2021

Additive and Interface Engineering of Lead-Tin Mixed Low-bandgap Perovskite Solar Cells for Higher Efficiency and Improved Stability

Nabin Ghimire
South Dakota State University, endreni2012@gmail.com

ADDITIVE AND INTERFACE ENGINEERING OF LEAD-TIN MIXED LOW-BANDGAP PEROVSKITE SOLAR CELLS FOR HIGHER EFFICIENCY AND IMPROVED STABILITY

BY

NABIN GHIMIRE

A dissertation submitted in partial fulfillment of the requirements for the

Doctor of Philosophy

Major in Electrical Engineering

South Dakota State University

2021

DISSERTATION ACCEPTANCE PAGE

Nabin Ghimire

This dissertation is approved as a creditable and independent investigation by a candidate for the Doctor of Philosophy degree and is acceptable for meeting the dissertation requirements for this degree. Acceptance of this does not imply that the conclusions reached by the candidate are necessarily the conclusions of the major department.

Yue Zhou
Advisor Date

Sid Suryanarayanan
Department Head Date

Nicole Lounsbery, PhD
Director, Graduate School Date

ACKNOWLEDGEMENTS

First, I would like to thank professor Dr. Quinn Qiao for providing me the opportunity to become a member of his diversified research group. He did not only just offer me a chance, but also believed in me and my potentials. He managed to afford me training in his lab before being formally accepted from graduate school. As a research advisor, Dr. Qiao never said "No" to me whenever I proposed new ideas and concepts. His leadership and encouragement have been significant throughout my research work and in improving the quality of this dissertation. I shall not forget whatever he has done to me.

My sincere gratitude goes to Dr. Yue Zhou, my academic advisor, who proficiently guided and supported me throughout these years. His calm and composed personality are the one which I'm always striving to learn. I will not forget his help and motivation.

My appreciations extend to Dr. Parashu Kharel and Dr. Hemachand Tummala for their essential role and support as committee members. I am also thankful to the Department of Electrical Engineering at South Dakota State University for encompassing all the administrative supports.

I feel very lucky to be a part of such a vibrant and friendly group. I would like to thank my colleagues for their generous supports during my experiments at the lab and their companionship and support outside the lab. I will miss all the moments we spent together.

I express my sincere gratitude towards my mother. Without her sacrifices, support, and love, I would not have achieved anything in my life. I thank my dear brother "Surya," who always encouraged and motivated me to seek better in life and strive for the best. I'm what I'm today because of his constant guidance, care, and love. I also like to thank my

dear sister Kopila and my sister-in-law, Gita, for their motherly love, compassion, and continuous support throughout these years. I bow down my head to my father, who always taught me great lessons in my life.

I express my sincere gratitude to my father and mother-in-law for their love, encouragement, and best wishes.

I would like to thank my dear wife “Shiksha,” who always stood by me in every moment of my crisis and joys. She always motivated and inspired me to become a better version of myself. She is the reason why I started and continued my Ph.D. journey. Finally, I would like to express my love and compassion towards our daughter ‘SUFI.’ She is the best gift we have ever got. I dedicate this dissertation to her, to the future !!

CONTENTS

ABBEREVIATIONS

τ_{rec}	Charge recombination lifetime
τ_{tr}	Charge transport time
μL	Microliter
Ω	Ohm
AC	Alternating current
AFM	Atomic force microscopy
Ag	Silver
BCP	Bathocuproine
C	Celsius
CS-AFM	Current sensing atomic force microscopy
Cs	Cesium
C_{60}	Buckminsterfullerene
DMF	Dimethylformamide
DMSO	Dimethyl sulfoxide
EA	Ethyl acetate
eV	Electron-volt
EDS	Energy dispersive spectroscopy
EIS	Electrochemical impedance spectroscopy
EQE	External quantum efficiency
ETL	Electron transport layer
FA	Formamidinium

FESEM	Field emission scanning electron microscopy
FF	Fill factor
FWHM	Full width at half maximum
GB	Glove box
HTL	Hole transport layer
IPA	Isopropyl alcohol
ITO	Indium doped tin oxide
J_{SC}	Short-circuit current density
KV	Kilo voltage
LBG	Low bandgap
LED	Light emitting diode
MA	Methylammonium
mg	Milligram
MHz	Megahertz
mL	Milliliter
MS	Mott-Schottky
NIR	Near-to-infrared
nm	Nanometer
N_{trap}	Trap density
Pb	Lead
PbI_2	Lead iodide
PCE	Power conversion efficiency
PEAI	Phenethylammonium iodide

PEDOT:PSS	Poly(3,4-ethylenedioxythiophene) polystyrene sulfonate
PL	Photoluminescence
PSC	Perovskite solar cell
PTAA	Poly[bis(4-phenyl)(2,4,6-trimethylphenyl)amine
RMS	Root mean square
rpm	Rotation per minute
SCLC	Space charge limited current
SEM	Scanning electron microscopy
Sn	Tin
SnI_2	Tin iodide
TPC	Transient photocurrent
TPV	Transient photovoltage
UV	Ultraviolet
UV-Vis	Ultraviolet visible
v/v	Volume/volume
V_{OC}	Open-circuit voltage
W	Watt
XRD	X-ray diffraction
ε_o	Permittivity
ε_r	Dielectric constant

LIST OF FIGURES

LIST OF TABLES

ABSTRACT

ADDITIVE AND INTERFACE ENGINEERING OF LEAD-TIN MIXED LOW-BANDGAP PEROVSKITE SOLAR CELLS FOR HIGHER EFFICIENCY AND STABILITY

NABIN GHIMIRE

2021

Lead (Pb) -Tin (Sn) mixed perovskites suffer from large open-circuit voltage (V_{OC}) loss due to the rapid crystallization of perovskite film, creating Sn and Pb vacancies. Such vacancies act as defect sites expediting charge carrier recombination, thus hampering the charge carrier dynamics and optoelectronic properties of perovskite films. In the first project, we focused on the passivation of perovskite surface defects to increase the open-circuit voltage of the 1.25 eV low-bandgap perovskite solar cells by utilizing a trace amount of Phenethylammonium iodide (PEAI) in the perovskite precursor solution as a doping agent. The incorporation of PEAI in perovskite precursors improved the perovskite film quality and crystallinity. In addition, it lowered the electronic disorder, enhancing open-circuit voltage up to 0.85 V, and power conversion efficiency up to 17.33 % was obtained with improved dark and ambient stabilities.

In the second project, we improved the charge transport dynamics of the Pb-Sn perovskite using interface engineering strategy by inserting an ultra-thin layer poly [bis(4-phenyl)(2,4,6-trimethylphenyl)amine] (PTAA) over the commonly used HSL of poly(3,4 ethylenedioxythiophene)polystyrenesulfonicacid (PEDOT: PSS). Modification of HSL ensured the suppression of the interfacial defects, enlarged the perovskite grain sizes, improved the crystallinity of the perovskite layer, enhancing open-circuit voltage up to

0.85 V, and a fill factor approached to ~ 80 % thus, power conversion efficiency boosted up to 19.41 % with improved dark-shelf and operational stabilities. These simple yet powerful additives and interface engineering techniques seem promising strategies to mitigate V_{OC}-loss in Pb-Sn mixed low-bandgap perovskite solar cells and can be easily applied in other mid-bandgap wide-bandgap perovskites.

Keywords: Low-bandgap perovskite solar cell, defect passivation, PEAI salt, interface modification, low V_{OC} deficit, lower trap, non-radiative recombination, PTAA modification

CHAPTER 1: INTRODUCTION

1.1 Background

Due to the extreme impact of human behavior on the environment, there is an urgent need to sustain all our activities. Human beings have relied upon the use of energy sources since the beginning of human civilization. Fossil fuels and oils have been serving as significant sources of energy demands right from the start of the industrial revolution. This has led to an upsurge in global carbon dioxide (CO_2) emissions levels. There are many implications of the continued use of fossil fuels and natural gas as demands for energy usage increase. CO_2 emissions, depletion of the ozone layer, air pollution, deforestation, and global warming are a few of the consequences that the heavy use of the fossils fuels and natural oils are causing [1]. Immediate actions need to be taken to reduce the damage to the environment. As the demand for energy is increasing, the non-renewable energy sources such as fossil fuels and natural gases also draining quickly [2]. The two primary reasons that stress seeking alternatives to fossil fuels and natural gases are the everlasting energy demands and energy restriction contribute to climate change. Reports say there are 1.4 billion people who are lacking from access to energy, and the rural communities relying on the conventional use of biomass is projected to increase from 2.7 billion in 2016 to 2.8 billion in 2030 [3]. On the other hand, supplying all the energy requirements in a modern, comfortable lifestyle yet sustaining the virtual community's needs has never been this crucial before. Sun is the most reliable and renewable source of energy. Tapping this endless source of energy and converting it into reliable forms are very significant. Solar energy itself, if utilized 100%, can fulfill the energy demand of the entire world.

Photovoltaic (PV) technology is considered one of the most reliable means to harvest solar power by converting sunlight into electrical energy. The principle of "The photovoltaic effect" and was discovered by Edmond Becquerel in 1838 using an electrochemical cell [4]. The photovoltaic effect states that "*The electrons can be promoted to the higher energy state if the material is exposed to the illumination of the light*." The first demonstration of PV cells was performed by Charles Fritts in 1884 using a thin sheet of selenium covered with a thin film of gold. The power conversion efficiency (PCE) of such cell was <1 %[4]. Later as technology advanced, the most helpful demonstration of the PV effect was evident using solid-state-device, mainly photodiodes. When sunlight is incident upon the photodiode, the electrons present in the valance band absorb energy and, being excited, jump to the conduction band and become free. These excited electrons diffuse, and some reach the rectifying junction, where they are accelerated into the p-type semiconductor material by the built-in potential. This generates an electromotive force and an electrical current, and thus some of the light energy is converted into electric energy. [5, 6]. Depending upon the advancement of materials and fabrication processes, the PV solar cells can be broadly categories into three generations.

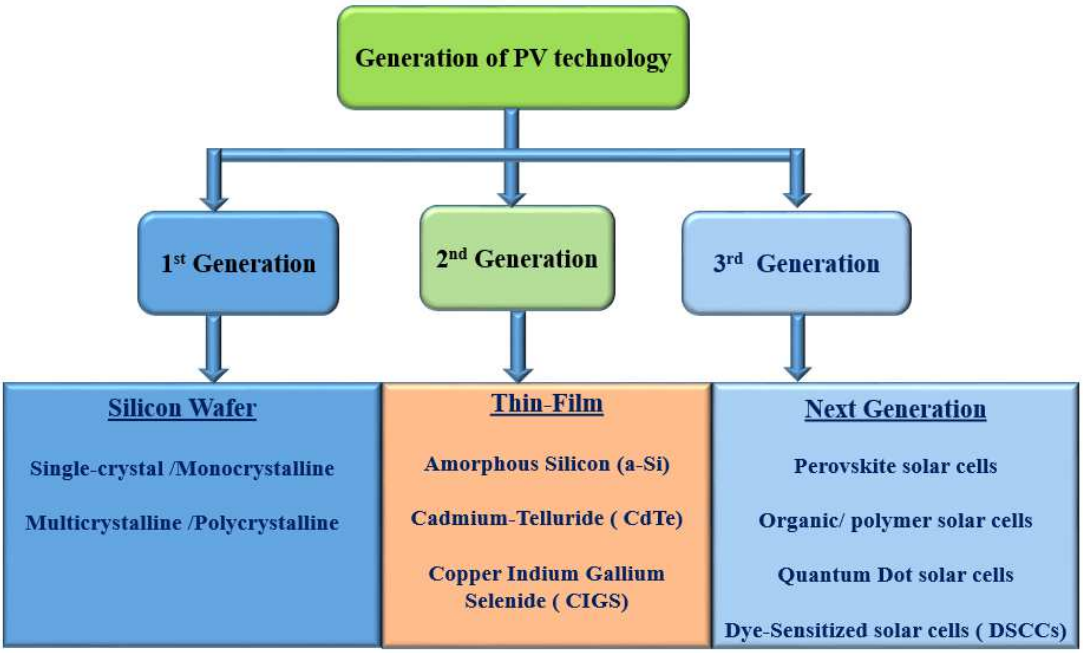

Figure 1.1. Three major PV technologies

As shown in figure 1.1 above, the first generation of solar cells is silicon solar cells fabricated from monocrystalline, polycrystalline silicon (Si) wafers. This type is the oldest and the most common due to high power efficiencies. However, the manufacturing process of first-generation solar cells require high temperature and are not flexible. Therefore, the second generation of PV technology was thin-film solar cells. This type of solar cell is fabricated using thin layers of semiconductor material, such as cadmium telluride or copper indium gallium selenide, or amorphous or microcrystalline Si. The typical thickness of such thin film is only a few micrometers; therefore, they have a lower production cost than the first generation.

Nonetheless, they have lower efficiencies in comparison to the first generation. The third generation is called next-generation solar cells. This new generation of solar cells is being made from various new materials besides silicon, including nanotubes, silicon wires, organic-inorganic metal halides (perovskites), and solar inks using conventional printing

press technologies, organic dyes, and conductive plastics. This type of solar cell is fabricated using thin layers (a few hundred nanometers) of semiconducting materials. These next-generation technologies may offer lower costs, greater ease of manufacture, or other benefits. Further research will see if these promises can be realized. Currently, most of the work on third-generation solar cells is still at the research level.

1.2 Basic theory of a solar cell

When photons hit the solar cell, electrons are promoted to conduction band from the valance band if incident photons have sufficient energy. Photons must transfer their energy to carriers in material. The carries should preserve significant parts of the absorbed energy, and then carriers should be collected at the PV device's terminals, resulting in electrons in the metallic wires flow through the electric circuit.

1.2.1 Electrical model of a solar cell

Under continuous illumination, the solar cell can be modeled as an electrical equivalent circuit with a single diode with series (Rs) and shunt (R_{sh}) resistances, as shown in figure 1.2. The current equations can be written as.

$$I = \frac{V - IR_S}{R_{sh}} + I_0\left(\exp\left[\frac{q(V - IR_S)}{nKT}\right] - 1\right) - I_L \qquad (1.1)$$

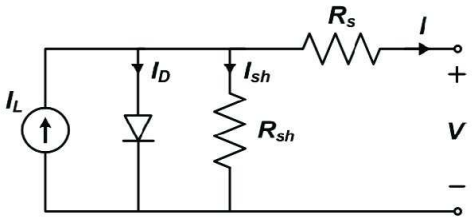

Figure 1.2. Equivalent solar cell electrical model.

Where, V is applied bias, and I is the total current through the circuit, I_0 is saturation

current. I_L is the current generated through light illumination, q is electron charge ($1.60217662 \times 10^{-19}$ coulombs), n is diode ideality factor, K is Boltzmann constant (1.38×10^{-23}J/ºK), and R_s & R_{sh} are parasitic series and shunt resistances, respectively.

1.3 Solar cell parameters:

Few key solar cell parameters determine the quality of the solar cell are explained briefly below.

1.3.1 Short circuit current (I_{sc})

Short circuit current is the current through the solar cell when the voltage across the solar cell is zero (I_{SC}). In practical application, I_{SC} is expressed in current density, i.e., current per square of the area.

$$J_{sc} = I_{sc} \times Area\ of\ the\ solar\ cell \tag{1.2}$$

1.3.2 Open circuit voltage (V_{OC})

This is defined as the voltage across the solar cell in an open circuit condition, i.e., when the current through the solar cell is zero. An equation for V_{OC} is found by setting the net current equal to zero in the solar cell equation to give,

$$V_{OC} = \frac{nKT}{q}\ ln\left(\frac{I_L}{I_0} + 1\right) \tag{1.3}$$

Where I_0 is reverse saturation current, IL is the current generated through light illumination, q is electron charge ($1.60217662 \times 10^{-19}$ coulombs), and n is the ideality factor of the diode, K is Boltzmann constant (1.38×10^{-23}J/ºK). Finally, T is the temperature at which the solar cell is operating.

1.3.3 Fill Factor (FF)

The maximum current and voltage generated by a solar cell are short circuit current (I_{SC}) and open-circuit voltage (V_{OC}). However, the net power of the solar cell is zero at these conditions.

The Fill Factor is defined as the ratio of the maximum solar cell power to the product of I_{SC} and V_{OC}. An ideal value of FF of any solar cell is unity. Closer the value of FF to unity, the higher the quality of a solar cell.

$$FF = (V_{MP} \times I_{MP})/(V_{oc} \times I_{sc}) \tag{1.4}$$

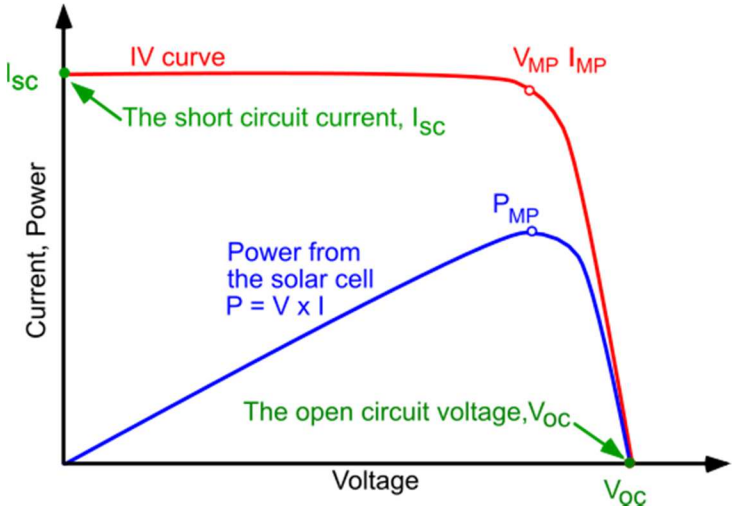

Figure 1.3. Typical I-V and power curves of a solar cell.

1.3.4 Power conversion efficiency (PCE)

V_{OC}, I_{SC}, and FF all are photovoltaic parameters of which defines the essential characteristics of a solar cell called power conversion efficiency (PCE) and is denoted by η and is expressed as:

$$\eta = \frac{V_{oc} \times I_{sc} \times FF}{P_{in}} 100 \quad (1.5)$$

Where p_{in} is the power input to the solar cell in the form of light energy.

1.3.5 External quantum efficiency (EQE)

It is the measure of the productiveness of a solar cell as a photon to electron converter. EQE is expressed as the ratio of the number of charge carriers collected by a solar cell to the number of photon incidents on the solar surface during illumination.

Mathematically,

$$EQE = \frac{Electrons\ out\ per\ second}{Photons\ in\ per\ second} \quad (1.6)$$

1.4 Introduction to perovskites

Perovskite is an oxide mineral composed of calcium titanate ($CaTiO_3$). The name perovskite is also applied to the class of compounds which have the same type of crystal structure as $CaTiO_3$, known as perovskite structure (figure1.4).The Perovskite was first discovered in the Ural Mountains of Russia by Gustav Rose in 1839 and is named after Russian mineralogist Lev Perovski.

Figure 1.4. Perovskite crystal found in nature.

Metal halide perovskites with generic structure ABX_3. Where A-site is an organic cation, such as Formamidinium (FA) and Methylammonium (MA), or inorganic chemicals such as Cesium (Cs) or a mixture of both organic and inorganic. B site is a metal cation such as Lead (Pb) and Tin (Sn), or a combination of both and X is the binder of A and B, and it could be Chlorine (Cl) or Iodine (I) or bromine (Br), or it could be a mixture of them. The perovskite crystal structure is illustrated in figure 1.5. The tolerance factor (t) and octahedral factor (μ) are the two main parameters determining crystallographic stability and probable structure. The tolerance factor is known as the ratio of the distance A-X to the distance B-X in the solid-sphere model and is expressed as.

$$t = (R_A + R_X)\ \sqrt{2}\ (R_B + R_X) \tag{1.7}$$

Here, R_A, R_B, $and\ R_X$ are the Goldsmith ionic radii of the equivalent ions. Where octahedral factor μ represents the ratio of R_B/R_X. Perovskite crystal structure generally has $0.81 < t < 1.11$ and $0.44 < \mu < 0.90$. To have a more stable perovskite crystal structure thus one more condition needs to be met, which is $R_A > R_B > R_X$.

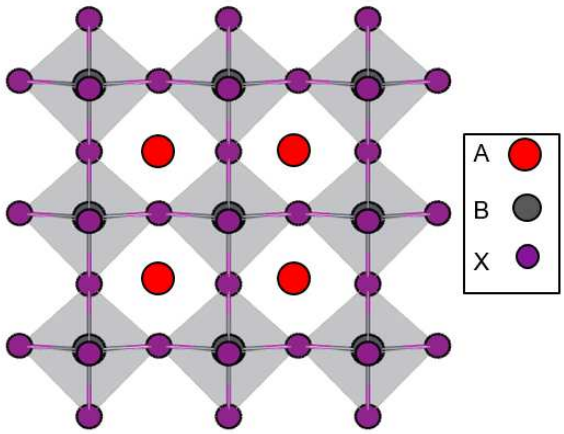

Figure 1.5. Organic-inorganic metal halide perovskite crystal structure

1.4.1 Properties of metal halide perovskites

Perovskite is a semiconductor with many exciting properties useful in many optoelectronic applications, such as LEDs, solar cells, and lasers [7-14]. Some of the essential properties are briefly discussed below.

1.4.1.1 Optoelectronic properties

Metal halide perovskites have several valuable optoelectronic properties that make perovskites suitable candidates for many optoelectronic applications. Unlike silicon, perovskites have a high absorption coefficient. Due to this, the thickness of the active perovskite layer is reduced (compared to silicon with several micrometers), and a few hundred nm of the active layer is sufficient to absorb an adequate amount of light for photon-electron conversion.

Another unique property is the long charge carrier lifetime. Perovskite possesses a long charge carrier lifetime in the range of microseconds. Sufficient time is essential for charge carriers to transverse across the thickness of the perovskite before electrons and holes can get recombined. Perovskites also have low binding energy (30-100 eV), due to which photo-generated charge carriers become free at room temperature, ensuring the facile charge collection at the electrodes.

1.4.1.2 Bandgap tunabilty

The most peculiar property of a perovskite semiconductor is that the bandgap can be easily tuned over a wide range just simply playing with the A, B, and X site components of ABX_3. Perovskite can be tuned to as low as 1.2 eV by simply alloying B site cation (Sn and Pb) in a proper ratio. If Cs is used as A-site cation and Br, or Cl or I is used as X, the

bandgap can be tuned as high as 3.06 eV [15]. Band-tunability opens avenues for multi-junction perovskite solar cells (PCSs), LEDs and lasers. Multi-junction PSCs are essential to overcome the efficiency limit of single-junction perovskite solar cells, which have already achieved the theoretical thermodynamic limit.

1.4.1.3 Ease of processing

Growing the perovskite is easy and cost-effective. Any perovskite composition can be either solution-processed at low temperature (< 150^{o} C) or solvent-free. Some notable solution-based methods are spin-coating, slot die coating, spray coating, and doctor blading. In solution-free methods, perovskite precursors are co-evaporated in a high vacuum system using a thermal evaporator, but the solution-based process is easy and cost-effective as all the perovskite precursor chemicals can be easily dissolved in the solvents. Solution processability also allows roll-to-roll processing of the perovskite devices. This would be useful in the large-scale production of perovskite devices.

1.4.1.4 Defect tolerance

Experimental studies have shown that metal halide perovskites are defect tolerant. Especially point defects and vacancies in perovskite semiconductors lie outside the electronic bandgap, making perovskite ideal for PV applications and various optoelectronic applications. The apparent source of vacancies in ABX_3 perovskite is loss of A-site cation (predominantly MA because of its volatile nature) and halide anion. B-site cations are not easily prone to the formation of vacancies because of their high formation energy and high redox potentials unless it is Sn. Thus, charge neutrality comes from self-regulating a loss of A-site cation by losing an X- site halide cation. Thus, the donor-acceptor charge

neutrality in the perovskite structure is responsible for overall system charge neutrality [16].

1.4.1.5 Lightweight and flexible

Among all existing thin film solar materials, perovskite has the highest power per weight, making it ideal for different lightweight optoelectronic applications. Because of lightweight and solution processing capabilities, perovskites can be used to make flexible devices.

1.5 Perovskite solar cell architectures

Perovskite solar cell device architecture can be broadly categories into three main architectures as shown in schematics below (figure 1.6).

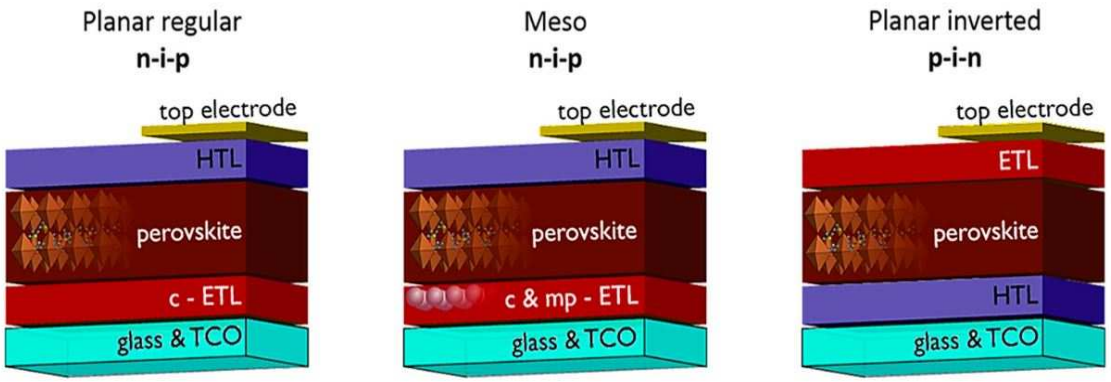

Figure 1.6. Schematics of the three PSCs architectures [9].

Irrespective of the architecture used, the light reaches the perovskite via TCO and hole selective layer or electron selective layer. The architecture is named based on the order in which the layers are deposited on the TCO. In planner regular n-i-p architecture, the bottom layer is an electron selective layer, followed by the perovskite layer, and the top layer is the hole selective layer. The compact electron selective layer is generally compact TiO_2 or SnO_2. The Mesoscopic n-i-p architecture (Meson-i-p) has compact and

mesoporous scaffolds that serve as a channel for electron transport. However, inverted p-i-n architecture has an inverted order of layers compared to n-i-p architecture; hence, the name is inverted p-i-n. A p-i-n structure has a hole selective layer up on TCO followed by perovskite and electron transport layers. In all structures, the topmost contact is a metal contact, and it can be silver (Ag) or gold (Au), or aluminum (Al).

1.6 Basic working principle of a typical perovskite solar cell

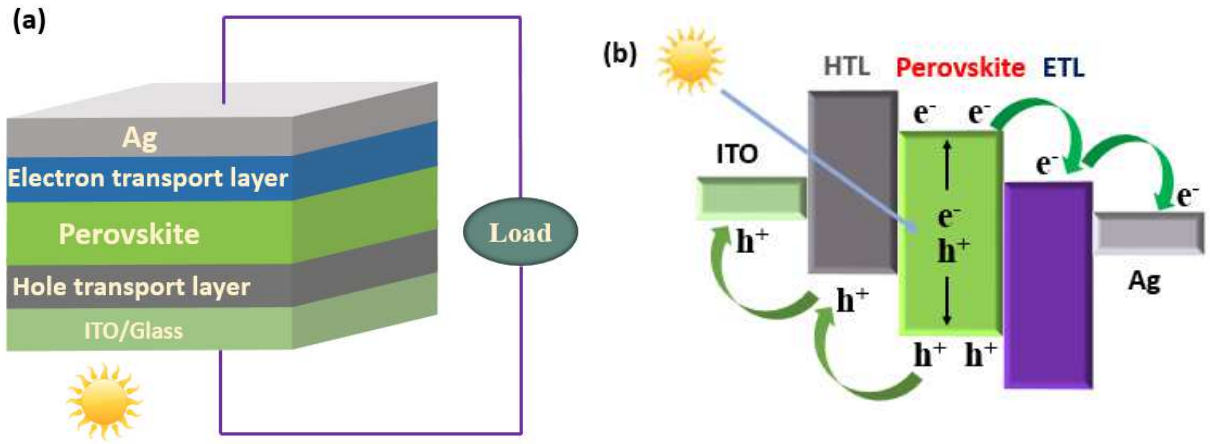

Figure 1.7. (a) Planner inverted p-i-n structure of PSC, (b) band diagram of typical p-i-n structure PSC

As shown in figure 1.7 (a-b), the perovskite layer is deposited between two opposite charge selective layers. Thus, the basic principle of perovskite solar cell operation involves the disassociation of electrons and holes as free charges upon the incident of sunlight to the perovskite via TCO and HTL, transportation of these holes and electrons by HTL and ETL in opposite directions, and finally, a collection of holes at ITO side and electrons at metal electrode side (Ag) thus completing the circuit to drive the external load. The HTL and ETL transport holes and electrons and block the opposite charge to prevent the

recombination before collecting these charge carriers at respective electrodes.

1.7 Recent progress in perovskite solar cell research

Organic-inorganic metal halide perovskite photovoltaic technology is still at the research level but has shown tremendous potential as next-generation solar cell technology. Since its first demonstration in 2009 (PCE <4%), PSCs have witnessed significant progress reaching the single junction-level highest certified power conversion efficiency (PCE) of 25.2% [17]. Excellent photo-physical properties and solution processability make perovskite solar the best candidate among the solar cell technologies [7-14, 18-20]. The NREL chart below shows the best research-level efficiency of PV technologies, including perovskites. The perovskites have emerged as a unique PV technology among other emerging technologies only in less than one decade, which other technology took almost many decades to achieve.

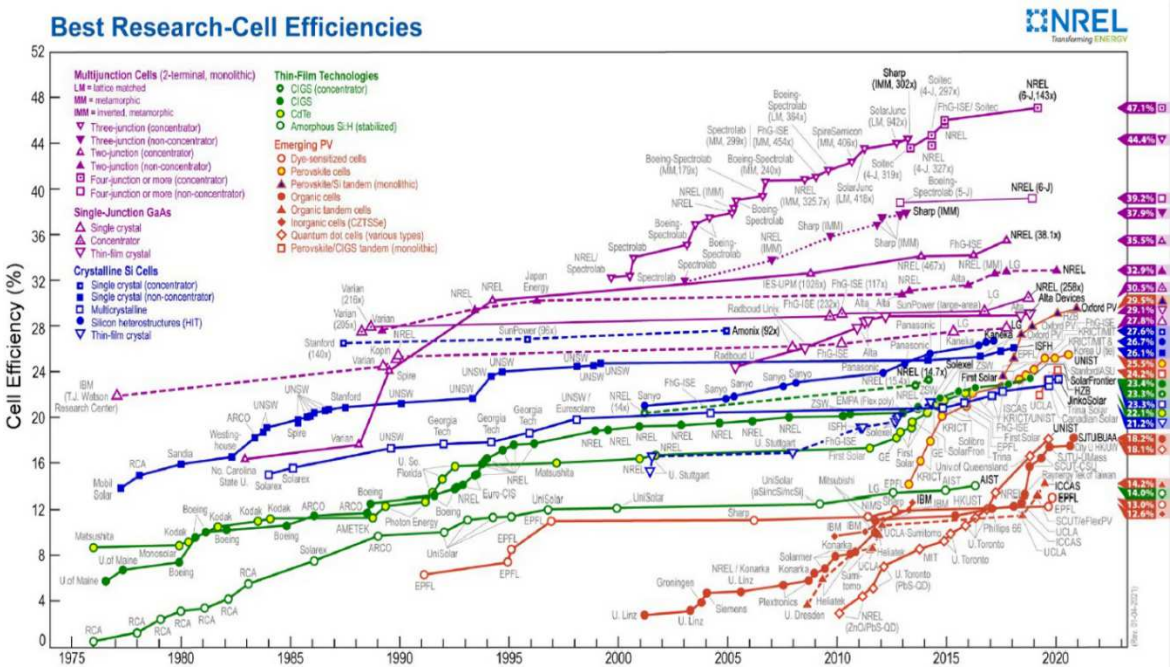

Figure 1.8. NREL best research cell efficiency for different PV technologies.

1.8 Lead-tin (Pb-Sn) mixed low-bandgap perovskite solar cells

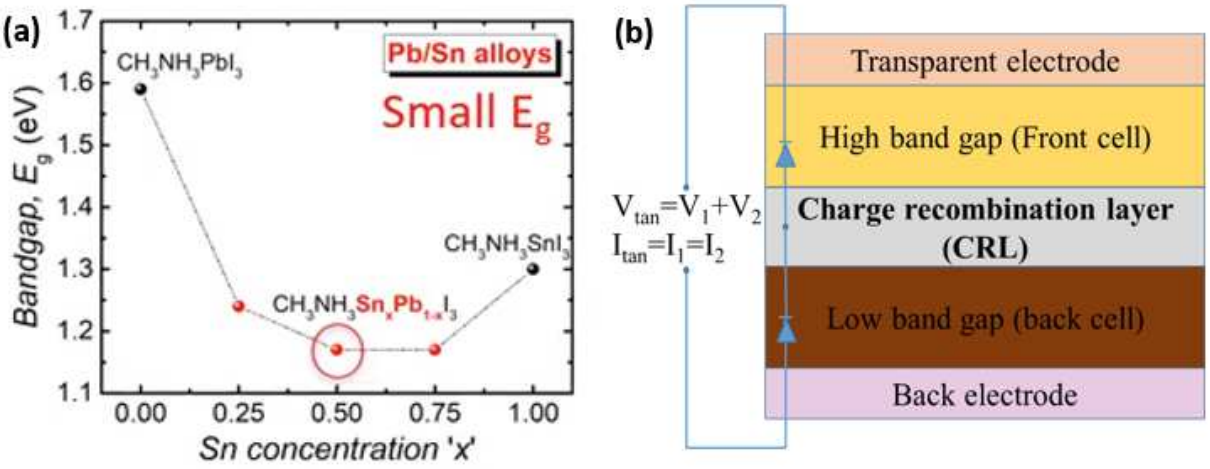

Figure 1.9. (a) Variation on bandgap of low-bandgap perovskite with Pb/Sn ratio [21], and (b) Schematics of typical tandem perovskite solar cells.

Perovskite solar cells (PSCs) have achieved substantial progress in the past few years, reaching the single junction-level highest certified power conversion efficiency (PCE) of 25.5 % [22, 23]. Excellent photo-physical properties and solution processability make perovskite solar the best candidate among solar cell technologies [7-14, 24]. The Shockley-Queasier limit governs the efficiency limitation of a single-junction perovskite solar cell [7, 25-27] thus, it is required to use multi-junction (tandem) perovskite solar cells to push forward the efficiency of the single- junction perovskite solar cells [18]. In this regard, Lead (Pb)-Tin (Sn) mixed perovskites have gained much attention in past few years because of their tunable bandgaps (1.2 -1.5 eV), extended range of photon absorption and lowered extent of toxicity [28-30]. As shown in figure 1.9 (a), the perovskite bandgap can be turned to as low as 1.2 eV by simply adjusting the Pb/Sn ratio. Advantage such as bandgap tunability makes Pb-Sn mixed PSCs ideal choice to be used as rear junction sub-

cell in all perovskites tandem solar cell applications where the excess light filtered through the wide bandgap (1.67 – 1.82 eV) absorber is absorbed by a low bandgap absorber (1.2 – 1.35 eV) as shown in figure 1.9 (b). Pb-Sn mixed LBG PCSs are getting considerable attention from the research community in the past few years, with some excellent efforts to improve chemical compositions, device structures, and fabrication protocol, including engineering of interfaces, bandgap, solvents, and additives.

1.9 Challenges in Pb-Sn mixed low-bandgap perovskite solar cells

The standard practice used to realize a low-bandgap perovskite absorber layer involves the use of Sn. Sn and Pb are mixed to serve as a "B" site cation in ABX_3. However, the use of Sn imposes some severe issues resulting in poor film quality, oxidation of Sn^{2+} to more stable Sn^{4+}, and creation of defects [31-33].

1.9.1 Poor film quality and crystallinity

Sn-Pb mixed perovskites suffer from inferior film quality as compared to pure lead-based perovskites. Several experiments have shown that the reaction of "A "site cation with Sn is much faster than with the Pb, which causes inhomogeneous crystallization of Pb-Sn throughout the film [26, 34]. Thus, resulting in poor film morphology, crystallinity, and compromised PV parameters such as open-circuit voltage (V_{OC}) and fill factor (FF). Optimization of fabrication protocols, recipes, composition, and processing conditions can help improve the film quality of Pb-Sn mixed perovskites.

1.9.2 Sn^{2+} oxidation/ self-doping

Pb-Sn mixed perovskites are prone to oxidation because of the use of SnI_2. This is the main reason for a large difference in PCE between Sn- and Pb- based PSCs. Sn^{+2} tends to oxidize to more stable Sn^{+4} even in a controlled environment. The standard redox

potential of Sn^{+2}/ Sn^{+4} is only +0.15 V which is low compared to Pb^{+2}/ Pb^{+4} with +1.67 V [35]. This is the primary reason why Pb based perovskites are vulnerable to ambient atmosphere whereas Sn based, or Pb-Sn mixed perovskites require precise control over fabrication atmosphere and processing parameters. Oxidation of Sn^{+2} to Sn^{+4} is very crucial, which creates Sn vacancies (p-type self-doping) on the perovskite film surface and at interfaces facilitating the non-radiative recombination loss in the perovskite.

There have been standard practices employed to compensate for such vacancies by adding a reducing agent to the perovskite precursors. The most used reducing agent is tin fluoride (SnF_2). Together with SnF_2, additives such as metallic tin powder, ascorbic acid have also been used to compensate for the Sn^{+2} vacancies [36, 37].

1.9.3 Defects

Due to its polycrystalline nature, perovskite film contains many grains and grain boundaries. Fewer grain boundaries and large grain size are always preferred as the possibility of charge leakage is essentially minimized. Pb-Sn mixed perovskites suffer from defects such as point defects and Sn vacancies during the film formation. Pb and Sn have different chemical properties, which causes lattice mismatch in Pb-Sn mixed perovskites. Sn^{+2} oxidation also causes contraction of grains and introduces residual strain compromising the efficient charge transportation.

Another issue is breaking of the chemical bond associated with Sn-I because the binding energy of Sn-I is lower than that of Pb-I. This can create the A-site vacancies in the perovskite crystals [38].

1.9.4 Large V_{OC} loss

Although Pb-Sn PSCs have higher J_{SC} because of extended range photon absorption but

V_{OC} of such PSC is compromised. This is mainly due to Sn^{+2} oxidation, poor crystallinity, and defects. V_{OC} loss can be expressed as,

$$V_{oc}loss = \frac{E_g}{e} - V_{OC} \quad (1.8)$$

Where E_g is optical bandgap of perovskite with unit of eV, e is elementary charge.

The main effort to improve the performance of Pb-Sn PSCs has been the strategies to improve the V_{OC} of the device. Lower the V_{OC} loss better the V_{OC} and other performance parameters of the PSCs.

1.10 Recent advancement in Pb-Sn mixed low-bandgap perovskite solar cells

Obtaining high-quality Pb–Sn perovskite films is a challenging task. In recent years, several efforts have been devoted to improving the perovskite and charge interfaces quality of Pb-Sn mixed low bandgap perovskite solar cells [22, 30, 36, 39-61].

Yang *et al.* reported that the combined compositional, process, and interfacial engineering approach uses 75% Pb and 25% of Sn as B site cation and varying the proportion of MA and FA as A-site cation. This improved the morphology of the perovskite films [44]. The best PCE of 14.2 % was obtained with the composition $MA_{0.5}FA_{0.5}Pb_{0.75}Sn_{0.25}I_3$ 1.33 eV with decent dark-shelf stability. In 2017, Zhao *et al*. used thickness optimization of perovskite layer in 1.25 eV $(FASnI_3)_{0.6}(MAPbI_3)_{0.4}$. By controlling the perovskite thickness and growth process, they could get a decent carrier lifetime of ~ 250 ns with ~700 nm thicker perovskite layer. The corresponding solar cell gave a certified PCE of ~17% [62]. They further improved the PCE up to ~20% by using strategies such as the incorporation of bromine, Guanidinium thiocyanate (GuSCN) in the perovskite precursor by suppressing the perovskite surface defects, suppression of leakage current, and prolonging the charge carrier lifetime [48, 54, 56, 63, 64].

Xu *et al.* used ultrathin bulk□heterojunction organic semiconductor (PBDB□T: ITIC) layer as an intermediary between the hole transporting layer and Sn–Pb□based perovskite layer to form a cascaded hole transport interface to minimize the carrier recombination at perovskite / HSL interface. As a result, PCE of 18.03 % with remarkably high Voc up to 0.86 V was obtained [65].

Chi *et al.* replaced PEDOT:PSS layer with NiO*x* as a hole transport layer, a power conversion efficiency of 17.25% was obtained with improved thermal stability [63]. Adharsh *et al.* used DF-C_{60} into the anti-solvent to form a graded heterojunction to passivate the defects of Pb-Sn mixed perovskite and obtained a remarkable V_{OC} up to 0.89 V [31]. Kapil *et al.* used a thin layer of spin-coated PCBM and a layer of thermally evaporated C60 to form a spike-like structure at the perovskite / ETL interface to minimize the conduction band offset as low as 0.15 eV. This ensured the facile charge flow from perovskite to Electron Selective layer (ESL), eventually improving PCE up to 17.6 % [66].

Jiang *et al.* employed delayed annealing (DA) treatment to obtain better interfacial contacts between the layers hence obtained less photo-voltage loss with improved PCE up to 18.6% [45]. Liu *et al*. employed the ZnO layer as a cathode buffer layer (CBL) between perovskite and PCBM interface to prevent the silver diffusion into the perovskite layer, which ensured reduced energy level mismatch between ESL and perovskite layer. They obtained PCE up to 18.1 % with an improved open-circuit voltage of 0.78 V [67]. *Lin et al*. reported a strategy of using a small amount of Tin (II) powder into the precursor to reduce Sn vacancies in Sn-Pb mixed low bandgap perovskite and achieved an efficiency of 21.1 % [58]. Wei *et al*. employed a strategy to passivate the perovskite defects by adding a trace amount of PEAI into the anti-solvent during the perovskite fabrication, eventually

getting PCE up to 18.95% in-film passivated solar cells [68].

Werner *et al.* employed a contact engineering approach to improve the perovskite / HSL interface by replacing PEDOT: PSS layer with the PTAA layer. A high-power conversion efficiency of ~ 20% was obtained with improved thermal stability when perovskite formation was performed with N_2 gas quenching. Nevertheless, the Voc obtained with this strategy was still lower than that of commonly used PEDOT:PSS as HSL [21, 26, 28, 44, 55-57, 62]. H. *et al.* used PEDOT:PSS and PTAA bilayer HSL to fabricate LBG PSCs but not sufficient detailing on the PEDOT:PSS/PTAA bilayer was reported [69] . The focus of the work was to enhance the charge carrier diffusion length by using a trace amount of cadmium in the perovskite absorber layer. They obtained PCE up to 20.3 % using this strategy. They obtained PCE up to 20.3 % using this strategy.

Tan *et al*. used formamidine sulfonic acid (FSA) as a surface-anchoring zwitterion antioxidant to reduce the Sn oxidation as well as to passivate both positively and negatively charge defects, eventually getting PCE of 21.7% and 18.8% for PSCs with areas of 0.049 and 1.05 cm^2, respectively [70]. Li *et al*. designed a two-step fabrication process to slow down the perovskite crystallization process. First, SnI_2/PbI_2 with Methylammonium thiocyanate (MASCN) and Pyrrolidinium thiocyanate (PySCN) was spin-coated on PEDOT:PSS substrates, and then FAI solution in isopropanol (IPA) was spin-coated. This two-step process could prolong the crystallization process with a significant reduction in Sn^{2+} oxidation, eventually boosting PCE ~20.4% with a high V_{OC} of 0.865V and good operational stability [71]. Based on the previous pioneer works in Pb-Sn LBG perovskite film and device fabrication, improving Pb-Sn perovskites film and device quality includes the serious consideration of the following three aspects.

a. Use of better antioxidant and passivation agents to prevent oxidation of Sn^{2+} to Sn^{4+}.
b. Control over crystallization process of perovskite film. This might include optimization of the fabrication process, recipes, and environment, etc.
c. Improvement of the stability of the devices. This includes proper encapsulation techniques, the right choice of substrates, and charge selective layers.

1.11 Motivation and objectives

1.11.1 Motivation

Fabrication of low-cost, efficient, and stable low-band perovskite solar cells for perovskite/perovskite tandem application to achieve efficiency beyond the Shockley-Queisser limit single-junction solar cells.

1.11.2 Objective

The objective behind this dissertation is to develop the strategy to fabricate the smooth–pinhole free, defect passivated Pb-Sn mixed low-bandgap perovskite absorber layers and use of that layer as a light absorber layer to achieve higher efficiency and stability. To achieve abovementioned objective, following tasks have been performed.

- Designed a new triple cation 1.25 eV low-bandgap structure.
- Employed additive engineering technique to passivate perovskite surface defects for higher efficiency and stability.
- Performed several film and device-level characterization methods to study the defects and the consequence of defect passivation after PEAI incorporation to the perovskite.

- Introduced a facile interface engineering scheme for suppressing interfacial defects, charge carrier trap sites and perovskite surface defects.

- Proposed the grain growth mechanism in not-wetting substrates such as PEDOT:PSS/PTAA.

- Studied the charge extraction and transport properties of PTAA modified HTL used perovskite thin films.

- Fabricated low-bandgap perovskite solar cells and performed different performance study.

1.12 Organization of the dissertation

Chapter 1 includes an introduction to perovskite, its structure, properties, and the working principle of PSCs. This chapter also includes the recent progress in PSCs research, challenges of low-bandgap perovskite solar cells, and the recent advancement on Pb-Sn mixed low-bandgap perovskite research motivation and objectives of this thesis work.

Chapter 2 discusses the experimental techniques used for perovskite film and device characterization throughout the study and related theories associated with each instrument and tool.

Chapter 3 describes the additive engineering approach employed to improve the Pb-Sn perovskite film and devices. This chapter also shows several characterization techniques to study the defects and the consequence of defect passivation.

Chapter 4 presents a facile interface engineering technique of our low-bandgap perovskite. Different films and device characterizations are also explained in detail.

Chapter 5 is the summary of the dissertation and the proposed future work.

CHAPTER 2 EXPERIMENTAL TECHNIQUES

2.1 Materials

Indium-doped tin oxide (ITO) substrates (Sheet resistance: 12 Ω/□, size: 1.5 cm x 1.5 cm, thickness: 1.2 mm) were purchased from Hartford Glass Co, USA. Lead (II) iodide (PbI_2, ultra-dry, 99.999%, LOT: T25F034) was bought from Alfa Aesar. Methylammonium iodide (MAI or CH_3NH_3I, 99.98 %) Formamidinium iodide (FAI or CH_5N_2I, 99.9%) was obtained from GreatCell Solar. Cesium iodide (CSI, 99.9%), Tin iodide (SnI_2, ultra-dry, 99.999%, LOT: X15F046), Tin fluoride (SnF_2, 99%), Phenethylammonium iodide (PEAI, 99.9%), Bathocuproine (BCP, 99.9%, sublimed grade LOT: 0000081433) and Lead thiocyanate $Pb(SCN)_2$ (99.5%) were purchased from Sigma Aldrich, USA. Buckminsterfullerene i.e., C_{60} (sublimed, 99.98%, Batch: BJ190612) was obtained from Nano C, USA. Poly (3, 4□ethylenedioxythiophene) □polystyrene sulfonic acid PEDOT: PSS (Clevios P VP AI 4083) was obtained from Heraeus Germany. Poly [bis (4-phenyl) (2, 4, 6-trimethylphenyl) amine (PTAA, CAS Number: 1333317-99-9) was obtained from Sigma Aldrich USA. All the solvents Dimethylformamide (DMF), Dimethyl sulfoxide (DMSO), and Ethyl acetate used in this study were anhydrous and were purchased from Sigma Aldrich USA. All solvents and materials were used as received.

2.2 Substrate cleaning

The patterned ITO glasses were cleaned using soap mixed deionized (DI) water, DI water, acetone, and isopropyl alcohol for 25 minutes each sequentially under ultra-sonication and blown dry with N_2. The substrates were then cured with UV-O_3 for 20 minutes. UV-O_3 treatment is necessary to remove any organic contaminants on the clean substrate and to improve the wettability of the substrates.

2.3 Perovskite precursor solution preparation

For the first project, the stocks solutions were prepared for both PbI_2 and CsI following the work by Saliba and coworkers [9]. 1 gram of PbI_2 was dissolved in 1.46 mL of mixed solvent (DMF: DMSO, 4:1 v/v) and heated at 180 ˚C for 10 minutes. Similarly, 78 mg (1.5 M) of CSI was dissolved in 200 µL of DMSO and heated at 150 ˚C for 5 minutes. Upon cooling, 464 µL and 45.25 µL of PbI_2 and CsI solution from respective precursor solutions were mixed with 233 mg of SnI_2, 30 mg of MAI, 172 mg of FAI. Together with these chemicals, 10 mol% of SnF_2 (15.6 mg) was mixed in DMF: DMSO (4:1 v/v) to retard the rapid oxidation of SnI_2. For perovskite with PEAI additive, a stock solution of 10 mg of PEAI in 100 µL DMF: DMSO (4:1 v/v) was prepared and added to the primary precursor as per need. For example, 10 µL of stock PEAI solution was added to a 666 µL of Perovskite precursor to get 1.5 mg PEAI per mL of perovskite precursor. The overall concentration of the perovskite precursor was 1.25 mole.

For the second project, perovskite solution was prepared according to the perovskite composition $FA_{0.8}MA_{0.15}Cs_{0.05}Pb_{0.5}Sn_{0.5}I_3$. Briefly, 0.8 M of FAI, 0.15 M of MAI, 0.5M of SnI_2, 0.5M of PbI_2, 0.035M of $Pb(SCN)_2$ and 0.01 M of SnF_2 were mixed to 944 µL of mixed solvent (DMF: DMSO, 4:1 v/v). For CSI, 78 mg (1.5 M) of CSI was dissolved in 200 µL of DMSO and heated at 150 ˚C for 5-7 minutes and upon cooling 56 µL was added to the mixed solution. The overall concentration of perovskite solution was 1.55 M. The solution was vigorously stirred at 60 ˚C for 2 hours before coating the perovskite layer.

2.4 Device Fabrication

Perovskite solar devices were fabricated using both solution-based spin-coating process and solution free thermal evaporation methods. The hole transport layer and perovskite

absorber layer were fabricated using solution-based spin-coating method whereas electron transport layer and metal contact (Ag) were deposited using thermal evaporator system. Figure 2.1 mimics the low-bandgap perovskite solar cell with all the layers fabricated in the lab.

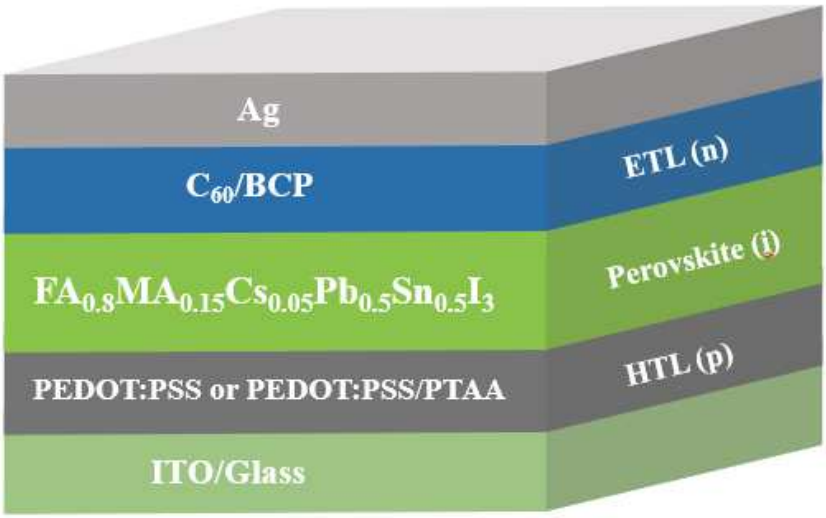

Figure 2.1. Schematics of low-bandgap PSC with all layers.

2.4.1 Hole transport layer (HTL) deposition

For the first project, a thin layer of PEDOT:PSS was then spin-coated on the UV-O_3 cured ITO substrate. The spinning protocol used for deposition was 5000 rpm speed/4500 rpm acceleration for 40 s, followed by annealing at 120 °C for 20 min. After cooling to the room temperature, the samples were immediately transferred to a nitrogen-filled GB for further processing.

For the second project, PEDOT: PSS layer was spin coated at 6000 rpm/s speed / 5500 rpm/s acceleration for 40 s and immediately annealed at 140 ˚C for 20 min. For

PEDOT:PSS /PTAA samples, a thin layer of PTAA (various concentrations of PTAA dissolved in 1 mL of CB) was spin coated over the PEDOT:PSS coated sample at the speed of 6000 rpm/s with the ramp of 2000 rpm /s. The samples were immediately annealed at 100 ˚C for 15 min inside a nitrogen-filled glove box.

2.4.2 Perovskite layer deposition

For the first project, 50 µL of the perovskite precursor with and without PEAI addition was dripped over the PEDOT:PSS-coated surface and then spun at 1000 rpm speed/350 rpm acceleration for 10 s and 5000 rpm speed/3500 rpm acceleration for 35 s. Then, samples were quickly washed with 200 µL of anhydrous ethyl acetate at 25^{th} sec of the second step to facilitate the crystallization process**.** The substrates were then transferred to a preheated hotplate and annealed at 60 °C for 3 min and 90 °C for 7 min.

For the second project, 45 µL of perovskite solution was dripped over the PEDOT: PSS or PEDOT:PSS /PTAA coated surface and then spun at the speed of 750 rpm/s with ramp of 500 rpm/s for 7 s and 5500 rpm/s speed with ramp rate of 3000 rpm/s for 35 seconds. 180 µL of Ethyl-acetate was quickly casted over the spinning sample at 25^{th} s at the second process. The substrates were then kept in a glass Petri dish for 5 min before annealing at preheated hotplate (90 ˚C for 10 minutes).

2.4.3 Electron transport layer (ETL) deposition

For the first project, C_{60} (28 nm), BCP (7 nm) were thermally evaporated inside a thermal evaporator under a vacuum of 3×10^{-6} Mbar.

For the second project, C_{60} (32 nm), BCP (8 nm) were thermally evaporated inside a thermal evaporator under a vacuum of 5×10^{-6} Mbar. The initial deposition rate for C_{60} was kept ~ 0.05A˚/sec for 8-10 nm then 0.2A˚/sec was used for rest of the thickness. BCP was

deposited at rate of 0.15 A˚/sec for entire thickness.

2.4.4 Metal contact (Ag) deposition

Finally, 100 nm of sliver (Ag) electrode was deposited using thermal evaporator system at rate of 0.2 A˚/sec for 8-10 nm and 1 A˚/sec for rest of the thickness.

2.5 Characterizations and measurement techniques

2.5.1 Film characterizations

2.5.1.1 Absorption profiles of perovskite films using UV-Vis spectroscopy

The absorbance profiles of perovskite films were recorded using the Agilent 8453 UV-Visible spectrometer in the range of 190 nm to 1100 nm using Chem station software. Since, Perovskite films were grown on top of either PEDOT:PSS or PEDOT:PSS/PTAA, background information of those films were collected first, and absorbance profiles of several perovskite films were recorded.

Figure 2.2 shows the basic building block of a typical single beam UV-Vis spectrometer, a tungsten lamp is used as light source for visible and near-infrared region. For a UV region a mercury lamp is used. Monochromator splits the light at different wavelength and passes them to the sample. The absorbance profile is created based on the light that is absorbed by the sample. The principle of UV-Visible spectroscopy is based on Beer-Lambert Law.

This law is expressed through this equation:

$$\text{Absorbance (A)} = -\log_{10}(I_0/I) \qquad (2.1)$$

I_0 stands for light intensity falling upon the sample, I is transmitted light.

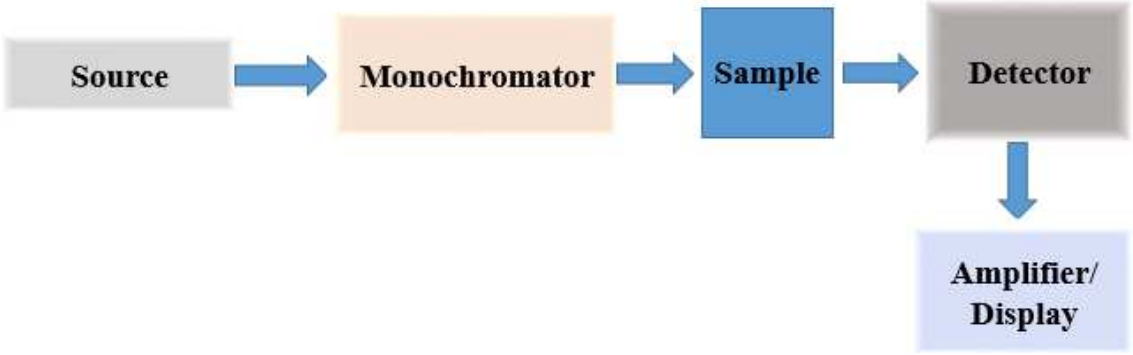

Figure 2.2. Block diagram of a typical single beam UV-Vis spectrometer

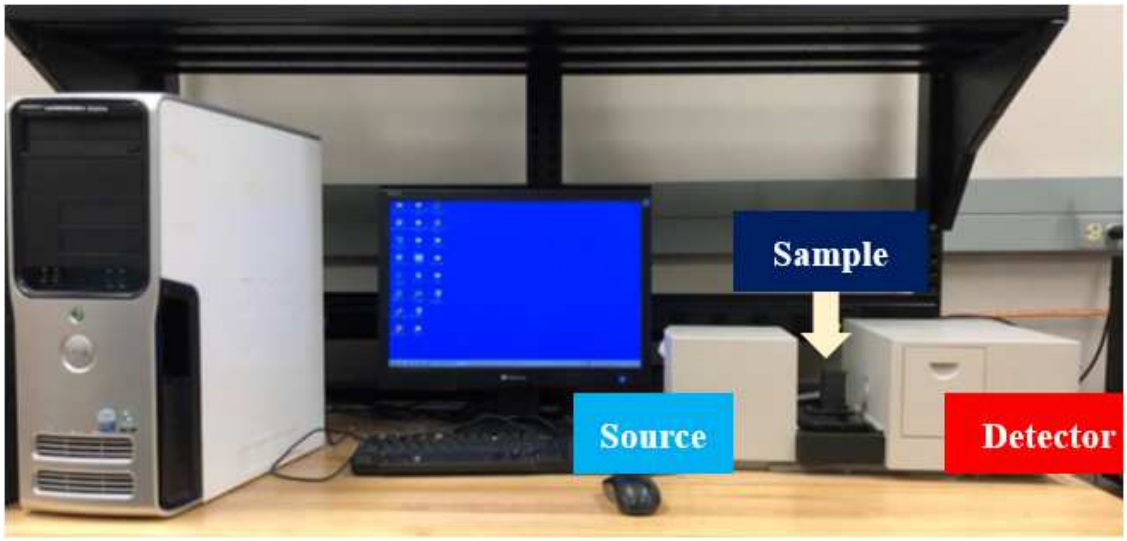

Figure 2.3. Agilent 8453 UV-Spectrometer

Figure 2.3 shows the lab setup of Agilent 8453 UV-Vis spectrometer for a measurement of thin film semiconductor.

2.5.1.2 Scanning electron microscopy (SEM)

In perovskite research, SEM plays a vital role to diagnosis the perovskite films. Perovskite is polycrystalline in nature meaning that a typical perovskite film surface

contains many grains and grain boundaries. SEM is very often used to study perovskite's the grain, grain boundaries, surface defects, surface morphology and pinholes. For our experiments, the morphology of the perovskite films was imaged using a field emission scanning electron microscope (Hitachi S-4700, figure 2.4) at an accelerating voltage of 3 kV. For imaging the samples, a thin conductive copper tape was used to connect the ITO glass and sample metal stub. 3 kV of acceleration voltage and 10 μA of current were applied at the ultrahigh magnification mode using secondary electron (SE) detector. The S-4700 FESEM also equipped with X-ray detection. The quantitative measurement of perovskite composition was also evaluated on the perovskite surface using SE detector and Oxford Aztec X- ray detector.

Figure 2.4. Hitachi S-4700 Field Emission SEM

2.5.1.3 Atomic force microscopy (AFM)

AFM is a type of scanning probe microscopy (SPM) that is very powerful for film

characterizations in perovskite research. Using AFM several film properties such as film roughness, local current distribution, grain size, and surface potential can be evaluated. Herein our research, AFM was used for topography imaging of perovskite films and local current distribution as well as topography imaging of PEDOT:PSS and PEDOT:PSS/PTAA HTLs. For surface topography imaging, Agilent 5500 AFM was used as shown in figure 2.5 (left) . As depicted in figure 2.5 (right) typical AFM system consists of nanometer-sized tip attached with the cantilever, a laser source, a photodetector. As laser falls on the tip, its movement changes according to the film surface height and roughness. This changes in the position of tip is detected by a photodetector and based on the surface information, topographic images are created [72, 73]. Depending upon the contact of the tip with the sample, different modes of operation such as tapping mode and contact mode are defined. For topographic imaging, tapping mode was used and for conductivity measurement current sensing AFM (CS-AFM) was used.

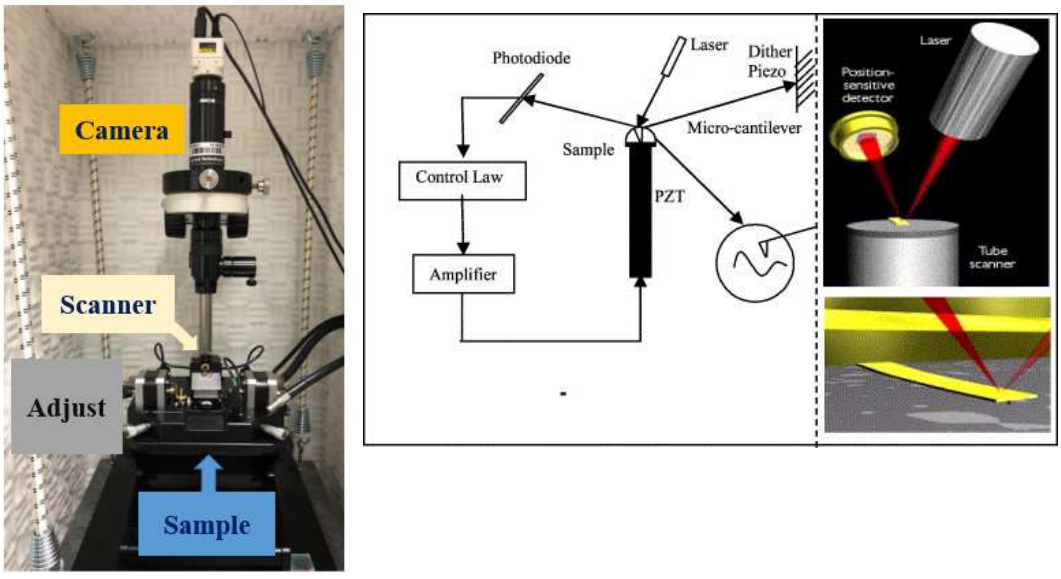

Figure 2.5. (left) Agilent 5500 scanning probe microscope, Schematic of basic AFM operation (middle), real micro-cantilever and components (right) [72].

2.5.1.4 X-ray diffractometer (XRD)

X-ray diffractometer is a widely used technique to examine crystal structures in composite materials. The crystallographic information of a crystalline structures can be studied using XRD. However, it can be also used to measure the degree of crystallinity in polymers. Traditionally XRD was used to examine bulk of the material but with the advancement in optical electronics, it is also possible to obtain the crystallographic information of thin films as well. When sample is tasted in an X-ray diffractometer, upon incident of X-ray, the crystal atom's electrons in the sample scatter the X-ray in all direction. An electron that scatters the incident X-ray is called scatterer. During the process, a combination of these scatterers produces an array of spherical wave, but these waves cancel each other out via destructive interference and only few waves in specific direction are added together as governed by Bragg's law (figure 2.6). Mathematically,

$$2d\sin\theta = n\lambda \tag{2.2}$$

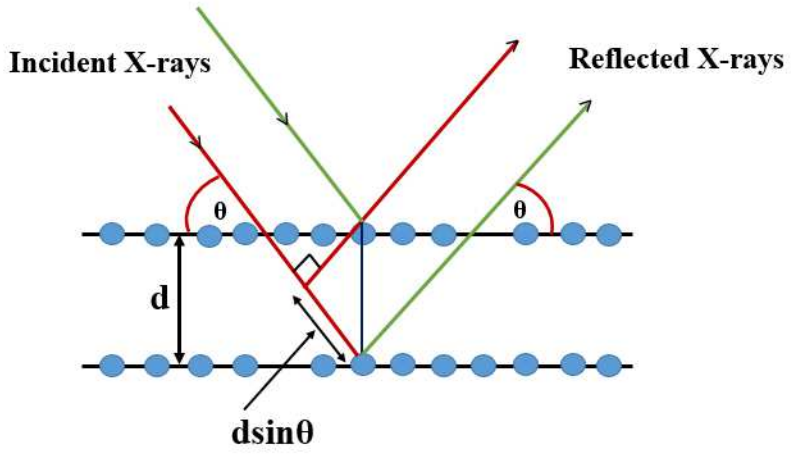

Figure 2.6. Illustration of Bragg's law.

For perovskite samples, XRD patterns were obtained using a Rigaku SmartLab system (2.2 kW, Cu Kα = 1.54 Å). For the measurement, tube voltage of 40 kV and tube current of 44 mA were used in PB/PSA medium resolution mode. A perovskite film coated on a quartz glass or clean ITO was placed on the flat surface of the sample holder and intensity was recorded at 2θ. Full width half maximum (FWHM) of peaks of interest were calculated using PDXL software. Figure 2.7 shows the Rigaku SmartLab system located in the lab.

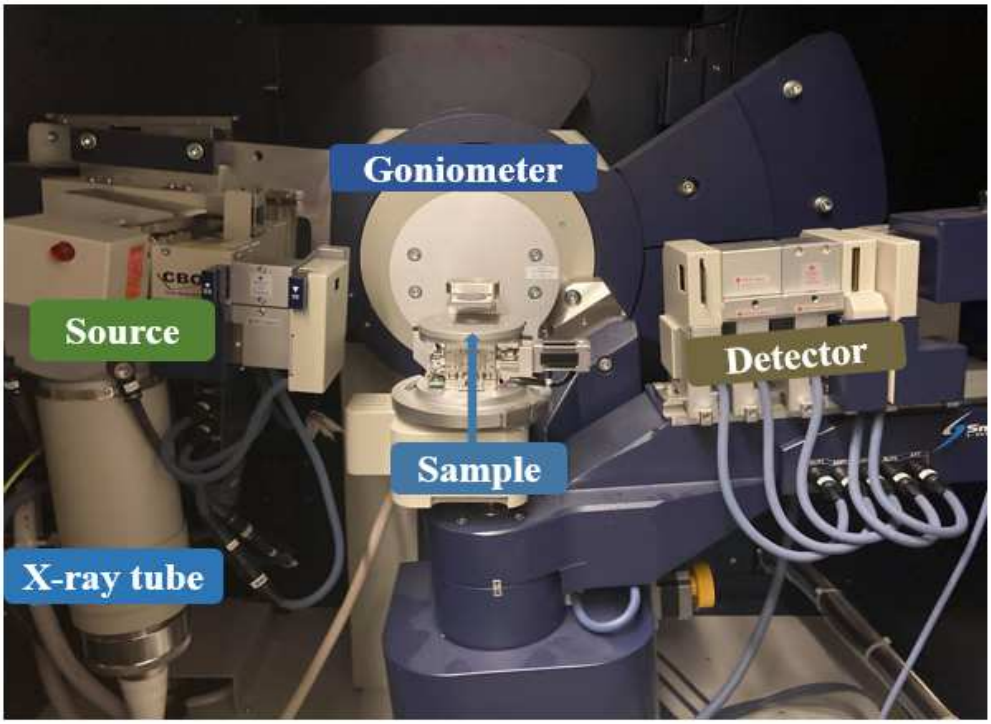

Figure 2.7. Rigaku SmartLab XRD system.

2.5.1.5 Photoluminescence (PL) spectroscopy

Photoluminescence (PL) spectroscopy is extensively used technique to study and examine the optical and electronics properties of semiconductors. It is particularly powerful characterization tool in perovskite research as much information about the lab-grown perovskite semiconductor can be collected simply by optically experimenting with

perovskite thin-films. We performed steady state PL measurements to gain the insight into the optical and electronic properties of our low-bandgap perovskites. The perovskite layer was deposited either on the glass substrate or on the top of HTL (in case of HTL modified project). The light was passed through the surface of the film upon investigation. The incident photons on the surface of the sample would create free charge carriers if the incidents photons has higher energy than the bandgap of the material through which light is passed. In case of modified perovskite, it is essential to get the information about the strength of photoemission because larger the amount of photoemission, lower the non-radiative recombination sites in the perovskites. In case of HTL modification (perovskite with charge selection layer), the strength of the photoemission should be less because generated charge carriers get attracted and collected at the charge selective layer. A typical arrangement of steady state experiment using Edinburg FLS 920 florescence spectrometer is shown below.

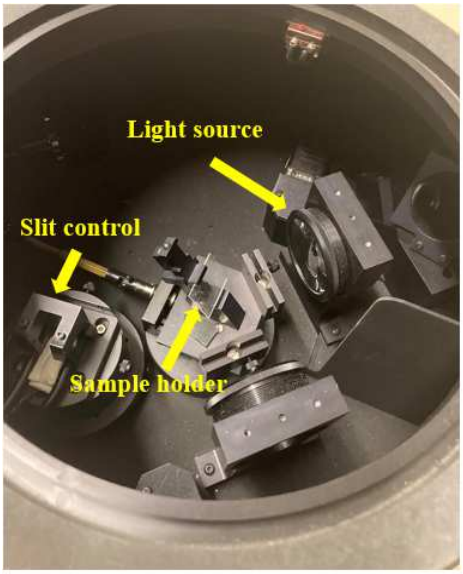

Figure 2.8. Edinburg FLS 920 florescence spectrometer arrangement for steady state PL measurement.

2.5.1.6 Surface profilometry

Profilometry is a technique to extract the topographical information from thin-film surfaces. There are two types of surface-profilometers based on the types of operation. First one is called optical profilometer which is a non-destructive way of collecting information from the thin film sample. The other one is called stylus profilometer that uses a diamond tip that physically touches the sample surface to extract different surface information as surface roughness, morphology, and step height hence it is a destructive way of collecting the information. In our case we used styles based profilometer. The thickness of the perovskite films and HTL were measured using Vecco Dektek 150 profilometer (figure 2.9).

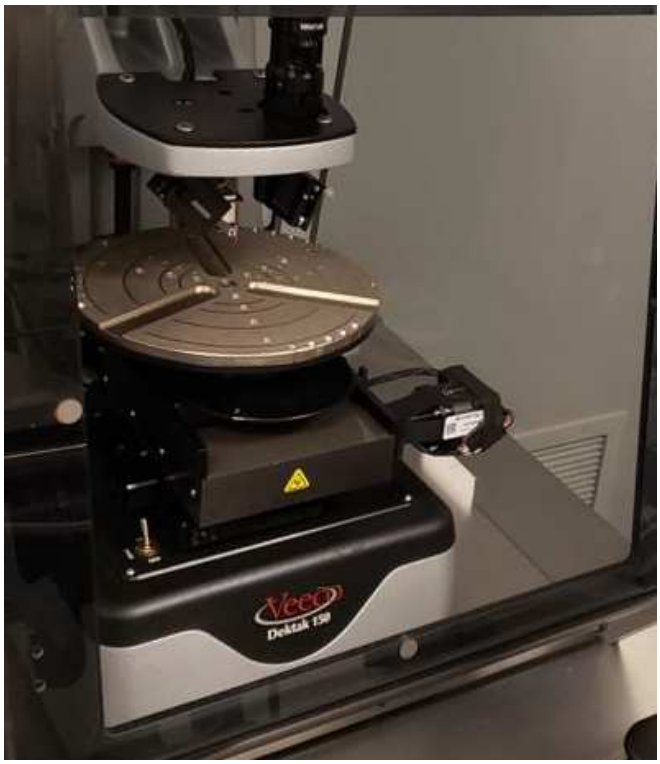

Figure 2.9. Vecco Dektek 150 surface profilometer.

2.5.1.7 Contact angle measurement

To check the wettability of the perovskite as well as charge selective layers, we performed the contact angle measurement using VCA 2000 video contact angle system. In a typical experiment, a thin film sample was placed on the flat surface and water was injected drop by drop, as the water drop reaches to the film surface it either stays on the surface as a drop or disperses throughout the sample depending upon the nature of the sample and its chemistry with the water. The contact angle of water and the surface is recorded using the video contact mode.

2.5.1.8 Electronic disorder measurement

Electronic disorder in semiconductors can be quantitatively analyzed by using the absorption information of the semiconductor of interest. Precise way of calculating the electronic disorder involves the use of photo thermal deflection spectroscopy (PDS). Electronic disorder can also be investigated by using the absorbance information from UV-Vis data or spectral information from EQE data. However, these processes are not as accurate as PDS and may not give an absolute value, but they are very useful while doing the comparisons among different semiconductors or same semiconductor with different treatments. In our case, we used the absorbance data to calculate the electronic disorder (also known an Urbach energy) of low-band perovskite with or without the PEAI treatments. An Urbach energy is estimated below the bandgap of the semiconductor using the relation

$$\alpha = \alpha_0 \, \mathrm{Exp} \left(\frac{E}{E_u}\right) \tag{2.3}$$

Where, α is an absorption coefficient, E (=hγ) is the photon energy, and E_u is the Urbach

energy.

High value of Urbach energy indicates the presence of defect states between valance and conduction band of a semiconductor. Thus, lower value of Urbach energy is preferred.

2.5.2 Device characterizations

2.5.2.1 Current-voltage (I-V) measurement

An archetypal setup for measuring the current-voltage response of PSCs was shown in figure 2.10. an AM 1.5 solar simulator (Model no. 91192, Oriel, USA) in conjunction with a semiconductor parameter analyzer (Agilent 4155C, figure 2.10) was used to measure the current density-voltage (J-V) characteristics at a light intensity of 100 $mWcm^{-2}$ determined by NREL calibrated silicon reference cell (S1133-14). The devices were scanned in both forward (0 to 1 V) and reverse (1 to 0) at a scan speed of 25 mVs^{-1}. A metal mask of aperture area 0.08 cm^2 was used to define the active area of the devices. No preconditions were applied for the measurements of all PSCs.

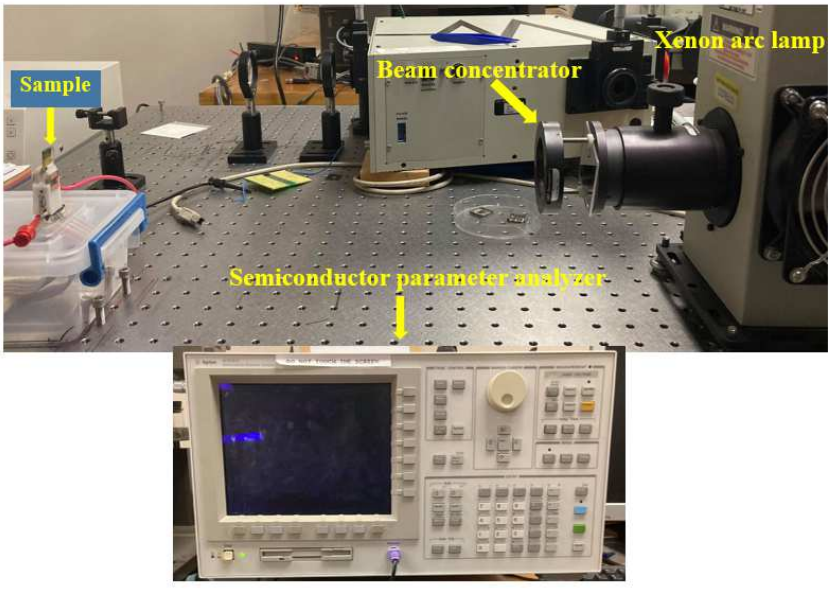

Figure 2.10. Current-voltage measurement setup using solar simulator and semiconductor parameter analyzer.

2.5.2.2 External quantum efficiency (EQE) measurement

An external quantum efficiency (EQE) measurement was performed using Newport IPCE system that consisted of a Xenon arc lamp (Newport, model 67005), monochromator (Oriel, model 74125) and semiconductor parameter analyzers (Agilent, model 4155C).Figure 2.11 shows a lab setup for EQE measurement of PSCs. An NREL calibrated photodiode (Hamamatsu mono-Si cell photodetector S111-14) was used to record the reference EQE spectrum. Two focusing lenses were used to focus the light passed through the monochromator. Samples were illuminated in a dark condition to avoid the possible light interference and EQE spectra were recorded in the range of 300-1100 nm with a step size of 5 nm. Amplifier was used to provide output to the semiconductor parameter analyzer. Finally, the EQE of PSCs were calculated using the relation below.

$$EQE_{sample} = (V_{sample} \times EQE_{reference}) / V_{reference} \quad (2.4)$$

Where EQE_{sample} is the EQE data of the PSCs. V_{sample} and $V_{reference}$ are voltages recorded for perovskite sample and reference photodiode respectively. $EQE_{reference}$ is the standard EQE for the reference photodiode.

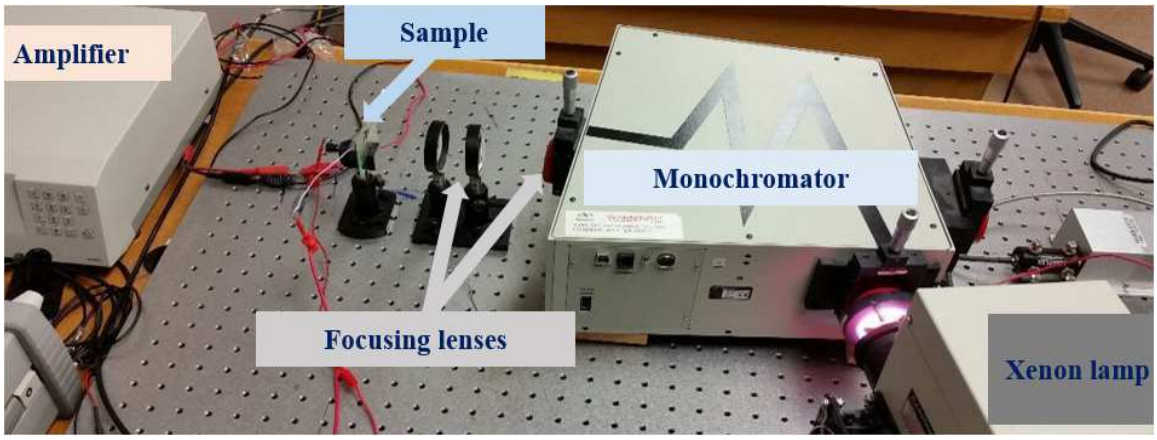

Figure 2.11. Lab set up of the EQE measurement.

2.5.2.3 Transient photovoltage and photocurrent measurements

Transient measurements were conducted using nitrogen laser (OBB's Model OL-4300) pulse at 377 nm to pump a dye laser (model 1011) for generating a short pulse. This pulsed laser was used as an excitation source with <1 ns pulse duration and ~4 Hz frequency. The responses were recorded with the help of oscilloscope.

2.5.2.3.1 Transient photovoltage (TPV) measurements

The TPV measurement was performed to study the photoconductivity of the PSCs. In a typical setup, devices were illuminated with white light (1.5 AM) and kept at open circuit voltage by applying very high impedance of 1M Ω across the solar cell terminals (figure 2.12). The charge recombination lifetime or charge carrier lifetime (τ_{rec}) was calculated from fitting of the exponential decay curve with mono-exponential function [30].

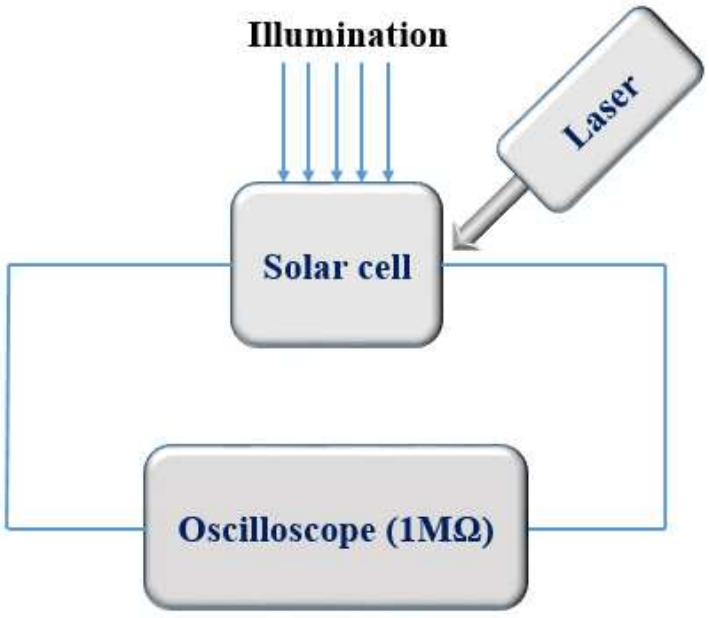

Figure 2.12. Schematics of TPV measurement.

2.5.2.3.2 Transient photocurrent (TPC) measurements

The TPC measurement was performed to study the photoconductivity of the PSCs. In a typical setup, devices were kept and at short circuit condition by applying very low impedance of 50 Ω across the solar cell terminals (figure 2.13). The charge transport time (τ_{tr}) was calculated from fitting of the exponential decay curve with mono-exponential function [30].

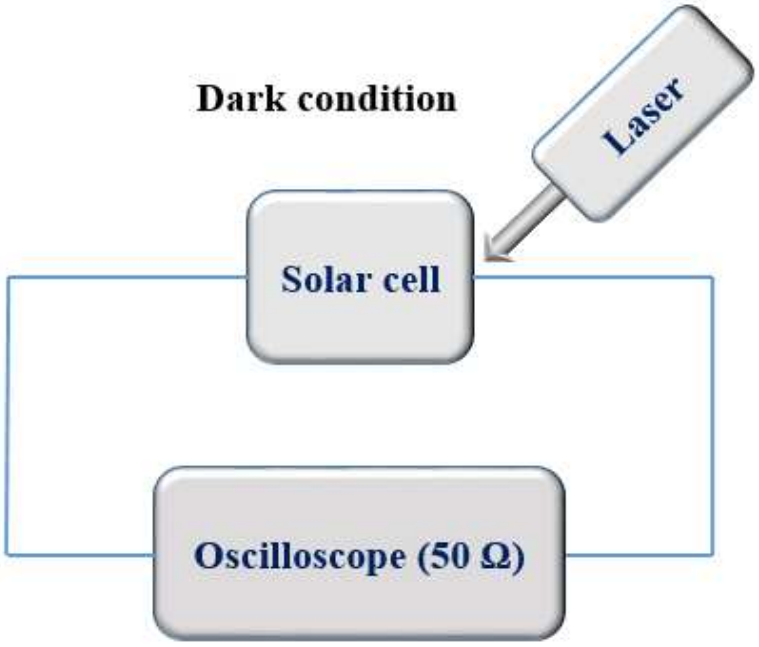

Figure 2.13. Schematics of TPC measurement.

2.5.2.4 Electrochemical Impedance Spectroscopy (EIS) and Mott-Schottky measurements

Electrochemical Impedance Spectroscopy (EIS) is a powerful tool to measure the electrochemical reaction to an AC potential over a wide range of frequencies [19, 74, 75]. EIS is a very established technique to estimate the charge extraction and charge

recombination processes in PSCs[76]. For an EIS measurement, Ametek VERSASTAT3□ 200 Potentiostat was used in the frequency range 1 Hz–1 MHz with amplitude of 20 mV in dark condition at MPP. The values of charge charrier recombination resistances were calculated by fitting plots using single RC circuit. Capacitance-Voltage measurement was performed using Ametek VERSASTAT3□200 in Mott-Schottky mode with fixed frequency of 20 KHz and perturbation AC voltage of 20 mV in dark condition. The built-in potential at the charge interfaces were calculates using the mott-Schottky plot.

2.5.2.5 Charge mobility measurement using photo CELIV

Photo CELIV measurement is used to investigate the charge extraction quality of charge selective layers of a photovoltaic device. In a mobility measurement experiment using photo CELIV, a linearly increasing voltage (triangular pulse) is applied to extract thermally generated charge carriers and mobility is calculated from the peak of the extraction time of corresponding transient curve [77-81]. The charge carrier mobility (μ) is expressed as [82];

$$\mu = \frac{2d^2}{3At_{max}^2} \tag{2.5}$$

Where t_{max} is the maximum attainable voltage. A is the slope the ramp voltage applied; d is the thickness of the active layer.

2.5.2.6 Space charge limited current (SCLC) method for trap density calculation

Trap densities in the device can be calculated using SCLC measurement. In the dark J-V curve of a single carrier device (Hole only or electron only device), there are three distinct regions and can be defined by $J \propto V^n$ relation, with n=1 being ohmic region, n=2 is the

SCLC region or the child region. The third region (n>3) is called the trap-filled region (TFL), which lies in between the ohmic and child region, where current increases quickly and non-linearly with a small increase in bias voltage specifying that traps are continuously filled up with the charges[83]. The kink point is called trap-filled-limit-voltage (V_{TFL}) and is used to calculate the trap density (N_{trap}) using the equation below [84].

$$N_{trap} = \frac{2\varepsilon_0 \varepsilon_r V_{TFL}}{eL^2} \tag{2.6}$$

Where ε_0 and ε_r are free space vacuum permittivity and relative dielectric constant of the active layer, respectively; L is the thickness of perovskite film, and e is the elementary charge.

2.5.2.7 Light Intensity dependence on V_{OC} and J_{SC} and FF

The charge recombination and charge extraction mechanisms can be studied by simply varying the incident light intensities on the solar cell and recording voltage and current responses at different intensities. The relationship between V_{OC} and light intensity (I) is given by,

$$V_{OC} = \frac{nKT}{q} \ln\left(\frac{I}{I_0}\right) \tag{2.7}$$

Where q is the elementary charge, n is the ideality factor, K is the Boltzmann constant, and T is the temperature. The value of the slope of V_{OC} versus ln (I) profile is used to estimate the diode ideality factor and indicate the recombination mechanics dominating the device during the operation. The value of slope KT/q away from the unity indicates the dominance of trap-assisted monomolecular Shockley–Read–Hall (SRH) recombination, and the

slope's value closer to the unity indicates the dominance of bimolecular recombination phenomena in the device.

In light dependence current test, the charge extraction ability of a charge selective layer is estimated quantitatively using a relation.

$$J_{sc} \propto I^{\alpha} \tag{2.8}$$

Where J_{SC} is the current density at light intensity I. α is estimated from the slope of the curve. Value of α near to unity indicates the superior charge extraction ability of the charge selective layer and also indicates the lower extent of recombination and potential barrier [85, 86]. Significantly lower value of α indicates the presence of defects states in the device.

The light dependence FF test is performed to evaluate the recombination kinetics in the device during the operation. The FF value is expected to be almost constant throughout the illumination intensities if the recombination mechanism in a solar cell is dominated by bimolecular recombination. In the presence of traps and recombination centers, FF will not be constant because more photo-generated charges will be needed to fill-up the traps [87-90].

CHAPTER 3 MITIGATING OPEN CIRCUIT VOLTAGE LOSS IN LEAD-TIN MIXED LOW-BANDGAP PEROVSKITE SOLAR CELLS VIA ADDITIVE ENGINEERING

3.1 Introduction

Fabrication of high quality Pb-Sn mixed low-bandgap perovskites is challenging because of the inferior film quality and chemical instability related to rapid oxidation of Sn^{+2} into more stable Sn^{+4}. Because of the oxidation, vacancies are created on the perovskite film's surface causing inferior optoelectronic quality, low crystallinity, and inefficient charge transfer properties. Rapid crystallization is also a major issue in LBG perovskites that makes perovskite film surface susceptible to defects and traps causing high non-radiative recombination loss which seriously compromises performance of the solar cells. Specially, high open circuit voltage (V_{OC}) loss is a major issue in LBG perovskite solar cells. In this project, we employed an additive engineering technique to improve the perovskite film quality and compensate the perovskite surface defects. The aromatic compound Phenethylammonium Iodide (PEAI) was selectively chosen as doping agent to compensate the Sn oxidation. A trace amount of PEAI directly added to the perovskite precursor solution not only improved the perovskite film quality and crystallinity but also lowered the electronic disorder thereby boosting the V_{OC} as high as 0.85 V (V_{OC} loss of 0.4 V) and power conversion efficiency up to 17.33%.

The value of V_{OC} loss achieved with this approach is amongst the smallest obtained for similar bandgap LBG PSCs. With the PEAI treatment, the stability of the unencapsulated PSCs also improved. This work presents a simple doping strategy to mitigate the V_{OC} loss of Pb-Sn mixed low-bandgap perovskite solar cell.

KEYWORDS: low-bandgap perovskite, PEAI salt, defect passivation, Pb−Sn hybrid perovskite, additive engineering, Voc deficit

3.2 Result and Discussion

The chemical composition of $FA_{0.8}MA_{0.15}Cs_{0.05}Pb_{0.5}Sn_{0.5}I_3$ was chosen as the baseline composition for the films and devices fabrication. The composition was fabricated using the anti-solvent aided single step spin-coating method and was tested several times to get the consistent film quality and optical bandgap. For doping, different PEAI concentration were added to the perovskite solution. The perovskite films and devices fabricated using as 0.5 mg PEAI per mL, 1.5 mg PEAI per mL 2.5 mg PEAI per mL of perovskite solution were termed as 0.5 PEAI, 1.5 PEAI, and 2.5 PEAI respectively. The pristine films or devices made without PEAI addition in the perovskite solution was named as “Control”.

3.2.1 Solar cell fabrication process

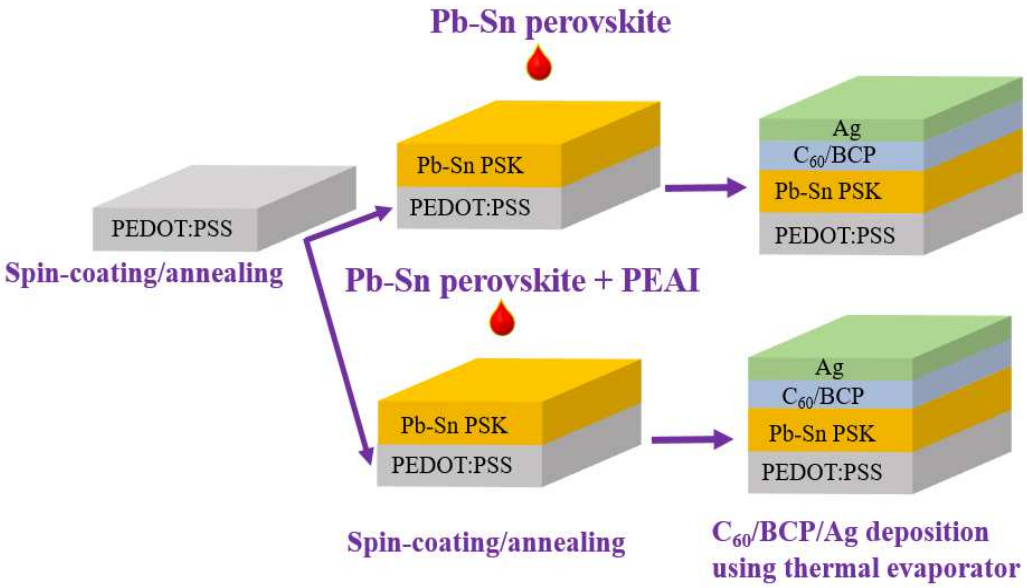

Figure 3.1. Low-bandgap perovskite solar cell fabrication process.

Figure 3.1 shows the complete solar cell fabrication process, first a thin layer of hole transport layer (PEDOT:PSS) was deposited at ambient condition using the spin-

coater. The spinning parameters used were 5000 rpm speed and 4500 rpm acceleration for 40 s and annealed at 120° C for 20 min. Immediately after cooling down to the room temperature, samples were processed inside the nitrogen-filled glove box. For a perovskite deposition, 50 µL of perovskite solution was spin coated on the PEDOT: PSS coated surface. The protocol used for spinning was 1000 rpm speed /350 rpm acceleration for 10 s and 5000 rpm speed /3500 rpm acceleration for 35 seconds. The samples were quickly wash away with 200 µL of anhydrous ethyl-acetate at 25th sec of second step to aid the crystallization process. The substrates were then annealed at 60 ˚C for 3 min and 90 ˚C for 7 minutes. For ETL deposition, C_{60} (28 nm), BCP (7 nm) were thermally deposited inside a thermal evaporation chamber before depositing 100 nm silver as contact electrodes.

3.2.2 Optical, Electrical, and Physical properties of perovskite films

Figure 3.2 (a) shows absorbance spectrum of control and various amount PEAI doped perovskite films.1.5 PEAI showed better absorbance than other concentrations of PEAI, however the optical bandgap remained constant at 1.25 eV as depicted in figure 3.2 (b).

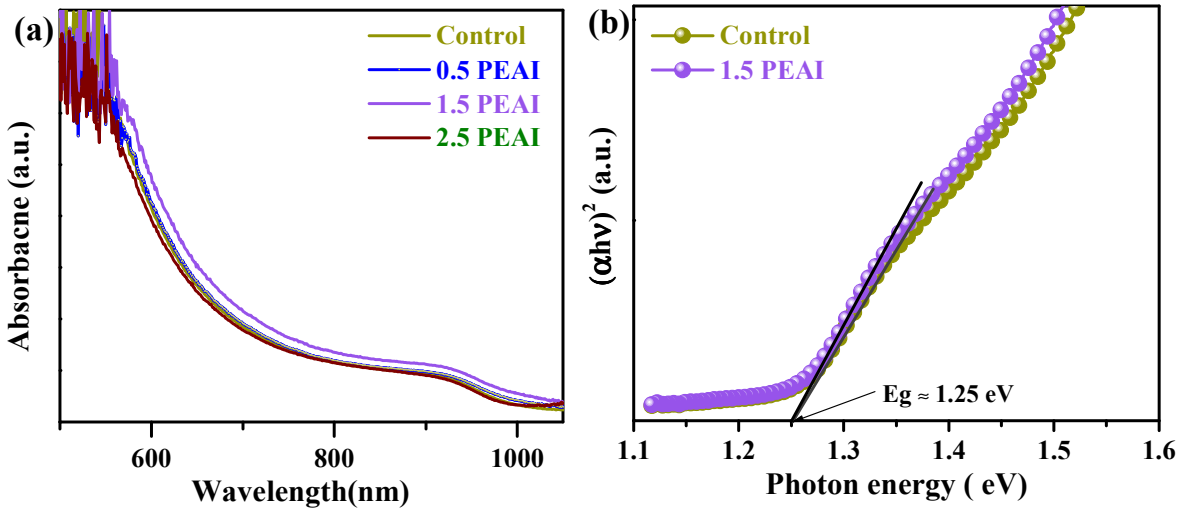

Figure 3.2. (a) UV-Vis spectra of control and various amount PEAI doped perovskite films, and (b) Tau-c-plot of control and 1.5 PEAI doped perovskite films.

Figure 3.3 illustrates the top view scanning SEM images of perovskite film with and without PEAI addition. All perovskite films showed compact film morphology without any pinholes but 1.5 PEAI showed enhancement in compactness and smoothness of the film. The white particles can be seen in control film that might be PbI_2/SnI_2 complex. The films with PEAI have so such particles on the surface. Hence it can be said that PEAI not only improved the compactness and smoothness of films but also removed unwanted PbI_2/SnI_2 complex from the film surface. SEM result is also in a good agreement with the topographical images acquired from the AFM measurement where reduction in the RMS roughness in PEAI treated films was observed (Figure 3.4).

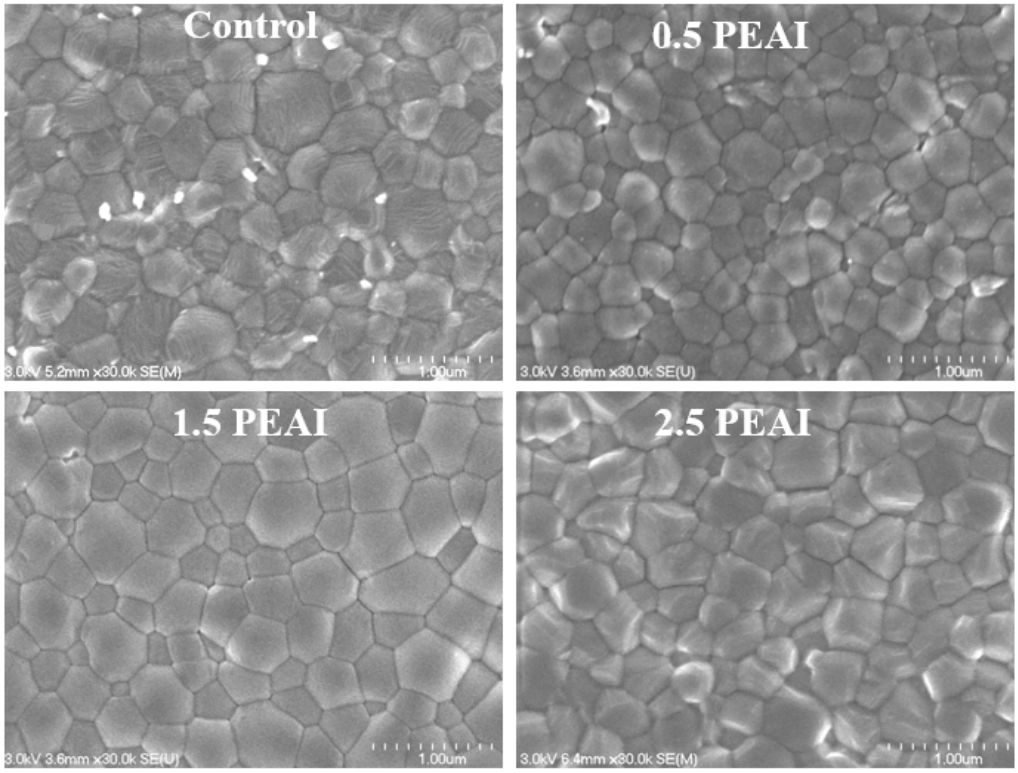

Figure 3.3. Top view SEM micrograph images of perovskite films (All scale bar has a dimension of 1 μm).

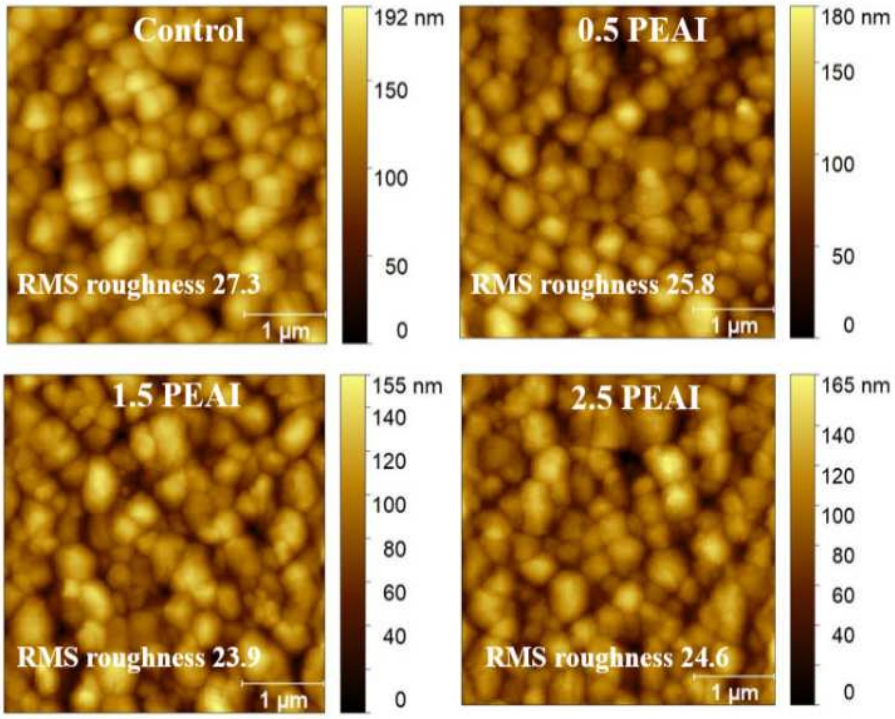

Figure 3.4. AFM topography images of perovskite films (All scale bar has a dimension of 1 μm).

To see the impact of PEAI doping in perovskite film crystallinity, we performed an XRD experiment. As shown in figure 3.5 (a) ,the formation of perovskite was confirmed with observed diffraction peaks at 2θ of 14.09° and 28.2°, 32°, 41° can be assigned to (110), (220), (310), and (214) lattice planes of the perovskite crystals respectively. A peak at 12.5° can be assigned to an uncoordinated PbI_2/SnI_2 complex. There exist no new peaks for the PEAI doped films and is like diffraction pattern of control film. This confirms that no 2D phases were formed in the PEAI doped cell. To further explain the effect of PEAI doping into the perovskite precursor, full width half maximum (FWHM) and peak intensity of perovskite main characteristics peak at 14.1° was estimated for each perovskite film (figure 3.5 b). The FWHM value for 1.5 PEAI narrowed down to 0.22° from 0.32° for the control perovskite film, signifying the improved crystallinity of PEAI doped perovskite films. Additionally, perovskite peak intensity increased with increasing the PEAI concentration

with showing best value at 1.5 PEAI.

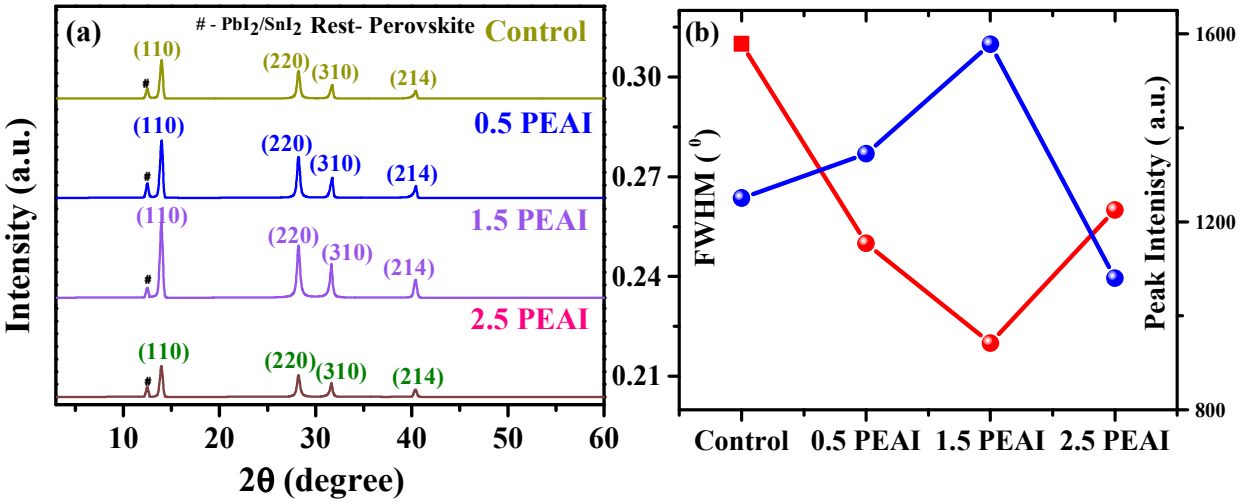

Figure 3.5. (a) XRD pattern of perovskite films with and without PEAI addition, (b) Full Width half Maximum (FWHM) and peak intensity profile of perovskite films with various addition of PEAI.

Since, 1.5 PEAI films showed better absorbance, crystallinity, less surface roughness, and compact film morphology than other doping concentrations, we considered control and 1.5 PEAI films for further characterizations.

To further understand the film quality after the of PEAI doping, electronic disorder also known as Urbach energy was estimated by linear fitting ln (α) vs. hγ profile using the relation $\alpha = \alpha_0 \text{ Exp } (E/E_u)$, where α is the absorption coefficient, E (=hγ) is the photon energy, and E_u is the Urbach energy [31]. As shown in figure 3.6 (a), the control sample has $E_u \sim 100.95$ meV, where 1.5 PEAI showed reduced value of 64.28 meV. The perceived reduction in the Urbach energy is a hint of reduced trap densities in the 1.5 PEAI film and is in a good agreement with steady-state photoluminescence (PL) study of perovskites films (figure 3.6 b), where 1.5 PEAI film showed higher PL strength than control film suggesting

the reduction in non-radiative recombination loss due to PEAI doping.

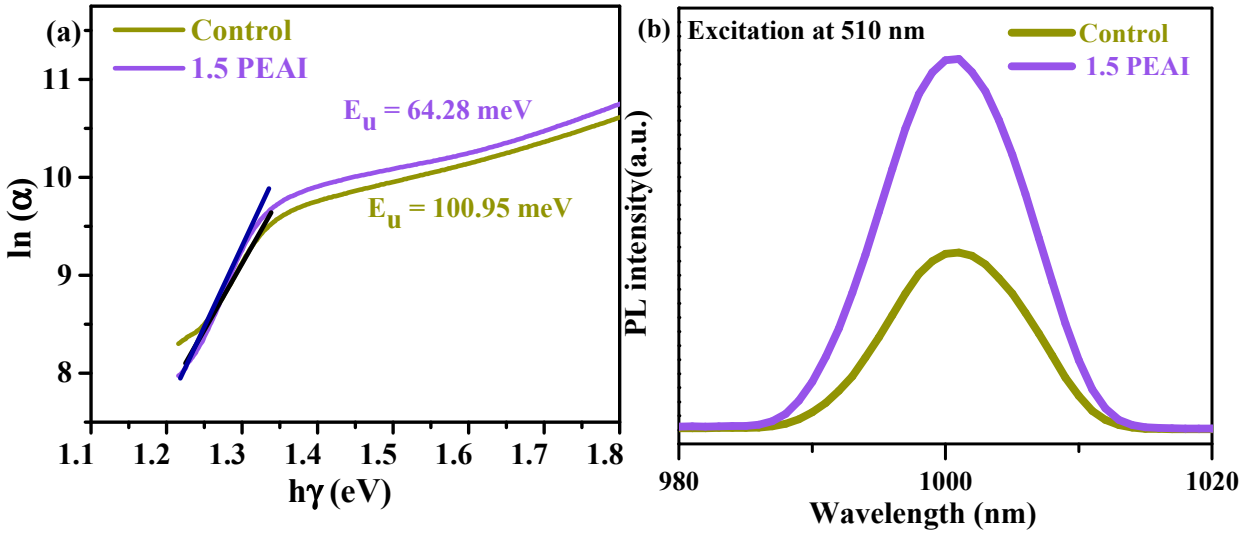

Figure 3.6. (a) Estimation of Urbach energies of control and 1.5 PEAI films. (b) Steady-State Photoluminescence profiles of control and 1.5 PEAI films.

3.2.2.1 Possible defect passivation mechanism using PEAI

The overall defect passivation mechanism using PEAI is presented in figure 3.7. NH_3^+ in PEAI can coordinate with Lewis acids such as PbI_2 and SnI_2 and form coordination bonds. The coordination bonds are useful during the perovskite crystallization as Sn tend to crystallize faster than Pb counterpart. Coordination bond binds the uncoordinated Sn molecules with perovskite crystal lattice by forming lewis-base adduct in perovskite film. Besides, iodide (I^-) in PEAI can provide excess iodide to reimburse the iodide vacancies [91, 92]. In addition, the rapid oxidation of Sn^{+2} into Sn^{+4} can be inhibited by the hydrophobic phenyl ring of PEAI [36, 49, 93]. This advises the defect passivation ability of PEAI salt by passivating both positive and negative defects.

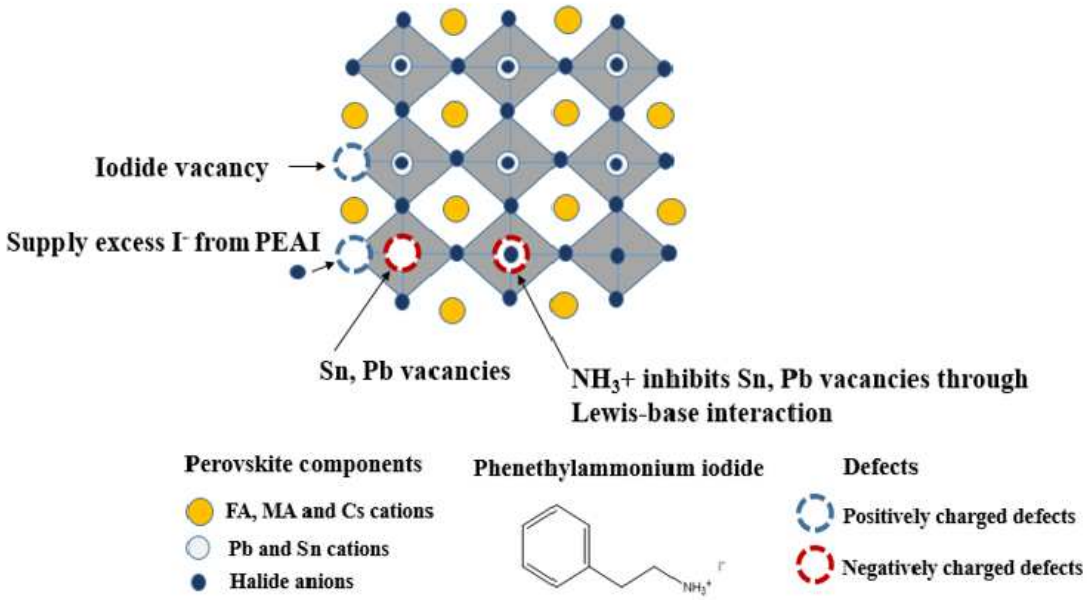

Figure 3.7. Schematics for possible defects passivation mechanism using PEAI.

To verify the possible defect passivation mechanism, we conducted Raman spectroscopy of PEAI-PbI_2, and PEAI-SnI_2 complexes [94]. Since, N in PEAI has Sp3-hybridization with electronic configuration as $1s^2$ $2s^2$ $2p^3$ where three hybridized orbitals can form three covalent bonds. One leftover lone pair of electrons has tendency to interrelate with other hybridized orbital via formation of a coordination bond [91, 94]. The delocalization of such lone pair electrons into the empty orbitals of Pb^{+2} or Sn^{+2} is beneficial for perovskite crystallization as it can extend the crystallization process for smooth, compact and defects free morphology. As shown in figure 3.8 (a), strong vibrational bands near 1076 and 1250 cm^{-1} can be credited to the Sn-N bond formation via delocalization of lone pair electron of PEA upon deprotonation N into the empty orbital of Sn^{+2} [95]. On the other hand, PEAI-PbI_2 complex showed a new peak at 131 cm^{-1} and peak shifts from 482 to 423, 818 to 842 and 1004 to 1052 cm^{-1} which can be ascribed to the Pb-N vibration[96].These interactions are further illustrated by graphical schematic in figure 3.8

(b). In addition, the evidence of the compensation of halide vacancies by excess iodide from PEAI was also supported by energy dispersive spectroscopy (EDS). As depicted in figure 3.9, upon PEAI doping iodide Wt. % increased as compared to that of control, suggesting that excess iodide from PEAI can fill the iodide vacancies created during the perovskite formation process.

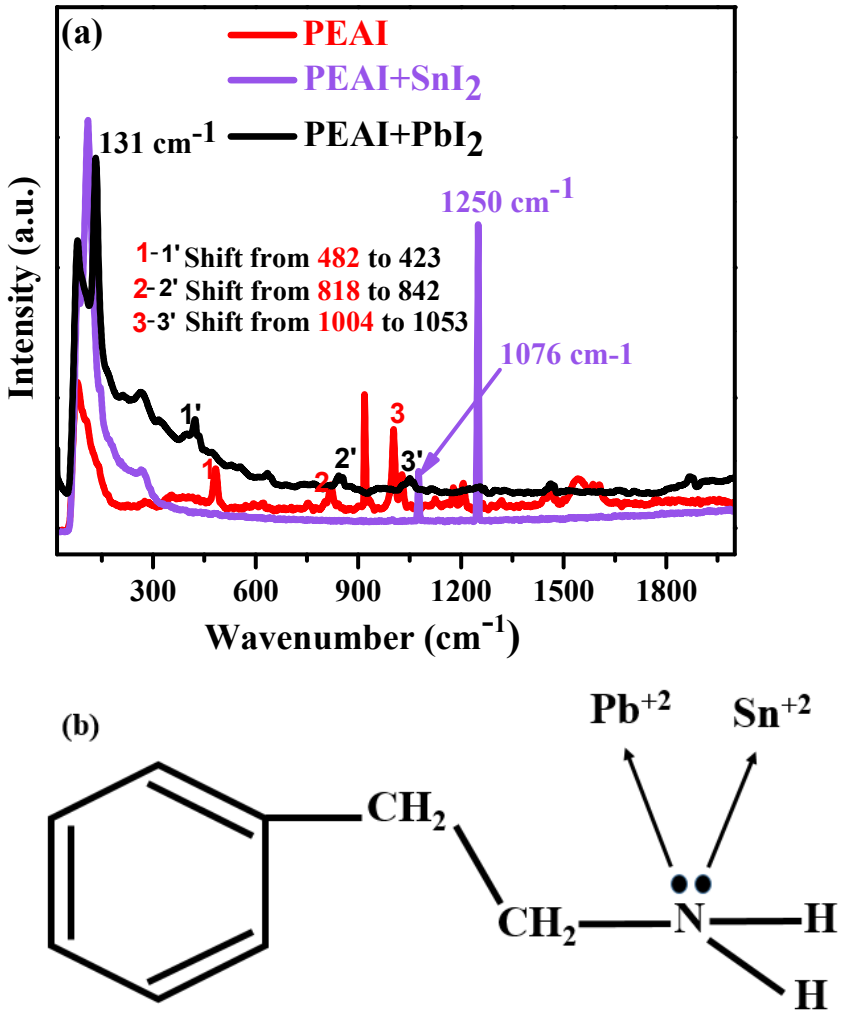

Figure 3.8. (a) Raman spectra of PEAI powder, PEAI-PbI_2 and PEAI-PbI_2 complexes. (b) Possible coordination mechanism of lone pair electrons in PEA with Sn^{+2} and Pb^{+2}.

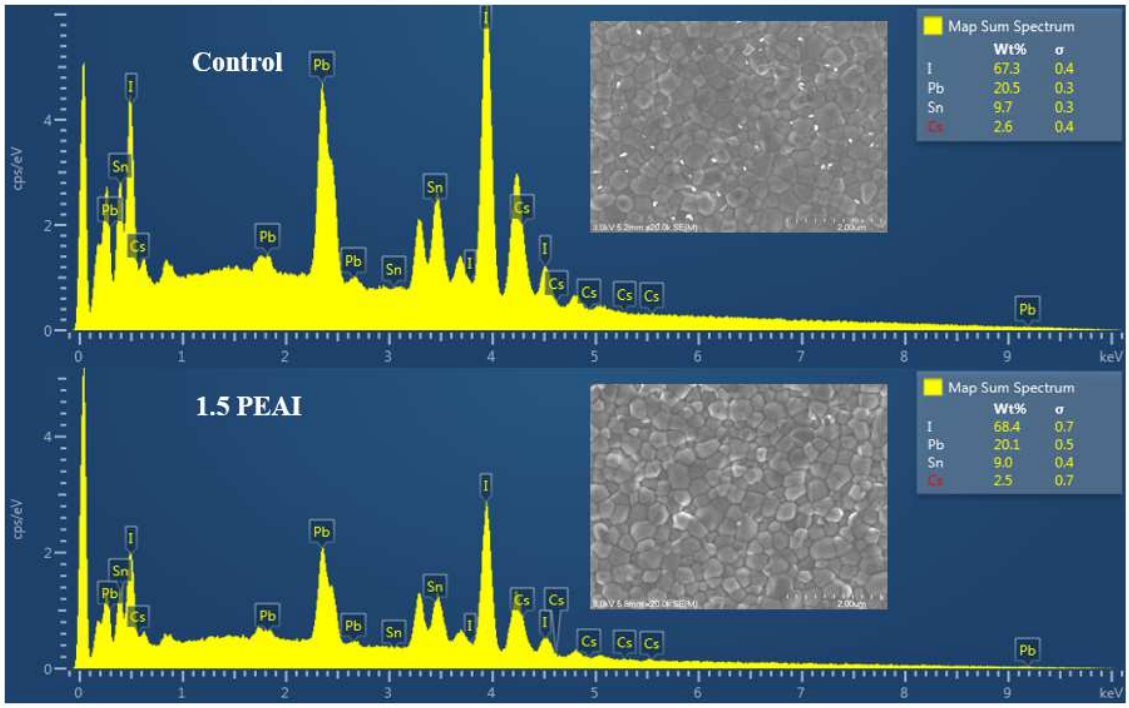

Figure 3.9. EDS results of control and 1.5 PEAI doped perovskite films for elemental Wt. % calculation.

3.2.3 Performance study of solar cells

To corroborate the improvements on the perovskite film quality as evidenced with optical, electrical, and physical properties of PEAI doped perovskite films, we fabricated complete solar cells in several batches. Figure 3.10 shows J-V curves for PSCs with and various addition of PEAI. As expected, 1.5 PEAI showed the best performance, delivering an excellent average PCE of 16.98%.The corresponding statistics of photovoltaic (PV) parameters are summarized in Table 3.1. The average value of corresponding parameters is followed by standard deviation and best value is enclosed by a parenthesis. Statistics were obtained from 25 best performing devices for each condition.

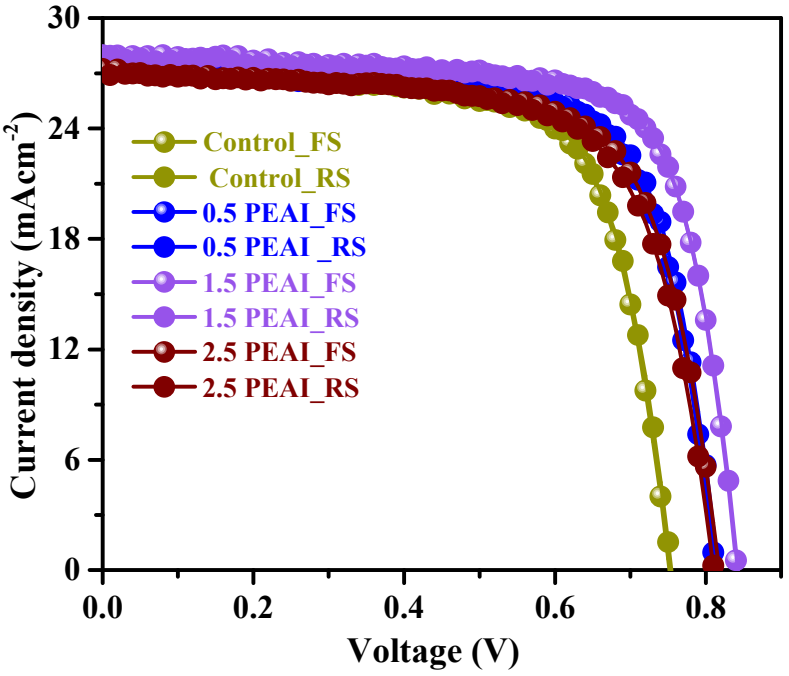

Figure 3.10. J-V curves of PSCs without and with various addition amount of PEAI.

Table 3.1. PV parameters of PSCs without and with various addition amount of PEAI.

Devices	V_{OC} (V)	J_{SC} (mA cm^{-2})	FF (%)	PCE (%)
Control	0.73 ± 0.02 (0.76)	26.89 ± 0.6 (27.49)	64 ± 0.02 (70.00)	13.84 ± 0.7 (14.61)
0.5 PEAI	0.79 ± 0.04 (0.82)	26.93 ± 0.5 (27.42)	68 ± 0.03 (71.23)	14.93 ± 0.4 (16.01)
1.5 PEAI	0.83 ± 0.01 (0.85)	27.47 ± 0.20 (27.93)	72 ± 0.01 (73.13)	16.98 ± 0.3 (17.33)
2.5 PEAI	0.80 ± 0.1 (0.82)	26.76 ± 0.4 (27.70)	67 ± 0.05 (69.51)	14.58 ± 0.6 (15.21)

Figure 3.11 (a) shows the J-V curves for best-performing control and 1.5 PEAI PSCs. Table 3.2 summarizes the PV parameters for control and best performing 1.5 PEAI devices for

both forward and reverse sweeps. The best PCE of 14.61 % was obtained for the control device in the reverse scan, demonstrating a short current density (Jsc) of 27.49 mA cm^{-2}, open-circuit voltage (V_{OC}) of 0.76 V, and fill factor (FF) of 69.97%. 1.5 PEAI device showed the best PCE of 17.33 % in a reverse sweep with significantly increased Voc of 0.85 V, FF of 73.13%, and Jsc of 27.89 mA cm^{-2}. V_{OC} loss of 1.5 PEAI device is only 0.4 V, which is 22.5% lower than in control with 0.76 V. This achieved Voc loss is among the least Voc loss reported with similar bandgap (1.2-1.27 eV). Additionally, the 1.5 PEAI device also showed a much lower hysteresis index of 0.14% compared to the control with 0.25 %. An external quantum efficiency (EQE) spectrum and corresponding integrated J_{SC} curves of control and 1.5 PEAI devices are shown in figure 3.11 (b)**.** The integrated J_{SC} obtained from the EQE measurement were 27.17 mA cm^{-2} and 27.59 mA cm^{-2} for the control and 1.5 PEAI devices, respectively, which are consistent with the J_{SC} extracted from the J-V curves.

For stable output power (SPO) measurement, devices were biased at respective maximum power outputs. SPO for control and 1.5 PEAI devices were found to be 14.31% and 17.01%, respectively (figure 3.11 c). Figure 3.10 (d) shows the V_{OC} histogram of 25 devices each for control and 1.5 PEAI conditions. An average V_{OC} of 0.83 V is acquired for 1.5 PEAI devices compared to the control with 0.73 V. The 100 mV increase in average Voc indicates the impact of the PEAI doping. Figure 3.10 (e) shows the PCE histogram of 25 devices for each condition. 1.5 PEAI devices showed the best average PCE of 16.98%, whereas the control devices showed 13.84 %. More than 75% of 1.5 PEAI devices showed a PCE > 17%, indicating good repeatability, whereas control devices showed lower PCE with much wider dispersion.

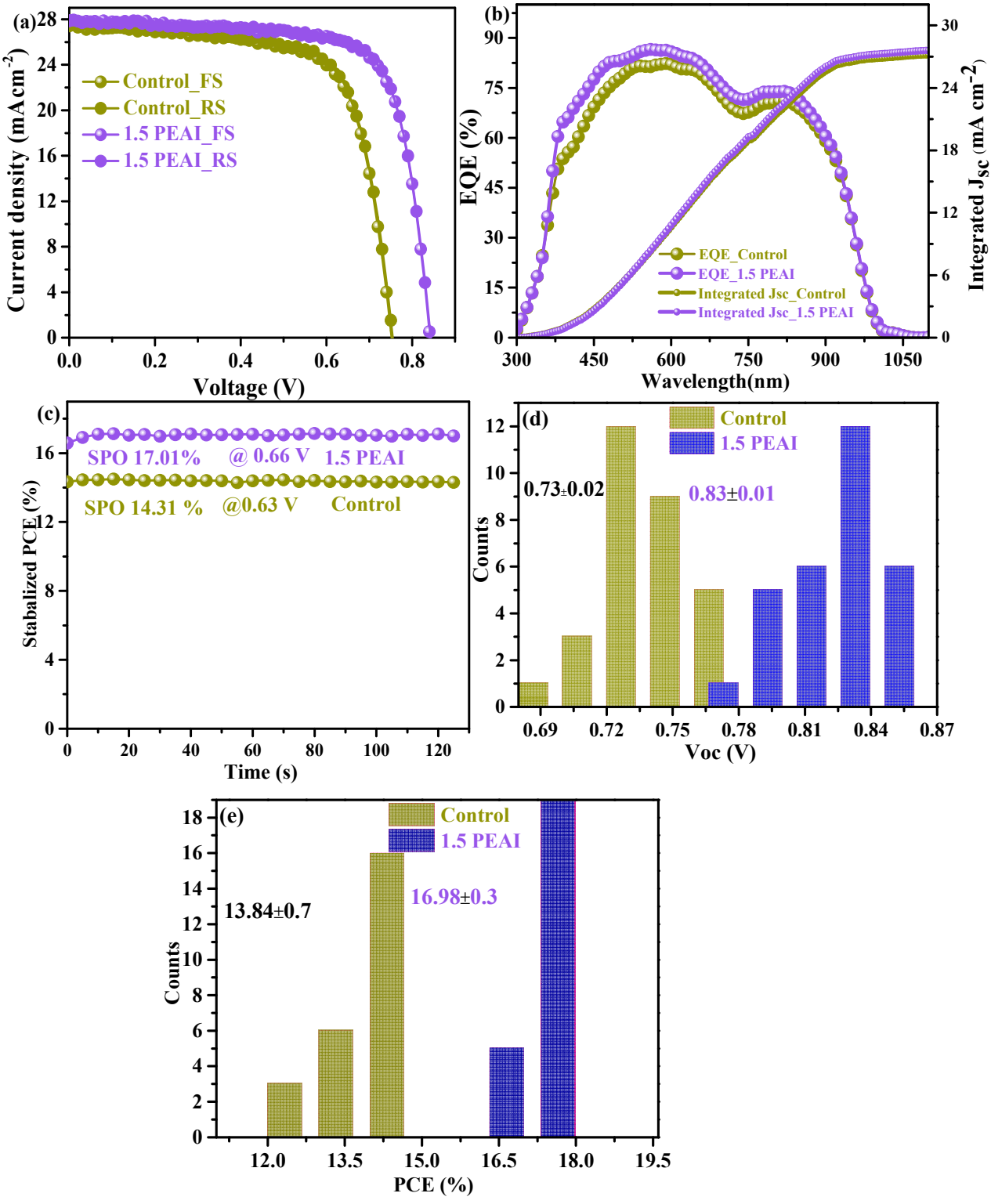

Figure 3.11. (a) J-V curves, (b) EQE profiles, (c) Stabilized power outputs (d) V_{OC} histogram, and (e) PCE histogram for control and 1.5 PEAI PSCs.

Table 3.2. Photovoltaic parameters of best performing control and 1.5 PEAI devices with both forward and reverse sweeps.

Devices	Scan	J_{sc} (mA cm^{-2})	V_{oc}(V)	FF (%)	PCE (%)	HI (%)
Control	Forward	27.42	0.75	70.00	14.39	0.25
	Reverse	27.49	0.76	69.97	14.61	
1.5 PEAI	Forward	27.93	0.84	73.00	17.12	0.14
	Reverse	27.89	0.85	73.13	17.33	

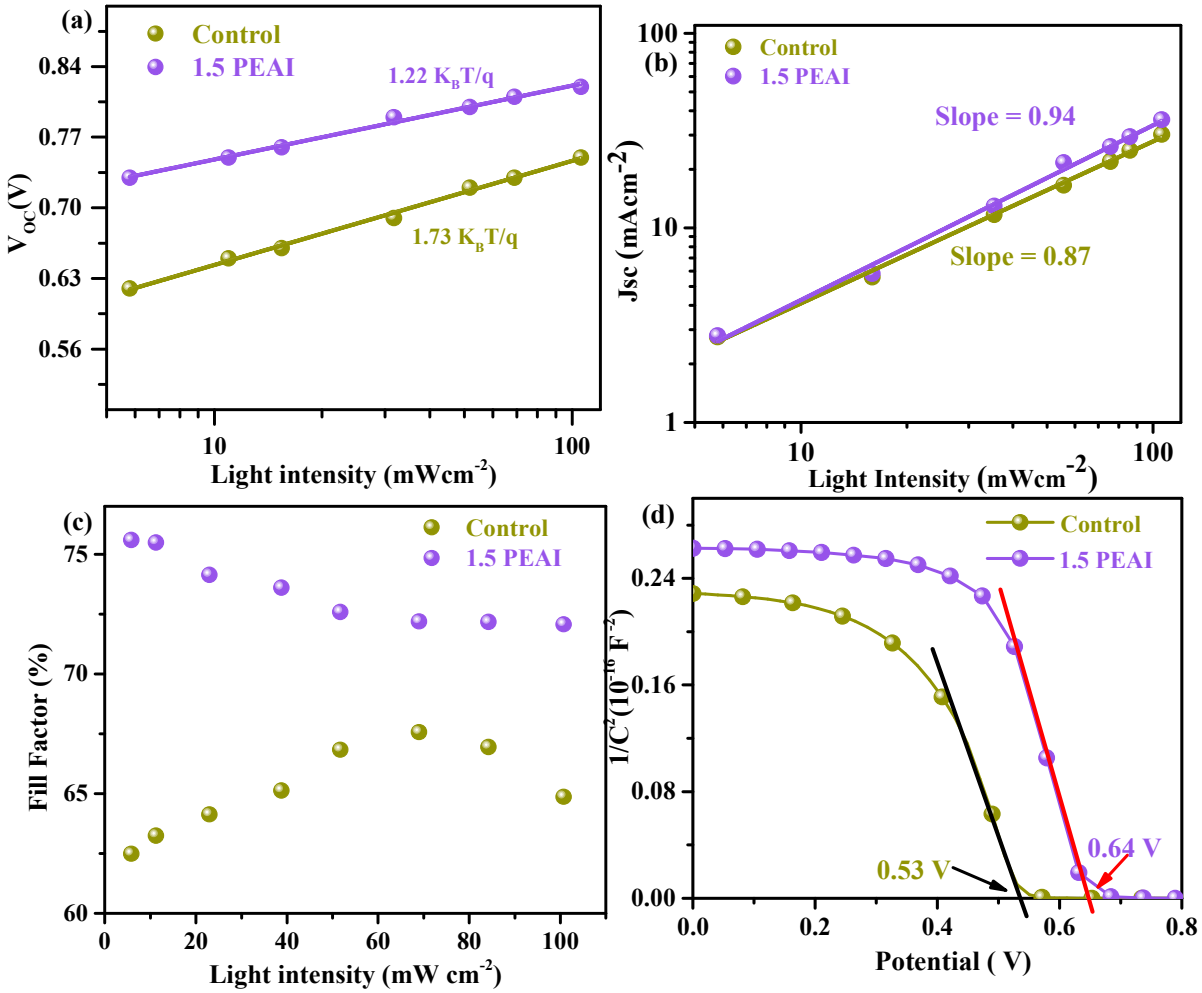

Figure 3.12. Light intensity dependence of (a) V_{OC}. (b) J_{sc}. (c) FF of control and 1.5 PEAI devices. (d) Mott-Schottky profiles of control and 1.5 PEAI devices at 20 KHz under dark

condition.

The most likely impact of PEAI doping was revealed in an enhancement of V_{OC} and FF. Understanding charge recombination and charge extraction mechanics in the PSCs is helpful to study the effect of PEAI incorporation on the perovskite. For this, we conducted a light intensity dependence test on V_{OC}, J_{SC}, and FF by simply varying the incident light intensities on the solar cell and recording voltage and current responses at different intensities. Splitting of the quasi-Fermi levels of electrons and holes is directly related to V_{OC}, where free charge carrier concentrations set up quasi-Fermi level positions [31, 66]. The relationship between V_{OC} and light intensity (I) is given by,

$$V_{OC} = \frac{nKT}{q} \ln\left(\frac{I}{I_0}\right) \tag{3.1}$$

Where n represents the diode ideality factor, q is an elementary charge, k is the Boltzmann constant, and T is the temperature. In ln (light intensity) vs. V_{OC} profile, deviation of the slope KT/q from unity indicates the dominance of trap-assisted monomolecular Shockley-Read-Hall (SRH) recombination. As the value of n approaches 2, the recombination is solely due to traps. As shown in figure 3.12 (a), the 1.5 PEAI device showed a lower value of ideality factor (1.22) than that of the control (1.73), indicating the dominance of bimolecular recombination in the 1.5 PEAI devices, whereas trap assisted SRH recombination in the control devices. Moreover, 3.12 (b) shows the light intensity dependence of J_{SC}, where 1.5 PEAI device displays a higher slope of 0.94 compared to control with 0.87, suggesting the reduced extent of non-radiative trap-assisted recombination and better charge extraction with PEAI incorporation.

These observations are further validated by performing the light-dependent fill factor (FF)

tests, as shown in 3.12 (c). The FF is related to trap filling, which occurs at a low light intensity of photo-generated charge carriers, and bimolecular recombination, which occurs at a high density of photo-generated carriers [51, 87-89]. In the 1.5 PEAI device, the value of FF decreased initially up to 45 mW cm^{-2} and then remained almost constant at higher light intensities. This hints at the reduced extent of trap-assisted recombination in the 1.5 PEAI device, as better FF is expected at low light intensity (low carrier density). Conversely, FF increased with increasing the light intensity up to 65 mW/cm^{-2} in control devices and then decreased with further increment in light intensity. This advises the dominance of trap-assisted recombination in the control devices as more photo-generated charge carriers are needed to fill the traps.

These findings align with the V_{OC} vs. light intensity test, suggesting that both bimolecular and trap-assisted recombination dominate the control and PEAI treated devices. However, the extent of the trap-assisted recombination is less severe in the 1.5 PEAI devices compared to the control.

We also performed capacitance-voltage (C–V) measurements to reveal the probable mechanism accountable for V_{OC} improvement. As shown in Mott-Schottky profile in figure 3.12 (d), higher built-in potential (Vbi) ~ 0.64 V was obtained for 1.5 PEAI device compared to control device with ~ 0.53 V, indicating the presence of a stronger electric field at 1.5 PEAI interface that facilities the better charge transport through the device [37, 97-100]. Additionally, the background hole carrier density is higher in the control device than that of 1.5 PEAI devices as the slope of the M-S plot is higher for 1.5 PEAI PSCs. This indicates a reduced capacitive effect due to the reduced extent of oxidation of Pb-Sn films with the introduction of hydrophobic PEA^{+}. These conclusions

are consistent with other reports [101, 102].

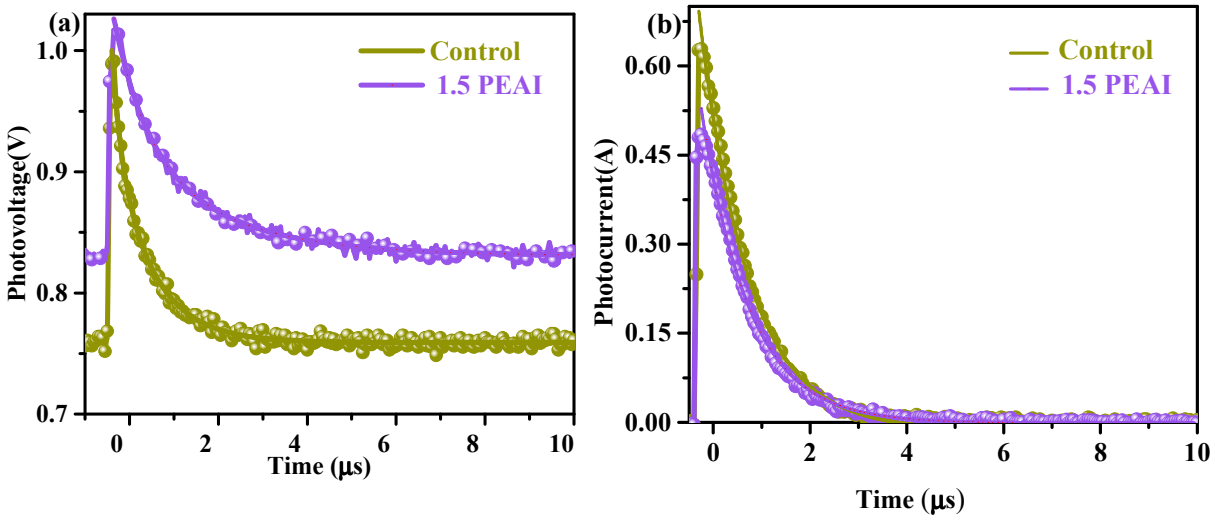

Figure 3.13. (a) TPV decay curves, b) TPC decay curves of control and 1.5 PEAI devices.

To see impact of the PEAI on carrier lifetime and transport time, we performed transient photo-voltage (TPV) and transient photo-current (TPC) measurements. As depicted in figure 3.13 (a) shows the transient photo-voltage decay profiles of the control and 1.5 PEAI devices. The charge recombination lifetime or charge carrier lifetime (τ_{rec}) was calculated from fitting of the exponential decay curve with mono-exponential function. The value of τ_{rec} for the treated device was found to be ~2.14 μs which is longer than that of control with ~0.99 μs. Figure 3.13 (b) shows the transient photo-current decay profiles of the control and 1.5 PEAI devices. Devices were kept under short circuit current conditions using a low input impedance of ≈50 Ω and excited by a nanosecond laser pulse without background light. The value of charge transport time (τ_{tr}) for each case were calculated via exponential fitting of TPC curves and it was found that τ_{tr} decreased from

~0.94 µs for the control to ~0.87 µs for the 1.5 PEAI device indicating better charge transport with the PEAI incorporation. These improvement in charge carrier dynamics further indicate defect passivation ability of the PEAI.

To back up the results obtained from TPV and TPC, we performed the study of charge transfer dynamics measuring impedances at frequency range of 1 Hz-1 MHz using electrochemical impedance spectroscopy (EIS).The results obtained from the measurement were fitted with commonly used one R-C circuit [19, 75, 103-106] as shown in the Nyquist plot in figure 3.14 (a). Figure 3.14 (b) shows the equivalent circuit table 3.3 lists the corresponding fitting parameters. The control device demonstrated recombination resistance (R_{rec}) of ~5 KΩ, whereas the 1.5 PEAI devices showed ~12 KΩ. This indicates a low recombination rate enabled with the PEAI doping, further confirming the observed increase in V_{OC} and FF.

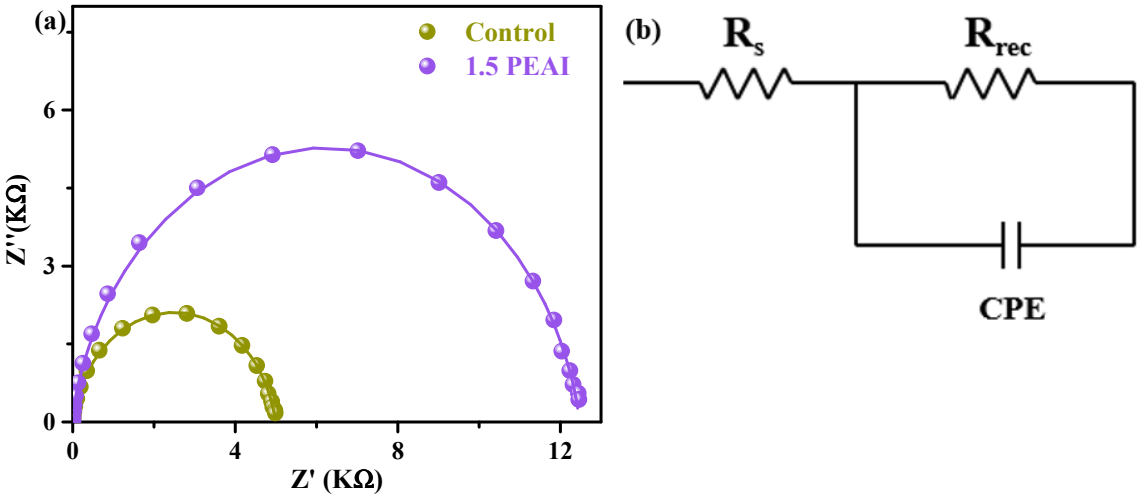

Figure 3.14. (a) Nyquist plots of control and 1.5 PEAI PSCs, and (b) Equivalent one RC-circuit.

Table 3.3. EIS fitting parameters of control and 1.5 PEAI devices

Device	R_s (Ω)	R_{rec} (KΩ)	CPE(nF)
Control	34.8	4.99	15.9
1.5 PEAI	29.4	12.45	13.1

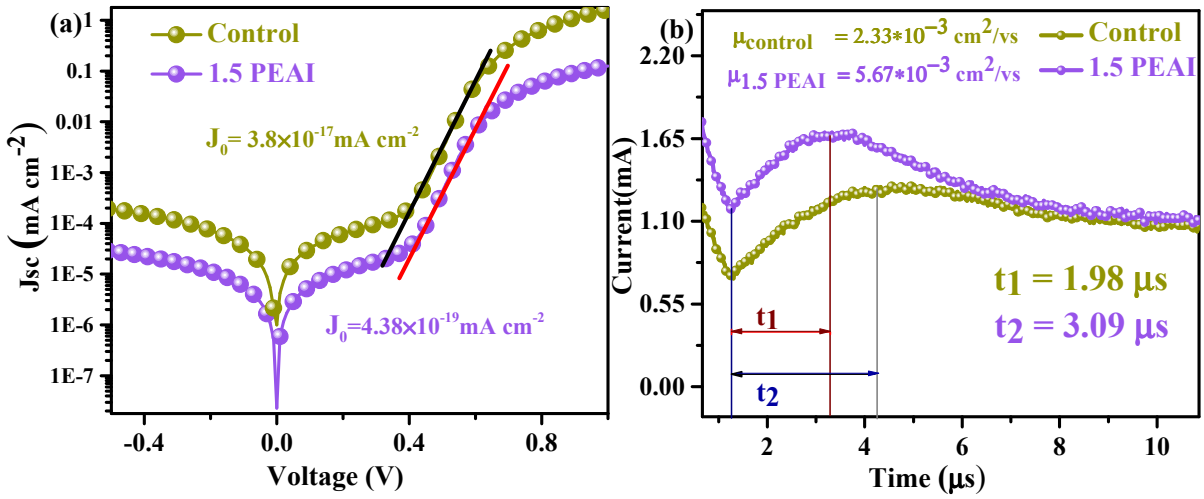

Figure 3.15. (a) Dark J-V curves of control and 1.5 PEAI PSCs, and (b) Photo-CELIV profiles of control and 1.5 PEAI solar cells.

Figure 3.15 (a) presents dark J-V curves for control and 1.5 PEAI devices. The control device has a reverse saturation current density of 3.8 ×10^{-17} mA cm^{-2}. In the 1.5 PEAI device case, the value significantly decreases to 4.38 ×10^{-19} mA cm^{-2} indicating a reduced number of traps with PEAI incorporation [107].Figure 3.15 (b) presents the charge carrier mobility measurement using photo-CELIV. Experiment showed higher value of mobility 5.67 x 10^{-3} cm^2 $v^{-1}s^{-1}$ for 1.5 PEAI devices compared to control with 2.33 x 10^{-3} cm^2 $v^{-1}s^{-1}$. The higher value of mobility is attributed to the better charge transport and less

carrier recombination with the PEAI treatment.

3.2.3.1 Stability analysis of perovskite solar cells

The performance of solar cells is determined by their film properties, PV parameters and the stability. To study the effect of PEAI on the PSCs stability, we performed the stability tests of unencapsulated devices by tracking the evolution of PCE and V_{OC} over time while storing the devices in ambient and controlled (N_2 filled glovebox) conditions.

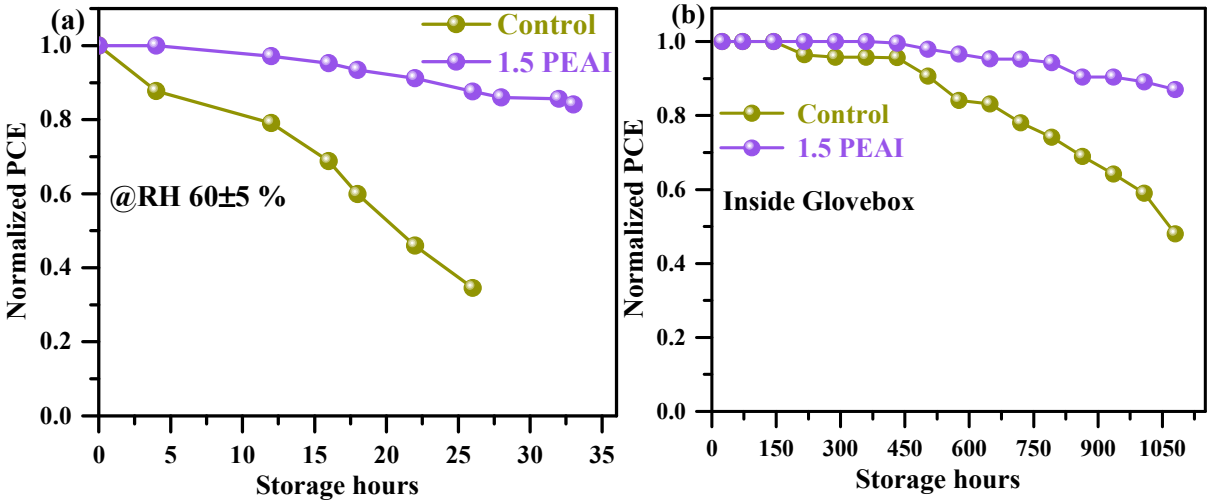

Figure 3.16. Ambient and dark shelf stabilities of control and 1.5 PEAI devices. (a) PCE evolution at ambient. (b) PCE evolution at N_2 environment.

Figure 3.16 (a) shows that the PCE of 1.5 PEAI devices retained almost ~85% of initial PCE over a storage period of 36 hours outside at ambient atmospheric condition of RH 60±5%, while the control device only lasted for 27 hours. The PCE retained by 1.5 PEAI PSCs while storing the devices in a controlled N_2 environment for 1050 hours was found to be ~87 %, while the control PSCs could only retain only 47% of the initial PCE for the same storage period (figure 3.16 b).

V_{OC} evolution over time by control and 1.5 PEAI was also performed. The V_{OC} of 1.5 PEAI devices retained almost ~90 % of the initial V_{OC} over a storage period of 36 hours outside at ambient atmospheric conditions of RH 60±5%, while the control device only could retain 28% V_{OC} for the same storage period lasted for 27 hours as shown in figure 3.17 (a). The V_{OC} retained by 1.5 PEAI PSCs while storing the devices in a controlled N_2 environment for 1050 hours was found to be ~98 %, while the control PSCs retained only 63 % of initial V_{OC} for the same storage period (figure 3.17 b).

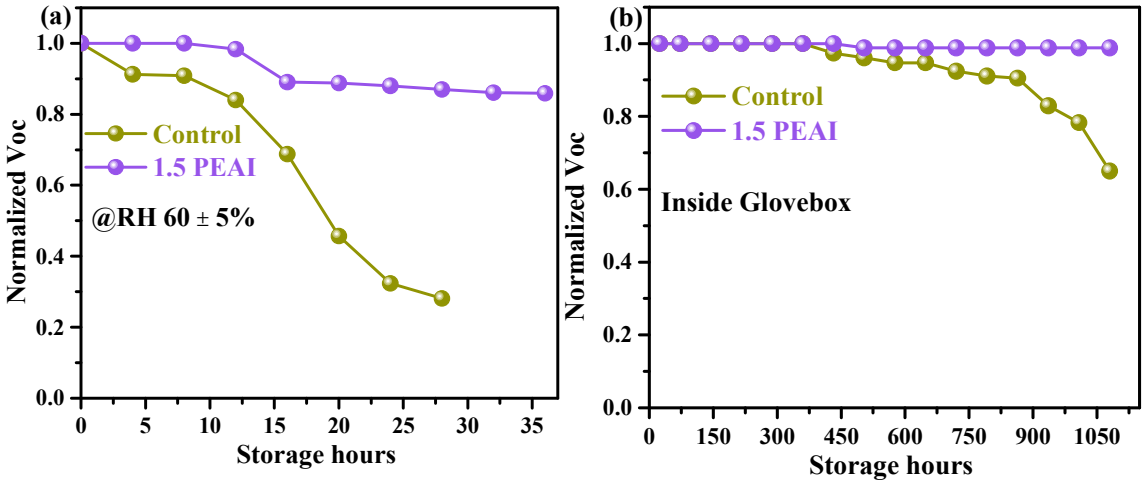

Figure 3.17. Ambient and dark shelf stabilities of control and 1.5 PEAI devices. (a) V_{OC} evolution at ambient. (b) V_{OC} evolution at N_2 environment.

To further confirm enhanced stability of PEAI doped devices, we experimented with perovskite solution by keeping each of the perovskite solutions outside the GB (RH 60±5%) for a certain period and carefully observing the change in solution color. As shown in digital photographs in figure 3.18 (a), 1.5 PEAI solution remained fresh even after 40 minutes of exposure, whereas control perovskite solution turned dark brown within 20 minutes of exposure. This suggests that even a trace amount of PEAI in perovskite

precursors can inhibit the oxidation of Sn. Furthermore, in figure 3.18 (b), the water contact angle measurement further validates the hydrophobicity of PEAI doped perovskite film, where 1.5 PEAI films showed a higher water contact angle of 68° compared to the control with 42°. Thus, the improved crystallinity and pinhole-free compact perovskite film morphology and hydrophobicity of PEAI-doped perovskite films might have a combined effect on the improved stability of 1.5 PEAI perovskite solar cells.

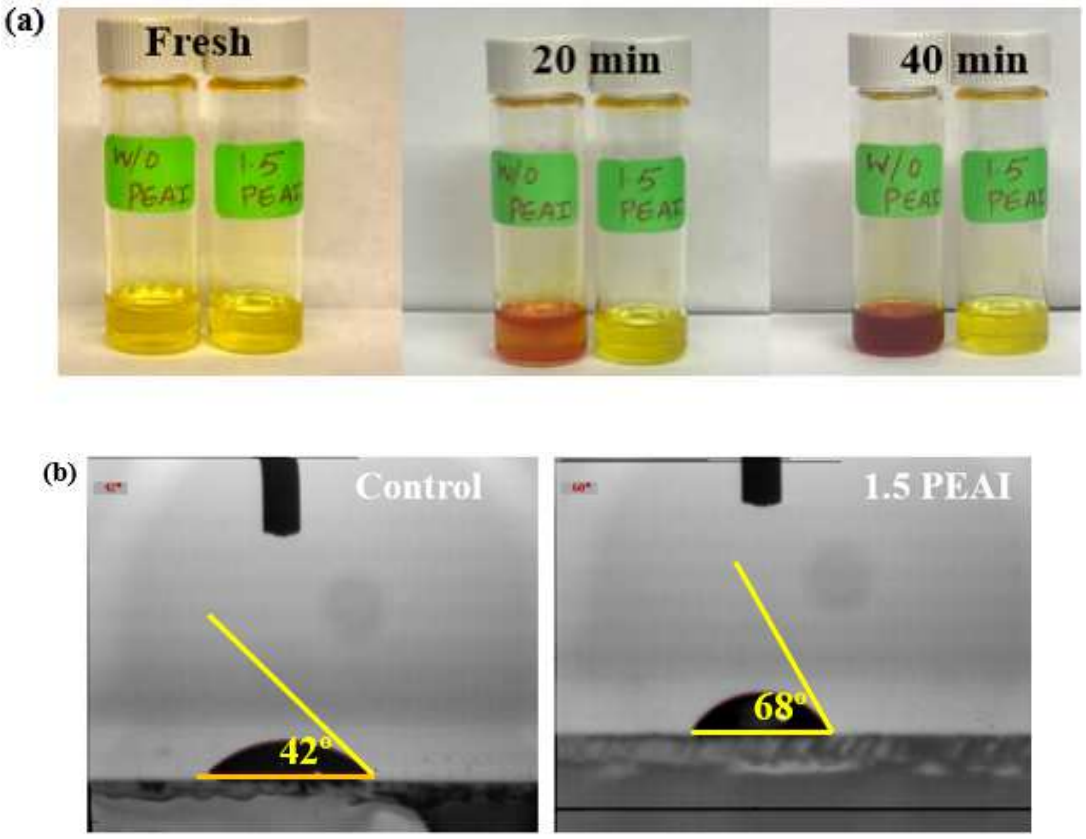

Figure 3.18. (a) Digital photographs of Pb-Sn perovskite precursors solutions without (control) and with 1.5 PEAI stored at ambient RH 60±5% for different time, (b) Water contact angle measurement of control and 1.5 PEAI perovskite films.

3.2.4 Conclusion

In summary, we developed a simple strategy to obtain high-quality Pb−Sn mixed low-bandgap perovskite films with smooth pinhole-free surface morphology, high crystallinity, and low electronic disorder by incorporating a suitable amount of PEAI for perovskite precursor doping. As a result, improvements were reflected on PV parameters. The high open-circuit voltage of 0.85 V achieved by our strategy corresponds to one of the least V_{OC} losses among similar Pb−Sn mixed low-bandgap perovskites while delivering a high PCE of 17.33% with negligible hysteresis. Furthermore, the ambient and dark self-stabilities of the PEAI-treated devices were significantly enhanced due to the hydrophobic nature of PEAI. Thus, this study paves a pathway to obtain defect-passivated, high-quality Pb−Sn mixed low-bandgap perovskite films with lower V_{OC} deficit and higher efficiency and stability.

CHAPTER 4 INTERFACE ENGINEERING OF LEAD-TIN MIXED LOW BANDGAP PEROVSKITE SOLAR CELLS FOR IMPROVED EFFCIEICNY AND STABILITY

4.1 Introduction

The power conversion efficiency (PCE) of Pb-Sn mixed low-bandgap (LBG) perovskite solar cell (PSCs) is inferior to that of pure lead-based medium bandgap counterpart because of large open-circuit voltage (V_{OC}) loss. The large Voc deficit is due to inefficient charge transport at perovskite surface and charge collection/perovskite interfaces because of facile oxidation of Sn^{2+} into more stable Sn^{4+}. In our work, we have designed and implemented a simple interface engineering strategy by inserting a thin layer of hydrophobic PTAA over the hydrophilic surface of PEDOT:PSS. The conductivity and mobility of the HSL layer improved with the HSL modification. The effect was reflected in the improved short circuit current density of PTAA modified devices. Evidently, the perovskite grains sizes were significantly enlarged, charge transportation dynamics were enhanced, which led to reduced density of traps. As a result, a high FF of ~ 80% % was obtained with significantly increased V_{OC} up to 0.85V. The V_{OC} obtained with this strategy is among the best V_{OC} obtained for Pb-Sn hybrid perovskite solar cells. Furthermore, a significant enhancement in PCE (16.04%) for pristine PEDOT:PSS to 19.41% was obtained with the PTAA modified HTL PSCs. Furthermore, the stability of unencapsulated devices was also enhanced where 84% and 80% of initial PCEs were retained by PTAA modified PSCs under the dark condition in N_2 for 1100 hours and under continuous illumination in N_2 environment for 108 hours, respectively. This work offers a simple interface engineering strategy to improve the PCE and mitigate the V_{OC}-loss of Pb-Sn mixed low-bandgap perovskite solar cells.

KEYWORDS: Interface passivation, HSL modification, PTAA, grain growth, low-bandgap perovskite, Pb-Sn mixed perovskite, V_{oc} loss, stability improvement

4.2 Result and Discussion

At first, optimization of PTAA concentration was performed. Then, different amounts of PTAA were dissolved in chlorobenzene (CB) and spin-coated on top of PEDOT: PSS-coated films. For ease of explanation, notation such as Reference, 0.3 PTAA, 0.6 PTAA, and 0.9 PTAA were assigned to the films and devices made with pristine PEDOT:PSS, PEDOT:PSS /0.3mg of PTAA in 1 mL of CB, PEDOT: PSS/0.6 mg of PTAA in 1 mL of CB and PEDOT: PSS/0.9 mg of PTAA in 1 mL of CB respectively. The perovskite composition of $FA_{0.8}MA_{0.15}Cs_{0.05}Pb_{0.5}Sn_{0.5}I_3$ was chosen as the baseline composition for the films and devices fabrication. The composition was fabricated using the anti-solvent assisted single step spin-coating method and was tested several times to get the consistent film quality and optical bandgap.

4.2.1 Solar cell fabrication process

Figure 4.1 shows the complete solar cell fabrication process. Patterned ITO glasses were cleaned using soap mixed deionized (DI) water, DI water, acetone, and isopropyl alcohol for 25 minutes, sequentially under ultra-sonication. The substrates were then cured with UV-O_3 for 20 minutes. PEDOT: PSS layer was spin-coated at 6000 rpm/s speed / 5500 rpm/s acceleration for 40 s and immediately annealed at 140 ˚C for 20 min. For PEDOT:PSS /PTAA samples, different concentrations of PTAA dissolved in 1 mL of CB and was spin-coated over the PEDOT:PSS coated sample at the speed of 6000 rpm/s with the ramp of 2000 rpm /s. The samples were immediately annealed at 100 ˚C for 15 min

inside a nitrogen-filled glove box. For perovskite coating, 45 µL of perovskite solution was dripped over the PEDOT: PSS or PEDOT:PSS /PTAA coated surface and then spun at the speed of 750 rpm/s with the ramp of 500 rpm/s for 7 s and 5500 rpm/s speed with a ramp rate of 3000 rpm/s for 35 seconds. 180 µL of Ethyl-acetate was quickly cast over the spinning sample at 25th s at the second process. The substrates were then kept in a glass Petri dish for 5 min before annealing at preheated hotplate (90 ˚C for 10 minutes). After cooling down to room temperature, C_{60} (32 nm), BCP (8 nm) & silver (100 nm) were thermally evaporated inside a thermal evaporator under the vacuum of 5 $\times 10^{-6}$ Mbar. The initial deposition rate for C_{60} was kept ~ 0.05A˚/sec for 8-10 nm, then 0.2A˚/sec was used for the rest of the thickness. BCP was deposited at a rate of 0.15 A˚/sec for the entire thickness. The area of each device was 0.13 cm^2.

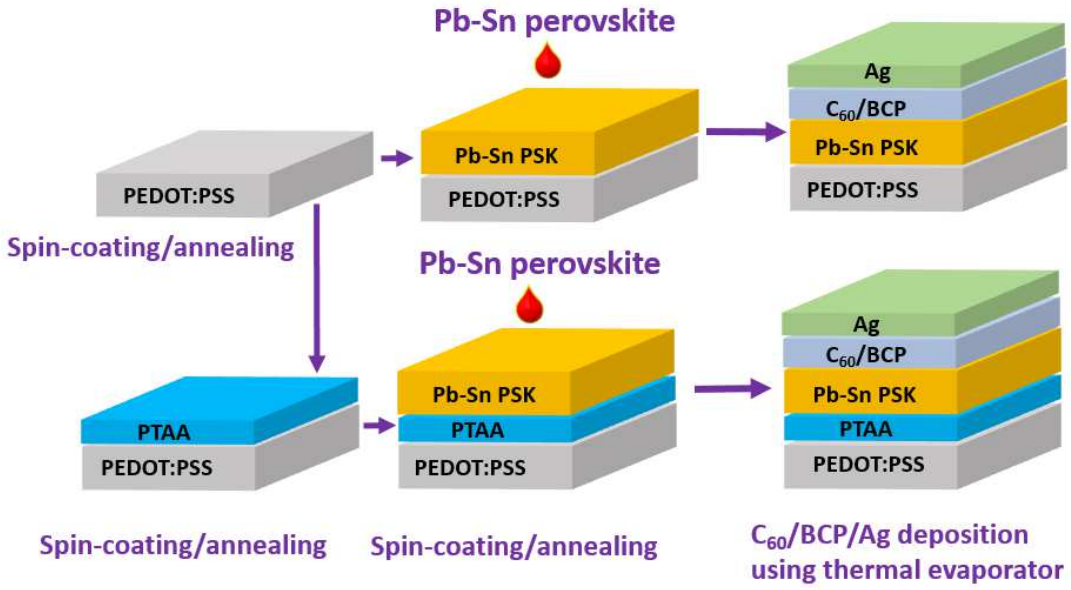

Figure 4.1. Low-bandgap perovskite solar cell fabrication process.

4.2.2 Optical, electrical, and physical properties of perovskite films

Figure 4.2 (a-d) shows an absorption spectrum, XRD pattern, FWHM vs intensity profiles

and steady state PL spectra of perovskite films grown on PEDOT:PSS and PEDOT:PSS/PTAA.

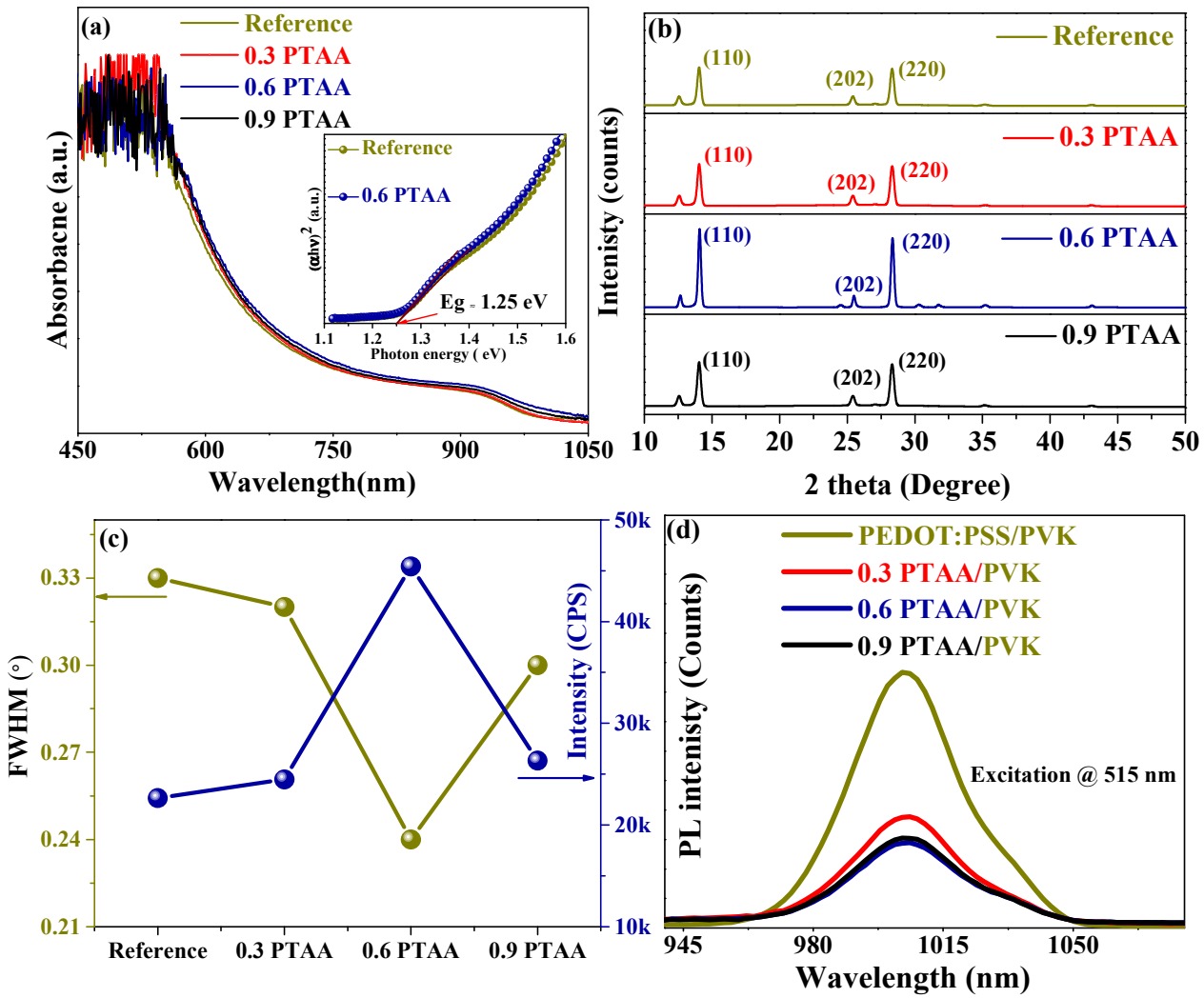

Figure 4.2. (a) Absorption spectra (Inset Tau-c plot of reference and 0.6 PTAA films), (b) XRD patterns, (c) FWHM and Intensity profiles, and (d) Steady state PL spectra of perovskite films grown on reference HSL, 0.3 PTAA, 0.6 PTAA, and 0.9 PTAA.

Figure 4.2 (a) shows the absorbance spectrum of reference and perovskite films grown upon 0.3 PTAA, 0.6 PTAA, and 0.9 PTAA, respectively. 0.6 PTAA perovskite film showed better absorbance than other concentrations of PTAA, and the optical bandgap

remained almost at 1.25 eV (Inset figure 4.2 a). We performed an XRD experiment to see the impact of HTL modification with PTAA in perovskite film crystallinity. As shown in figure 4.2 (b), the formation of perovskite was confirmed with observed diffraction peaks at 2θ of 14.09° and 28.2°, 32°can be assigned to (110), (220), lattice planes of the perovskite crystals, respectively. To study the effect of HTL modification, the full width half maximum (FWHM) of the perovskite peak at 14.1° was estimated for each perovskite film (figure 4.2 c). The lowest value of FWHM and highest peak intensity value was found to be for a 0.6 PTAA perovskite film, signifying the improved crystallinity of perovskite film grown on a 0.6 PTAA film. FWHM was also in good agreement with the steady-state PL result (figure 4.2 d), revealing that better quenching was achieved with a 0.6 PTAA sample. Efficient quenching is the hint of proper charge transport and less non-radiative recombination loss.

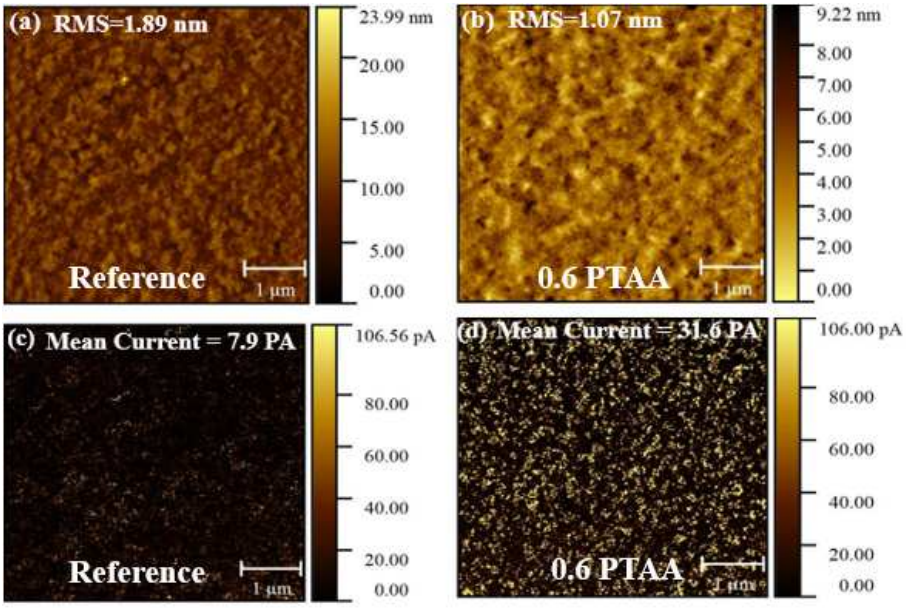

Figure 4.3. (a) AFM topography images of PEDOT: PSS film (b) AFM topography images of PEDOT: PSS/PTAA film. (c) CS-AFM images of PEDOT: PSS film (d) CS-AFM images of PEDOT: PSS/PTAA film.

Figure 4.3 (a-b) shows atomic force microscopy (AFM) topography images of reference and 0.6 PTAA films, respectively. The reference film showed a smooth morphology with RMS surface roughness of 1.89 nm. With the introduction of an ultrathin PTAA layer over the PEDOT: PSS layer, the film roughness decreased to 1.07 nm. We anticipated that the smoother underlying layer would help grow a compact and pinhole-free perovskite absorber layer. Figure 4.3 (c-d) presents CS-AFM images of reference film and modified HSL film, respectively. The local current distribution for each film was mapped to evaluate the average current on the films. The average current for reference film was found to be 7.9 pA, which significantly increased to 31.6 pA for modified HSL film, indicating enhancement on conductivity of hole transport layer due to deposition of PTAA

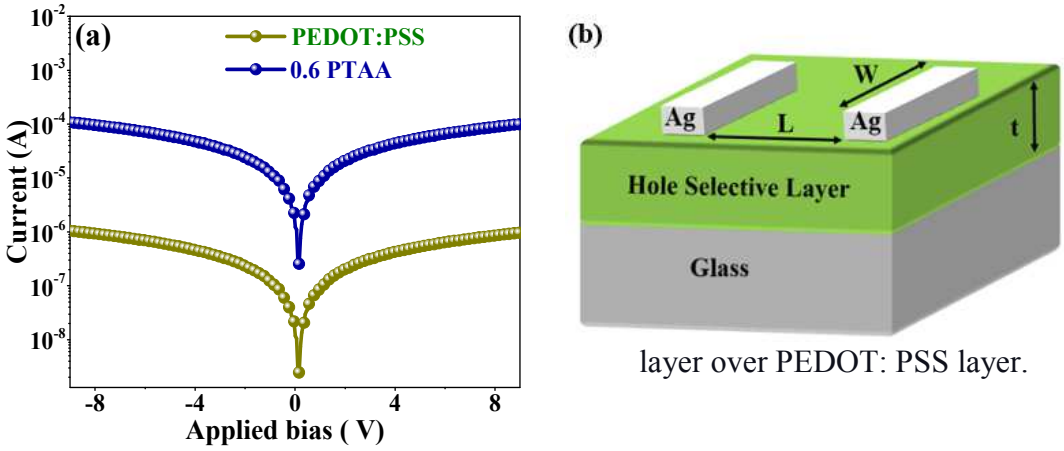

layer over PEDOT: PSS layer.

Figure 4.4. (a) In-plane I-V profiles of reference and modified HSL samples, and (b) Device structure used for in-plane *I-V* measurement.

To support the result obtained with CS-AFM, we performed conductivity measurement for the reference sample by recording in□plane current-voltage (*I–V*) data for every two adjacent electrodes. Figure 4.4 (a) shows in□plane current-voltage (*I–V*) characteristics curves for PEDOT: PSS film and PEDOT: PSS/ PTAA film. The device structure used for the experiment is shown in figure 4.4 (b). The film resistance *R* was

calculated from the gradient of *I–V* curves. Then, the conductivity values were calculated using the equation below.

$$\sigma = \frac{1}{R} \times \frac{L}{W \times t} \tag{4.1}$$

Where σ is film conductivity, *R* is film resistance, while *L*, *w*, and *t* are film length, width, and thickness, respectively.

The thickness of the reference sample was found to be ≈ 36 nm, whereas the thickness of 0.6 PTAA film was ≈ 38 nm as measured by the Dektek profilometer. PTAA deposition did not cause any significant change in the transmission spectrum (figure 4.5 a). The calculated conductivity for the reference film was found to be ≈ 8.014×10^{-3} S cm^{-1}, which significantly increased to ≈ 0.78 S cm^{-1} for 0.6 PTAA film. Intrigued by the enhancement of the conductivity of 0.6 PTAA film, we carried out the hole mobility measurement using the space-charge limited current method [103]. The hole□only diode devices were fabricated using the structures shown in 4.5 (b-c). The hole carrier mobility was calculated using Mott–Gurney equation.

$$\mu = \frac{8d^3}{9\,\varepsilon_0 \varepsilon_r}\left(\frac{J}{V^2}\right) \tag{4.2}$$

Where μ is hole carrier mobility, d is active layer thickness, is the dielectric permittivity of free space (8.85×10^{-12} F m^{-1}), is the dielectric constant of the active layer, J is current density, and V is applied bias. Figure 4.5 (d) shows the relation between $J^{1/2}$ versus applied bias V. The slope of the space charge region was linearly fitted from the profile, and mobility was calculated using equation 4.2. As expected, the hole mobility was increased

to 7.283×10^{-3} for the 0.6 PTAA film from 1.21×10^{-3} cm^2 Vs^{-1} for the reference film. We believed higher conductivity of 0.6 PTAA film and improved charge interface quality contributed to higher hole mobility for 0.6 PTAA films.

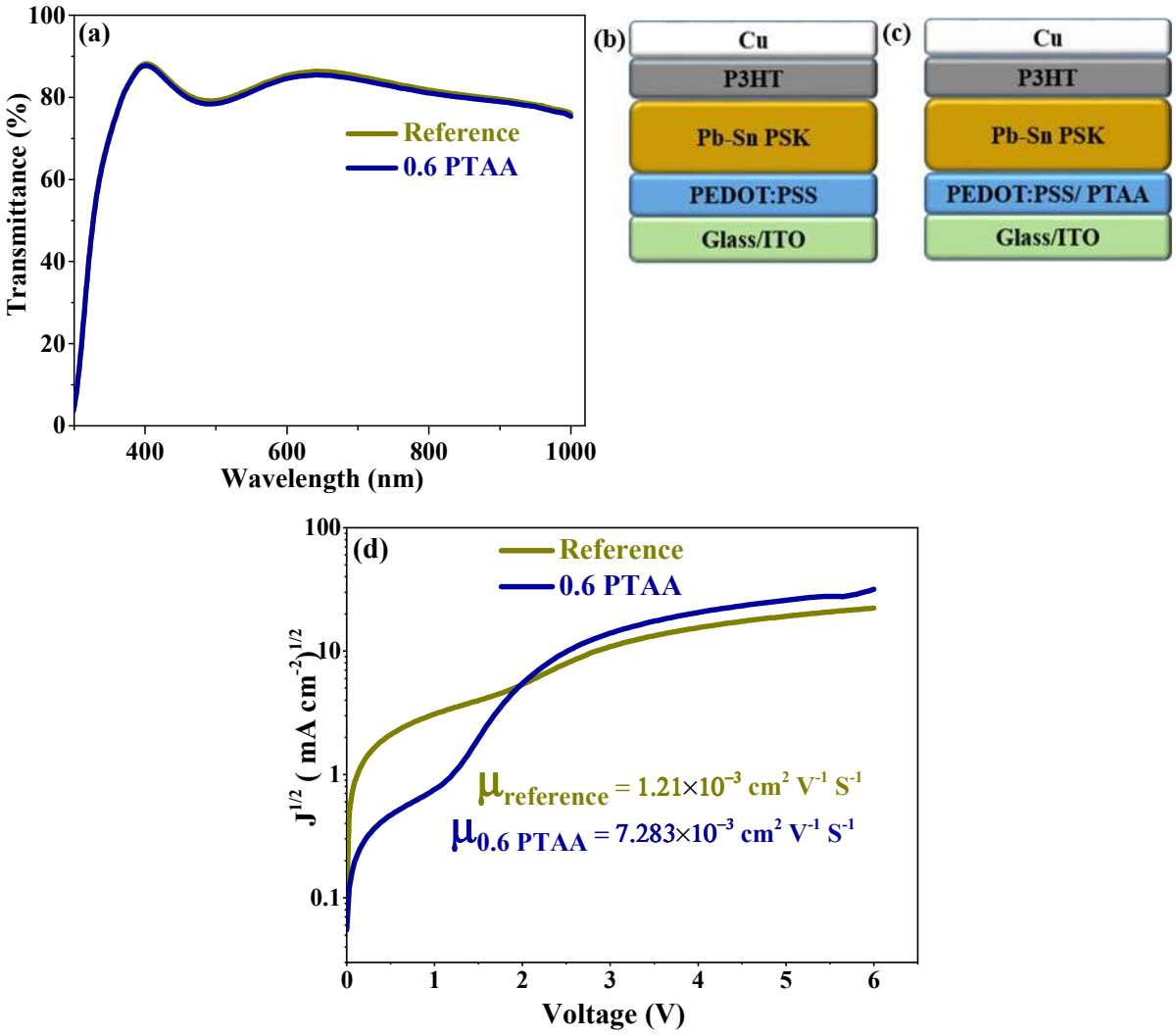

Figure 4.5. (a) Transmission spectra of reference and 0.6 PTAA films, (b-c) Device structures used as hole only device to estimate the hole carrier motilities using SCLC method for reference and 0.6 PTAA films respectively, and (d) $J^{1/2}$ versus applied bias V profile for extracting the slope in SCLC region to estimate the hole carrier motilities.

Fascinated by the fact that 0.6 PTAA HSL film possessed low surface roughness, higher conductivity, and mobility than the reference HSL film, we further investigated perovskite films grown on different HTL. As shown in figure 4.6 (a-d), the perovskite film morphology for the reference sample shows a compact-pinhole free surface. However, the orientation and sizes of the grain are inferior to that of 0.6 PTAA and 0.9 PTAA film surfaces. When perovskite film was grown on PEDOT:PSS/ PTAA layer, large grains with compact film morphology was obtained. In a polycrystalline film such as perovskite, larger grain size is essential to reduce the PSCs photo-voltage loss. Fewer grain boundaries are always preferred as the possibility of charge leakage would essentially minimize. The grain growth mechanism and the possible reason for bigger perovskite grain on PTAA modified HTL used perovskite films is explained later in this section.

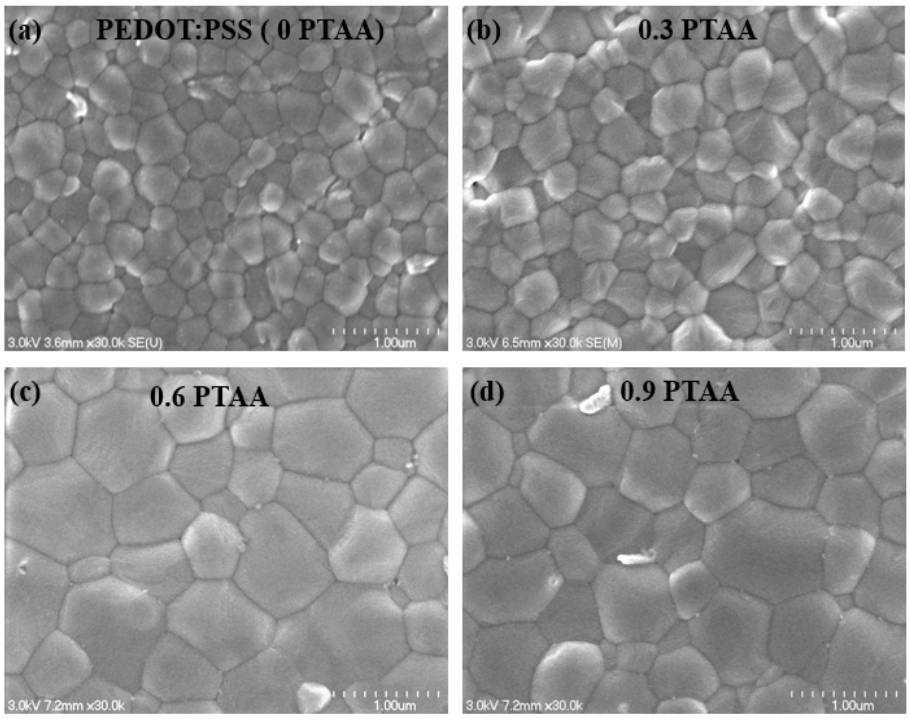

Figure 4.6. SEM micrograph of perovskite films on (a) Reference HSL. (b) 0.3 PTAA, (c) 0.6 PTAA and (d) 0.9 PTAA.

We further quantitatively compared the perovskite grain sizes of reference and 0.6 PTAA films (figure 4.7). The Image J software was used to measure the size of the grains in each perovskite film. The average grain size for the reference sample was found to be 302 ± 128 nm. The average grain size for 0.6 PTAA samples was significantly increased to 716 ± 185 nm. We anticipated that such a substantial enhancement on perovskite grain size would support increasing the solar cell open-circuit voltage (V_{OC}).

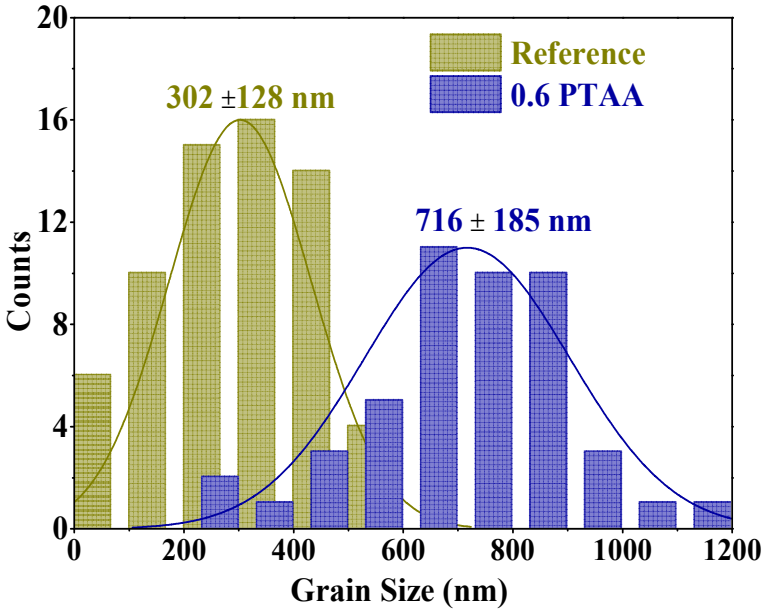

Figure 4.7. Grain size comparison histograms for reference and 0.6 PTAA samples.

Estimation of an Urbach energy can provide information on the optoelectronic quality of a semiconductor. The width of the tail of the absorbance curve estimates localized defect states in the bandgap. When the semiconductor such as perovskite is illuminated, such defect states prevent the direct transition of the charge carrier to the conduction band [59]. The Urbach energy is calculated below the optical bandgap by linear fitting ln (α) versus hγ profile using the relation $\alpha = \alpha_0 \, Exp\,(E/E_u)$, where α is the absorption

coefficient, E (=hγ) is the photon energy, and Eu is the Urbach energy.

As shown in figure 4.8, Eu's values for perovskite film with reference HSL and 0.6 PTAA HSL were found to be 83 and 68 meV, respectively. The observed reduction in the Urbach energy for perovskite film with 0.6 PTAA indicates the reduced density of trap sites due to possible passivation with PTAA modification of HTL

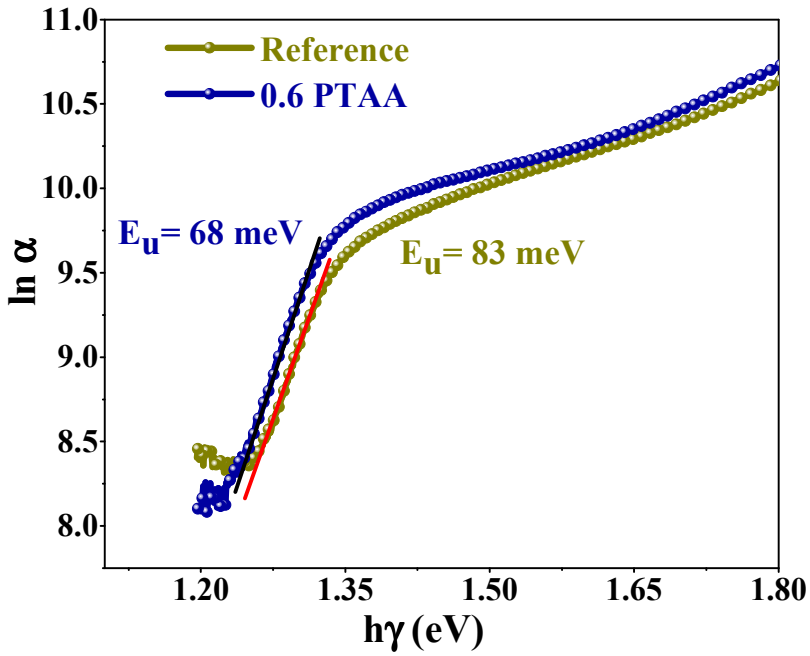

Figure 4.8. Estimation of Urbach energies for the perovskite films with reference HSL and 0.6 PTAA HSL.

4.2.3 Possible grain growth mechanism

Since perovskite grains are considerably larger with PTAA modified HTL, it is essential to understand such significant grain size improvement. Figure 4.9 shows the typical grain growth mechanism in hydrophilic vs. hydrophobic surfaces.

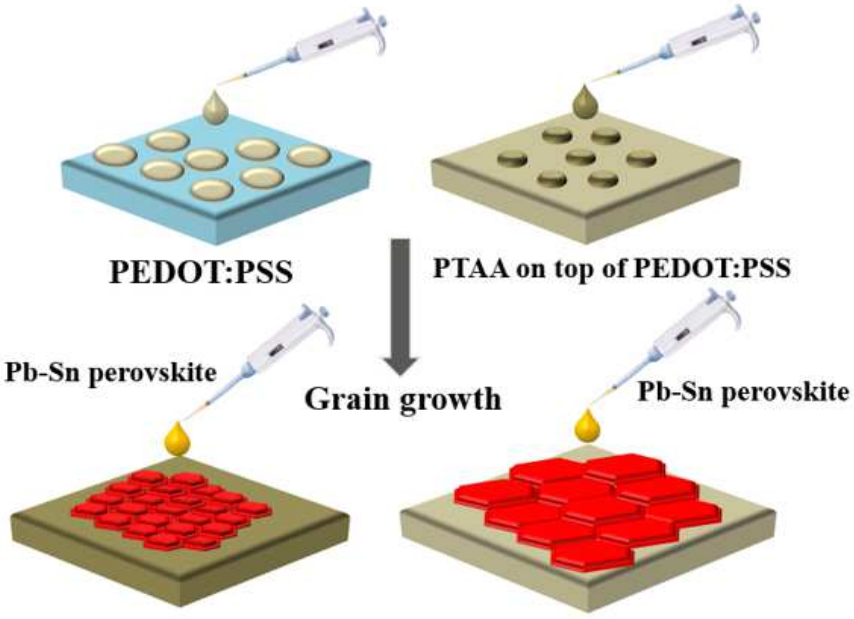

Figure 4.9. Possible grain growth mechanism in perovskite films using reference HTL and PTAA HTL.

Typically, in the hydrophilic surface, the number of nuclei is higher than that of the non-wetting surface because of the rapid heterojunction nucleation, which results in small grain size. In addition, the high surface tension dragging force in the wetting surface, such as PEDOT:PSS substrates, reduces the grain boundary mobility, limiting the grains to be merged and become bigger [108]. In contrast, with non-wetting smooth surfaces such as PEDOT/PTAA, the higher grain boundary mobility is possible because of the low surface tension dragging force on the substrate favoring the suppression of nucleation in small cavities to grow bigger grains [109].

To further study the wettability of the reference HTL and 0.6 PTAA HTL, we conducted water contact angle measurements of corresponding films. As shown in figure 4.10 (a-b), the angle was calculated as 11° for the reference film, whereas the 0.6 PTAA showed a higher contact angle of 41°. This confirms the non-wettability of the former as compared to the reference HTL film.

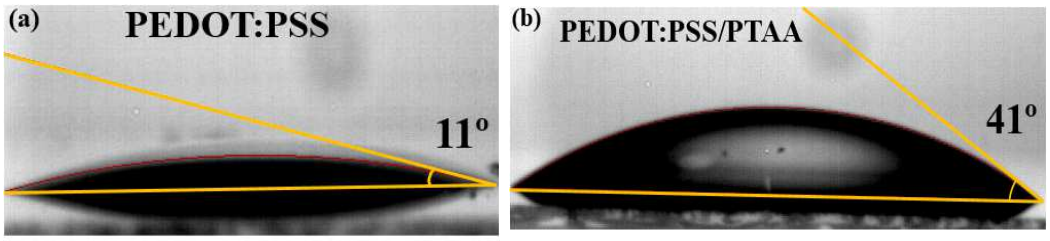

Figure 4.10. Water contact angle measurement of reference (PEDOT:PSS) HTL and 0.6 PTAA HTL.

4.2.4 Performance study of perovskite solar cells

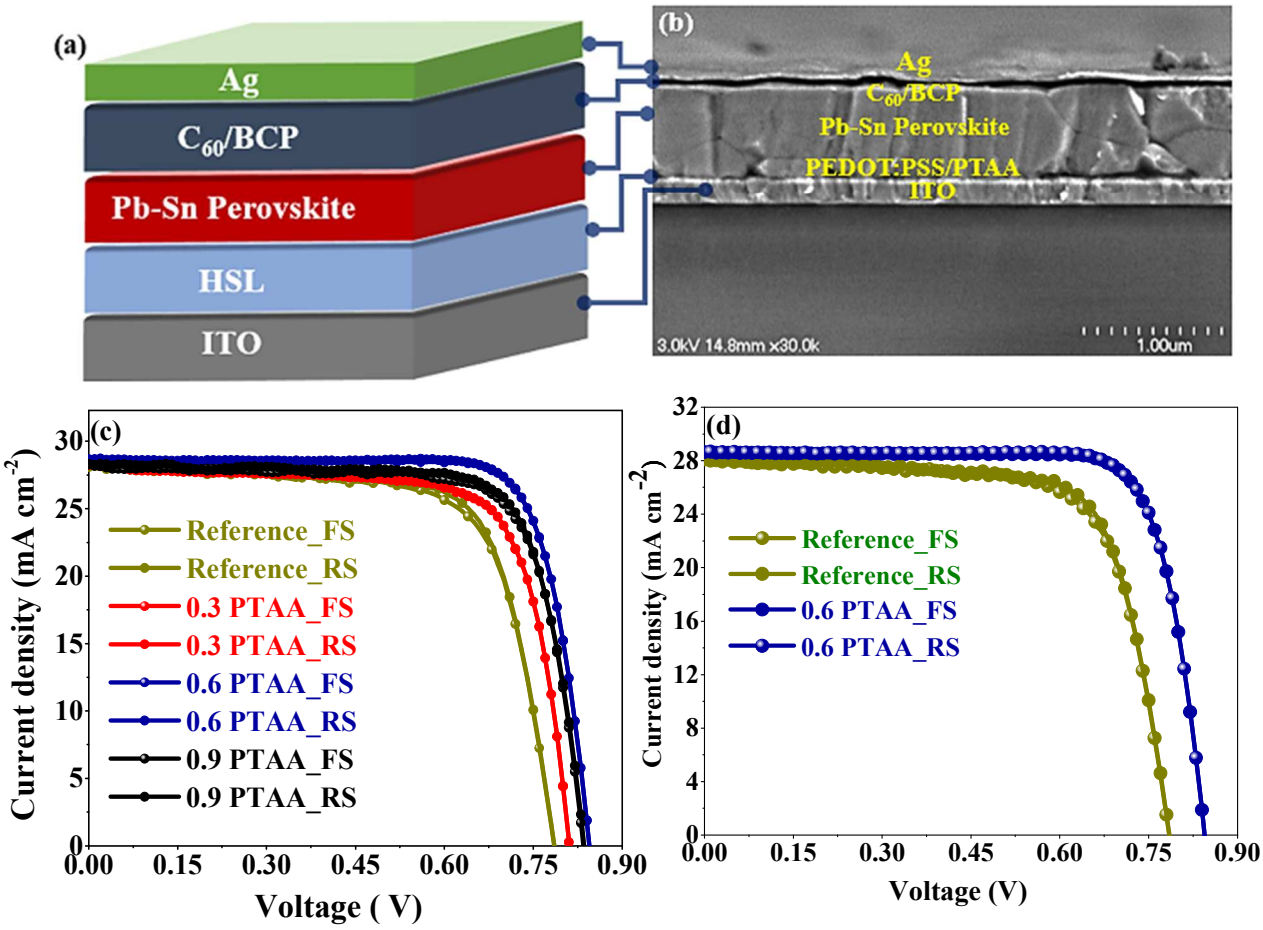

Figure 4.11. (a) Typical device structure of a p-i-n LBG PSCs. (b) SEM cross-section image of 0.6 PTAA used PSC (c)) J-V curves for reference device and devices with various

concentration of PTAA on PEDOT:PSS film as HSL. (d) J-V curves of reference and 0.6 PTAA PSCs.

Table 4.1. The photovoltaic parameters of reference device and devices with various concentration of PTAA on PEDOT:PSS film as HSL

Device	Scan	J_{sc} (mA cm^{-2})	V_{oc} (V)	FF (%)	PCE (%)	HI (%)
Reference	Forward	28.05	0.78	71.16	15.56	1.2
	Reverse	28.07	0.79	72.29	16.04	
0.3 PTAA	Forward	28.25	0.81	73.73	16.87	0.35
	Reverse	28.28	0.81	73.91	16.93	
0.6 PTAA	Forward	28.64	0.85	79.59	19.37	0.20
	Reverse	28.67	0.85	79.65	19.41	
0.9 PTAA	Forward	28.31	0.83	76.02	17.86	0.99
	Reverse	28.27	0.84	75.98	18.04	

To validate the perovskite film quality improvements with PTAA modified HSL, we fabricated complete solar cells based on the device structure shown in figure 4.11(a). The corresponding cross-sectional SEM image is presented in figure 4.11 (b). The perovskite thickness was found to be ~ 700 nm. Figure 4.11 (c) depicts J-V curves for reference devices and devices with various concentrations of PTAA on PEDOT: PSS film as HSL. Table 4.1 summarizes corresponding PV parameters for the device with each condition. As shown in figure 4.11 (d), the best PCE of 16.04 % was obtained for the reference device in reverse scan exhibiting short current density (J_{SC}) of 28.07 mA cm^{-2}, open-circuit voltage (V_{OC}) of 0.79 V and fill factor (FF) of 72.29%. 0.3 PTAA device exhibits the best PCE of 16.93 % in reverse scan with slightly increased V_{OC} of 0.81 V, FF of 73.91%, and J_{SC} of

28.64 mAcm^{-2}. 0.6 PTAA device exhibits superior performance with best PCE of 19.41 % in reverse scan with significantly increased V_{OC} of 0.85 V, FF of 79.65%, and J_{SC} of 28.67 mA cm $^{-2}$. V_{OC} loss of such a device is only ~400 mV. This achieved V_{OC}-loss is among the least V_{OC} loss reported with a similar bandgap (1.2-1.27 eV). 0.9 PTAA PSCs showed better performance than reference, 0.3 PTAA PSCs with PCE of 18.04 % in reverse scan with a decent V_{OC} of 0.84 V, FF of 75.98%, and J_{SC} of 28.27 mA cm $^{-2}$. V_{OC} obtained with 0.9 PTAA is reasonable because of the bigger grain size than perovskite films with reference and 0.3 PTAA HTLs. The 0.6 PTAA PSCs also demonstrated a much lower hysteresis index of 0.20% than the reference with 2.18%.

Figure 4.12 (a) shows the stable power output profiles for PSCs with reference and 0.6 PTAA. 0.6 PTAA PSCs delivered a stable power output of 19.38%, outperforming the reference PSCs with 15.81% for 500 sec. Figure 4.12 (b) shows the PCE histogram of 35 devices for each of the conditions. 0.6 PTAA devices showed the best average PCE of 19.03±0.3 %, whereas the reference devices showed only 15.69±0.4.

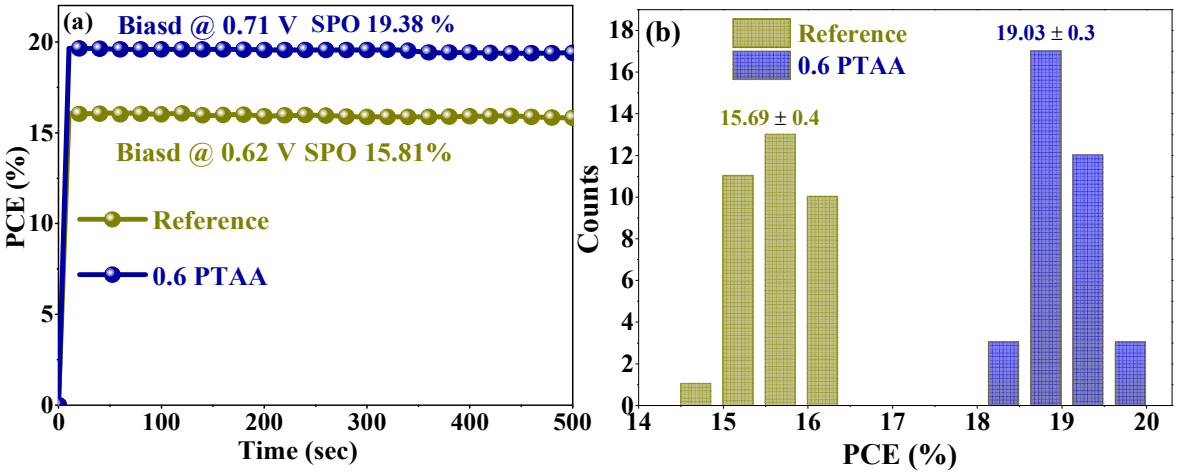

Figure 4.12. (a) Stable power outputs for reference and 0.6 PTAA PSCs, and (b) PCE histogram of reference and 0.6 PTAA PSCs.

The device statistics are illustrated in box charts shown in figure 4.13 (a-d). Each performance parameter for 0.6 PTAA PSCs was found to be greater than that of other devices. 35 devices of each condition were used to plot the box charts for different PV parameters.

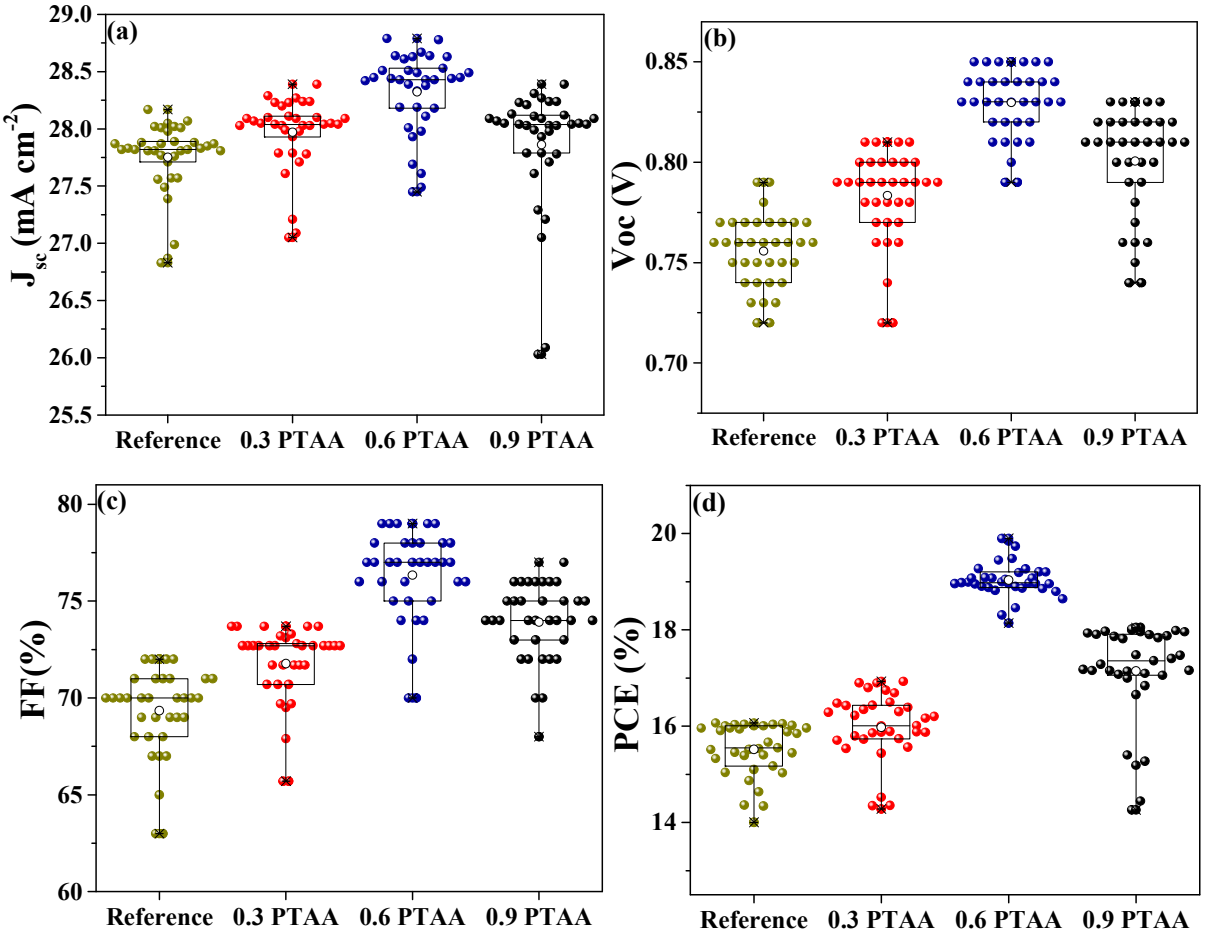

Figure 4.13 (a-d). Box charts showing device statistics for PV parameters of reference device and devices with various concentration of PTAA on PEDOT: PSS film as HSL.

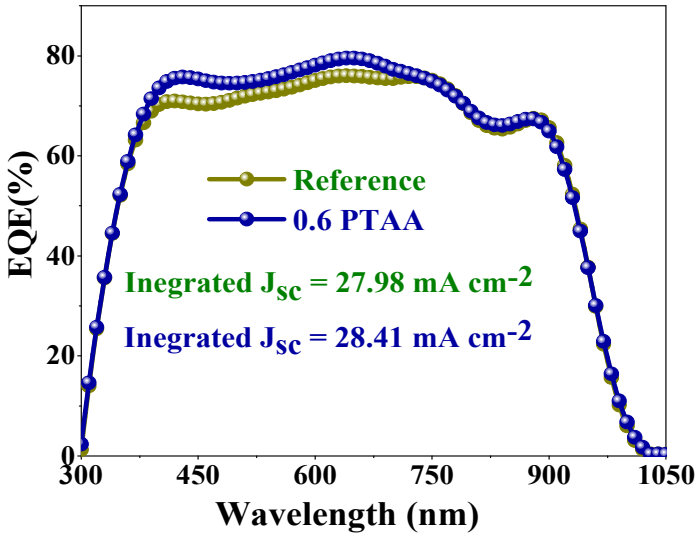

Figure 4.14. EQE profiles of reference and 0.6 PTAA PSCs

External quantum efficiency (EQE) profiles of reference and 0.6 PTAA PSCs are depicted in figure 4.14. The integrated J_{SC} obtained from the EQE curves for the reference and 0.6 PTAA PSCs were well-matched with the J_{SC} extracted from the J-V curves.

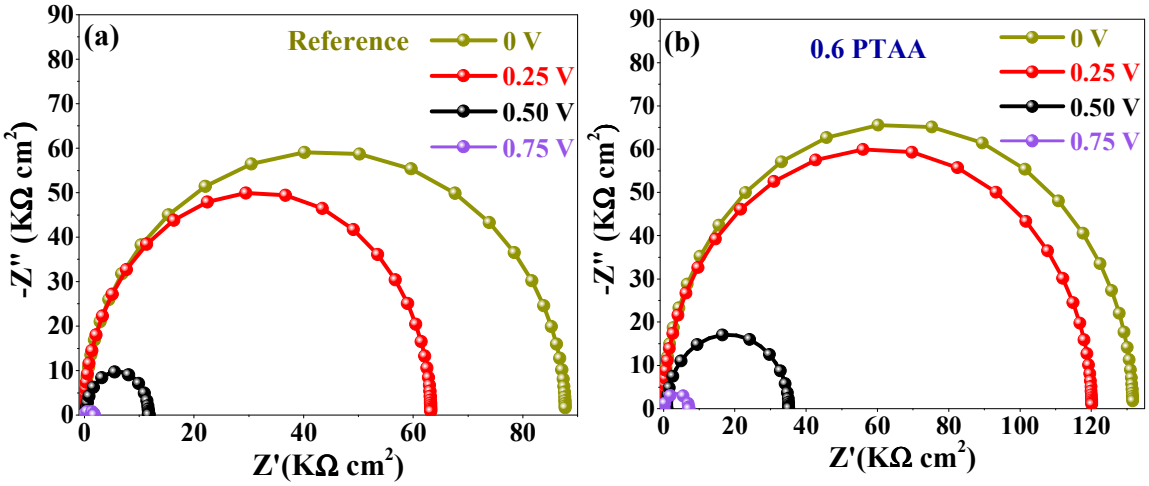

Figure 4.15. (a-b) Nyquist plots at different bias voltages for reference and 0.6 PTAA PSCs respectively.

Electrochemical impedance spectroscopy (EIS) is a convenient and extensively used tool to study the charge transfer dynamics through the perovskite solar cells' interfaces. The reference and 0.6 PTAA PSCs charge transfer dynamics were studied by measuring impedances at the frequency range of 1 Hz-1 MHz at dark conditions. Figure 4.15(a-b) shows Nyquist plots for both reference and 0.6 PTAA PSCs with different bias voltages, respectively. The obtained results were fitted with commonly used one R-C circuit to extract charge recombination resistance (R_{rec}) of PSCs interface [19, 75, 103-105]. The higher value of R_{rec} indicates a low recombination rate which is the trend observed for 0.6 PTAA devices. Every value of R_{rec} was higher in the case of 0.6 PTAA devices with every biasing voltage.

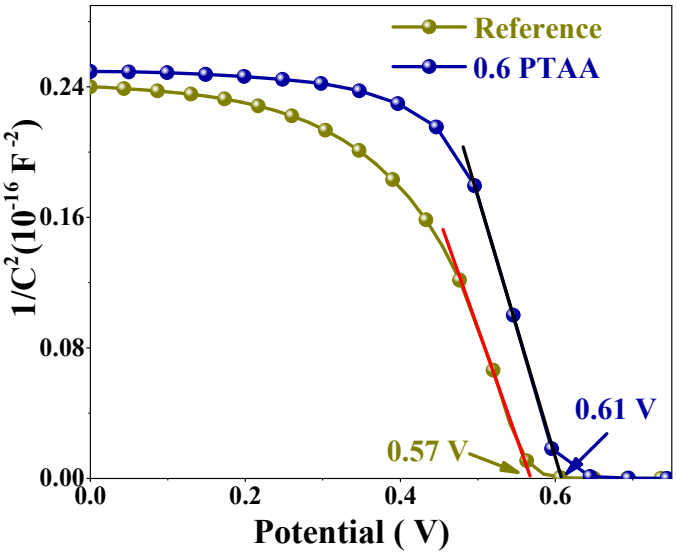

Figure 4.16. Mott-Schottky profiles of reference and 0.6 PTAA PSCs.

We also performed capacitance-voltage (C–V) measurements to elucidate further the possible mechanism responsible for enhancing PV parameters. As shown in Mott-

Schottky profiles in figure 4.16, the 0.6 PTAA device showed a higher built-in potential (Vbi) ~ 0.61 V compared to reference with ~ 0.57 V. The higher Vbi indicates the presence of a stronger electric field facilitating better charge transport through the interfaces [37, 97-100]. This is the primary reason behind the substantial enhancement in Voc from 0.79 V for control to 0.85 V for the 0.6 PTAA devices. The results from both the EIS study and M-S measurement are in line with the assumption that deposition of a tiny layer of PTAA over the PEDOT: PSS layer improves the quality of the perovskite/ HSL junction. These are concrete evidence of enhanced charge transportation in PTAA modified devices as compared to the reference device.

We further quantitatively calculated the trap densities in reference and 0.6 PTAA PSCs by recording the dark *J-V* curves of hole-only devices. Figure 4.17 (a-b) shows that there are three distinct regions and can be defined by $J \propto V^n$ relation, with n=1 being the ohmic region, n=2 is the SCLC region or the child region. The third region (n>3) is called the trap-filled region (TFL), which lies in between the ohmic and child region, where current increases quickly and non-linearly with a slight increase in bias voltage specifying that traps are continuously filled up with the charges [83]. The kink point is called trap-filled-limit-voltage (V_{TFL}) and is used to calculate the trap density (Ntrap) using the equation below [84].

$$N_{trap} = \frac{2\varepsilon_0 \varepsilon_r V_{TFL}}{eL^2} \tag{4.3}$$

Where ε_0 and ε_r are free space vacuum permittivity and relative dielectric constant of the active layer, respectively; L is the thickness of perovskite film, and e is the elementary charge. The hole trap density for reference PSC was calculated to be 7.88×10^{-15} cm^{-3} which

significantly reduced to 5.03 $\times 10^{-15}$ cm^{-3} for 0.6 PTAA PSC, indicating the role of PTAA in defect suppression as well, and this understanding is consistent with Mott Schottky analysis where enhancement on V_{bi} validated better charge transportation through the HSL/ perovskite junction.

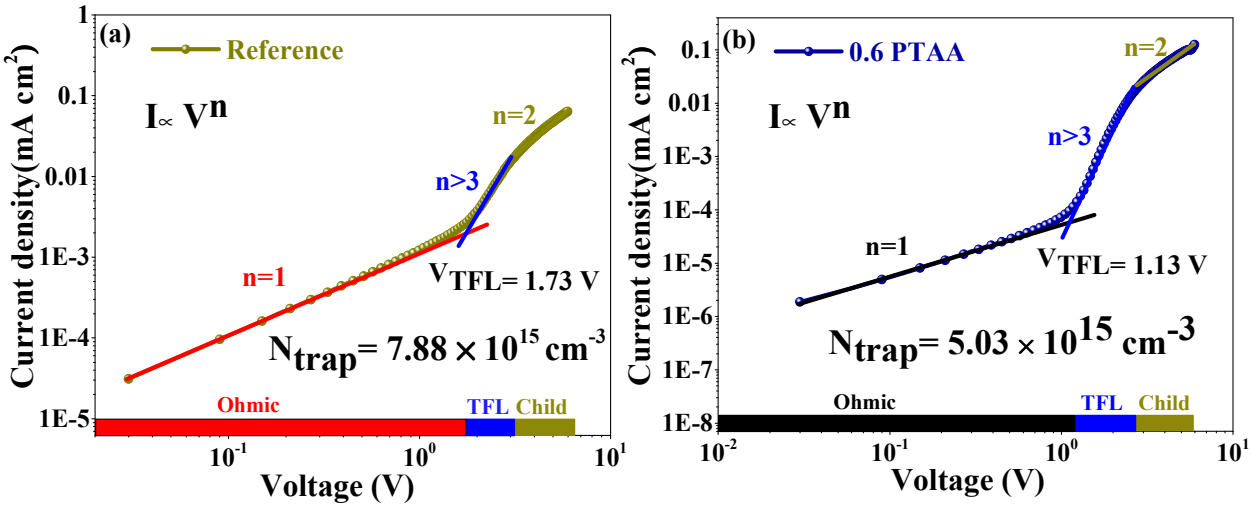

Figure 4.17. (a-b) Space charge limited current (SCLC) profiles for hole only devices for reference and 0.6 PTAA samples respectively.

We further conducted the transient photovoltage (TPV) and photocurrent (TPC) experiments to get insight into the PSCs charge carrier dynamics. Figure 4.18 (a) shows the transient photo-voltage decay profiles of the reference and 0.6 PTAA devices. As shown in the TPV decay profile**,** slow decay indicates the longer charge carrier lifetime (0.6 PTAA sample), and fast decay represents the shorter carrier lifetime (reference device). The fast decay in the TPC profile in figure 4.18 (b) indicates better charge transport with 0.6 PTAA PSC and slower decay with reference PSCs. Both longer recombination lifetime and shorter transport time are beneficial from a device perspective because charges can be collected to

the electrodes before recombining. Enhancement in a lifetime for 0.6 PTAA is ascribed to the improvement on charge extraction and interfacial defect passivation ability of the PTAA layer.

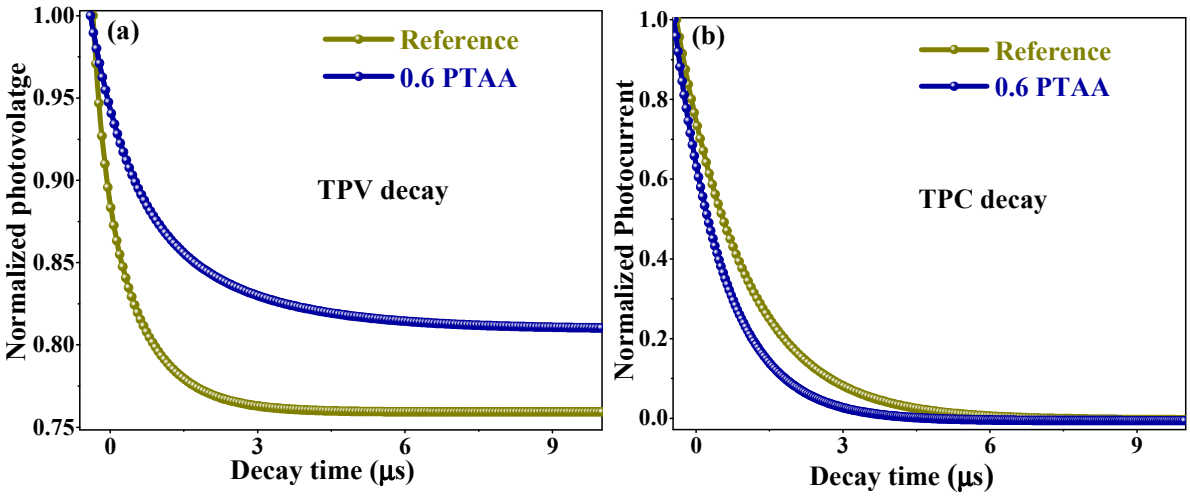

Figure 4.18. (a) TPV decay curves of reference and 0.6 PTAA PSCs. (b) TPC decay curves of reference and 0.6 PTAA PSCs

We further performed light intensity dependence V_{OC}, J_{SC}, and FF tests to help shed light on the charge recombination process. The relationship between V_{OC} and light intensity (I) is given by,

$$V_{OC} = \frac{nKT}{q} \ln\left(\frac{I}{I_0}\right) \tag{4.4}$$

Where q is the elementary charge, n is the ideality factor, K is the Boltzmann constant, and T is the temperature. The value of the slope of V_{OC} versus ln (I) profile is used to estimate the diode ideality factor and indicate the recombination mechanics dominating the device during the operation. The value of slope KT/q away from the unity indicates the dominance of trap-assisted monomolecular Shockley–Read–Hall (SRH) recombination, and the

slope's value closer to the unity indicates the dominance of bimolecular recombination phenomena in the device. As shown in figure 4.19 (a)**,** 0.6 PTAA PSCs showed a lower value of ideality factor (1.26) than that of the control (1.68), indicating the dominance of bimolecular recombination in the 0.6 PTAA devices whereas trap-assisted recombination in the reference devices. Furthermore, light dependent J_{SC} profiles the in figure 4.19 (b) device showed a higher slope of 0.97 for 0.6 PTAA than the reference device with 0.92, indicating the better charge extraction and transportation with PTAA modification. Figure 4.19 (c) shows the light dependence FF test. The FF value is expected to be almost constant throughout the illumination intensities if the recombination mechanism in a solar cell is dominated by bimolecular recombination. In the presence of traps and recombination centers, FF will not be constant throughout the illumination because more photo-generated charges will be needed to fill-up the traps [87-90]. In the case of the 0.6 PTAA HTL devices, the value of FF decreased initially up to 20 $mWcm^{-2}$. However, it remained constant throughout the rest of the illumination intensities specifying the reduced extent of trap-assisted recombination in those devices. On the other hand, FF continuously decreased with increasing the light intensity throughout the full range of illumination intensities in reference devices, suggesting traps and recombination centers in the reference device.

Figure 4.19 (d) shows the dark J-V curves of reference and 0.6 PTAA PSCs. The reference device has a reverse saturation current density of 1.04×10^{-11} mA cm^{-2}, which significantly decreased to 6.51×10^{-14} $mAcm^{-2}$ for a 0.6 PTAA device, indicating a reduced number of traps and efficient charge transportation on PTAA modified PSCs. The reduction in leakage current is understandable from the fact that 0.6 PTAA HTL instigated the larger perovskite

grains and fewer grain boundaries, as evidenced by SEM images. We also estimated the values of series and shunt resistances in the reference and 0.6 PTAA PSCs and are presented in table 4.2. Reduction in series resistance (R_s) for 0.6 PTAA film to 4.13 from 8.97 Ω for reference film is apparent because of the improved film conductivity and mobility, as discussed earlier. The value of shunt resistance R_{Sh} for 0.6 PTAA PSC was estimated to be 288.23 KΩ which is much higher than that of reference PSCs with 163.54 KΩ. Substantial enhancement on R_{Sh} is reasonable and is correlated to significant improvement on V_{OC} and FF of 0.6 PTAA PSCs.

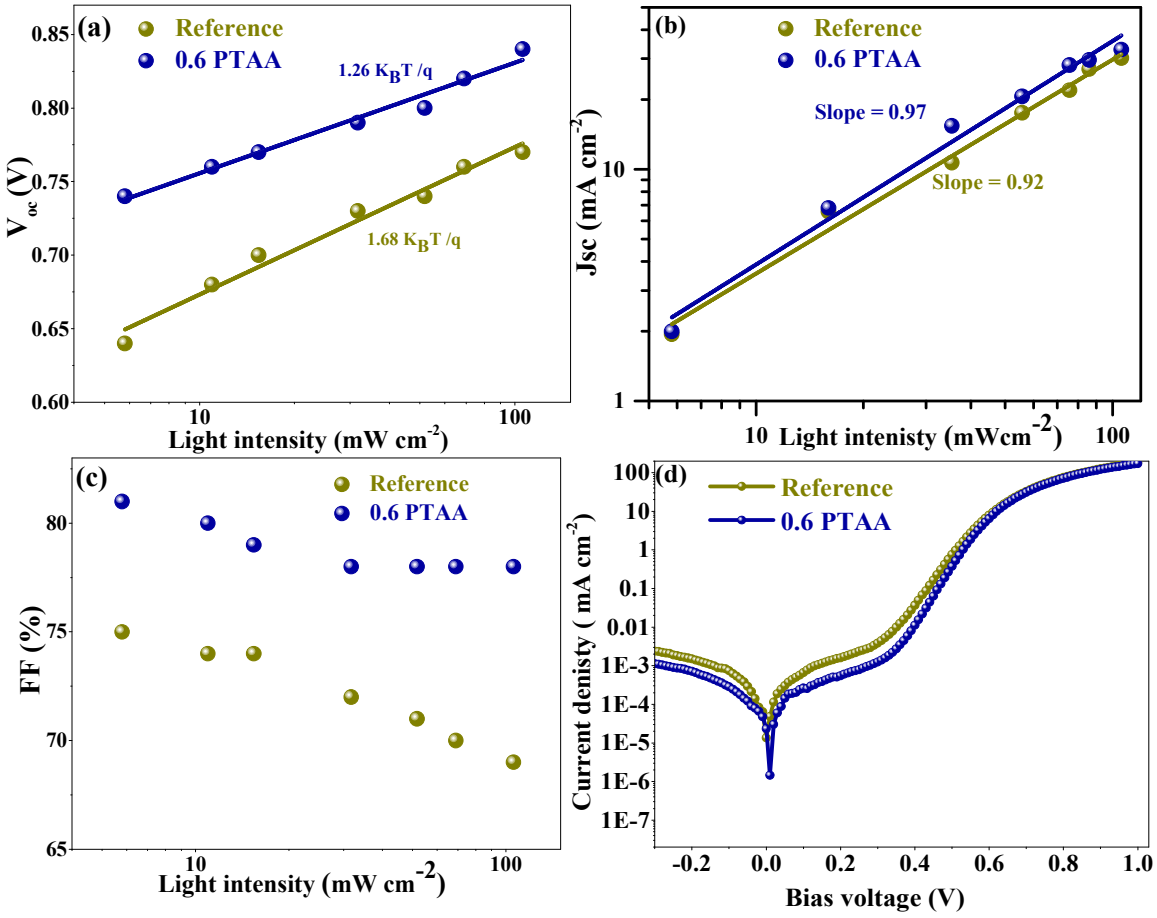

Figure 4.19. Light dependence of (a) V_{OC}, (b) J_{SC}, (c) FF of reference and 0.6 PTAA PSCs. (d) Dark J-V curves of reference and 0.6 PTAA PSCs.

Table 4.2. Extracted reverse saturation current density, series, and shunt resistances from the dark J-V curves of reference and 0.6 PTAA PSCs.

Device	J_0 (mA cm^{-2})	R_s (Ω)	R_{sh} (KΩ)
Reference	1.04×10^{-11}	8.97	163.54
0.6 PTAA	6.51×10^{-14}	4.13	288.23

4.2.5 Stability analysis of perovskite solar cells

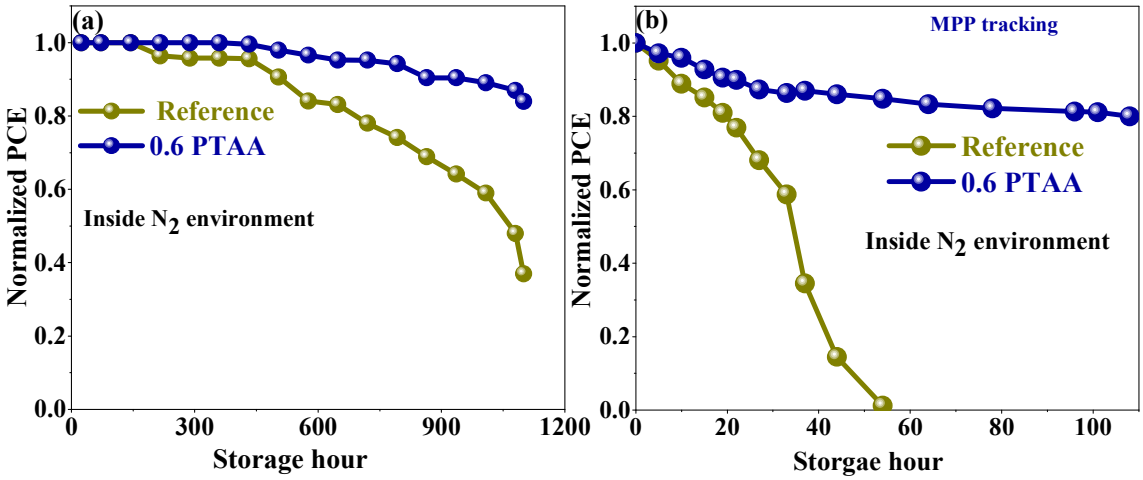

Figure 4.20. (a) PCE evolution of reference and 0.6 PTAA PSCs in Glovebox over the time (b) Operational stability of reference and 0.6 PTAA PSCs at MPP inside glovebox over the time under continuous 1.5 AM light illumination.

The stability of the unencapsulated devices was evaluated by tracking the evolution of PCE over time while storing the devices in inert (N_2 filled glovebox) conditions. As shown in figure 4.20 (a), an excellent PCE retention of ~ 83 % was obtained for the 0.6 PTAA devices, whereas the reference device retained only 35 % of its initial PCE over the

storage time of 1100 hours. Figure 4.20 (b) shows maximum power point (MPP) tracking of unencapsulated reference and 0.6 PTAA devices under continuous light inside N_2 filled GB. The reference device died entirely after 54 hours, but 0.6 PTAA PSC device ran up to 108 hours with a decent PCE retention of 80%. The reduction in PCE of reference PSCs is ascribed to degradation of perovskite film under continuous illumination, indicating inferior photophysical properties of the reference sample to that of 0.6 PTAA sample.

To study the effect of HTL modification with PTAA on photophysical properties of perovskite films, we continuously illuminated the reference perovskite sample and 0.6 PTAA sample by recording the absorption spectra and XRD patterns for both films. Figure 4.21 (a) shows the absorption spectrum of reference perovskite film degraded over the illumination span of 54 hours. Digital photographs in the inset showed the physical degradation of the film. In contrast, the absorption spectrum of 0.6 PTAA perovskite film remained almost the same as fresh throughout the illumination period of 54 h (figure 4.21 b). Thus, digital photographs of perovskite films in the inset did not show significant physical degradation. This observation is in good agreement with the XRD pattern recorded for both fresh and 54 h illuminated samples for each condition. As depicted in figure 4.21 (c), the intensity of the PbI_2/ SnI_2 complex is prominent in the case of reference perovskite film after the illumination of 54 h, which is ascribed to the decomposition of perovskite into lead and tin species, indicating the intrinsic instability of the reference perovskite film. On the contrary, PTAA modified perovskite sample did not show the significant decomposition of perovskite into lead and tin complex. Also, the intensity of perovskite characteristics peaks at 14.09° and 28.2° are higher than that of reference perovskite film. These results demonstrate the superior operational stability of PTAA modified PSCs over

the reference PSCs. The improvements on both the dark shelf and operational stability of PTAA modified PSCs can be credited to superior perovskite film morphology obtained with large grains with minimal grain boundaries, improved crystallinity, minimized interfacial defects, and superior charge transport dynamics.

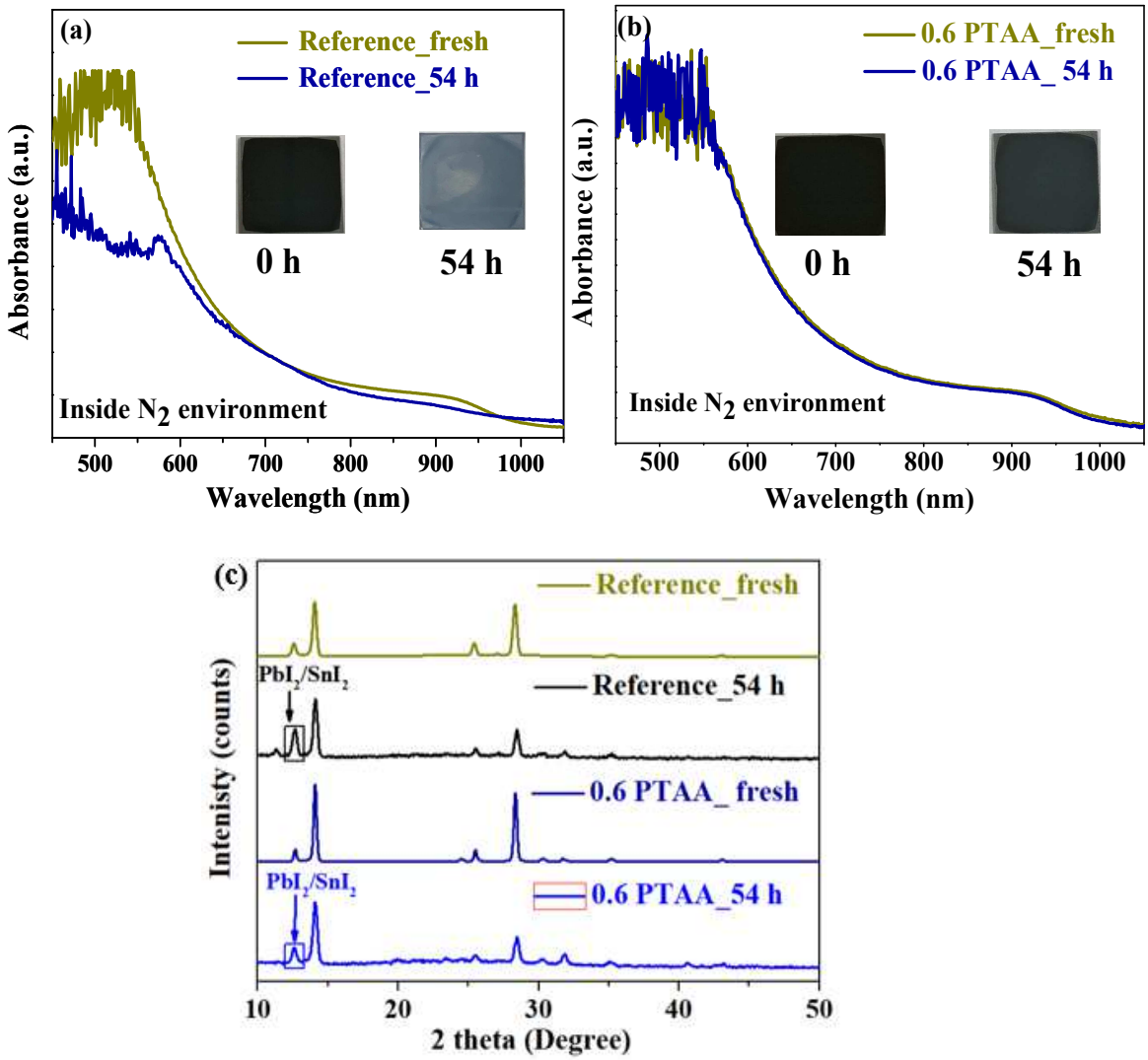

Figure 4.21. (a-b) Absorption spectra of fresh and 54 h illuminated perovskite films for reference and 0.6 PTAA samples respectively (Insets: digital photographs of corresponding films), (c) XRD patterns of fresh and 54 illuminated perovskite films with reference and 0.6 PTAA HTL.

4.3 Conclusion

In summary, the Pb-Sn mixed low-bandgap perovskite films with superior morphology, excellent optoelectronic properties with large grains, few grain boundaries, high crystallinity, and reduced trap density were achieved with a simple modification of HSL with PTAA. The improvements were reflected on PV metrics of fabricated PSCs where champion PCE of 19.41% was achieved with improved J_{SC}, high FF of ~80%, and high open-circuit voltage of 0.85 V. The V_{OC}-loss of 0.4 V attained herein corresponds to one of the least V_{OC}-loss among similar Pb–Sn mixed low-bandgap perovskites. Furthermore, the PTAA modified HSL PSCs dark-self and operational stabilities significantly elongated because of improved HSL/ perovskite interface quality. This study provides a simple but powerful method to obtain high-quality Pb–Sn mixed low-bandgap perovskite films with higher V_{OC}, FF, PCE, and stability. Moreover, this strategy can be easily adapted to improve the performance of other perovskite compositions as well.

CHAPTER 5 CONCLUSIONS AND FUTURE WORKS

5.1 Conclusions

Pb-Sn mixed perovskites have several critical issues which hamper the quality of the perovskite absorber layer. To [27] solve a few of them, we have successfully employed several strategies. We also performed several films and device-level characterizations to study and examine the behavior and performance of PSCs. The significant findings of the dissertation are as follows.

- Oxidation of Sn^{+2} to more stable Sn^{+4} restricts the Pb-Sn-based PSCs to achieve higher efficiency and stability. In addition, a trace amount of PEAI incorporation (1.5 mg per mL of perovskite solution) to the perovskite precursor solution can inhibit the rapid oxidation of Sn^{+2} also controls the perovskite crystallization process.
- Unwanted photo-inactive particles can compromise the PV performance of PSCs. Such particles (Pb_2/SnI_2) on perovskite surface causes inhomogeneous crystallization forming rough and non-compact surface. Removal of such particles can help grow compact pinhole hole free, smooth perovskite surface.
- Defect passivation at the perovskite film surface resulted in a smooth, compact film with high crystallinity and lower electronic disorder by passivating both positively and negatively charged defects. A possible defect passivation mechanism was also described in detail. The evidence of co-ordination of Sn^{+2} and Pb^{+2} with lone pair of a free electron in PEA^{+} was also explained briefly with the help of Raman Spectroscopy.

- The PSCs fabricated using PEAI as an additive resulted in very high V_{OC} of 0.85 V (Average 0.83±0.01) and PCE of 17.33 % (Average 16.98±0.3). On the contrary, the control PSCs without PEAI could only get the best V_{OC} of 0.76 V (Average 0.73±0.02) and PCE of 14.61 % (Average 13.84 ± 0.7). The V_{OC} of 0.85 V is among the best values obtained so far for similar bandgap Pb-Sn PSCs and corresponds to a V_{OC} loss of only 0.4 V.
- The ambient and dark self-stabilities of the PEAI-treated devices are significantly enhanced. The improved crystallinity pinhole hole-free compact perovskite film morphology and hydrophobicity of PEAI-doped perovskite films might have a combined effect on the improved stability of 1.5 PEAI perovskite solar cells.
- In our second project, we explored using an ultrathin layer of P-type semiconductor PTAA over the commonly used hole selective layer (HSL) of PEDOT:PSS to tune the conductivity of the HTL layer and to improve the charge transport properties of perovskite / HTL junction.
- PEDOT:PSS /PTAA, when used as HTL, resulted in high film conductivity and mobility as evidenced with CS-AFM and SCLC measurements. Moreover, perovskite grain size also significantly enlarged, benefiting from the hydrophobic nature of PTAA. The trap density in the perovskite surface was also significantly reduced. The perovskite grain growth mechanism in both PEDOT:PSS and PEDOT:PSS/PTAA layers was also proposed and explained.
- The PSCs fabricated using PEDOT:PSS/PTAA as HTL resulted in very high V_{OC} of 0.85 V (Average 0.83±0.02) and PCE of 19.41 % (Average 19.03±0.3). The reference PSC on PEDOT:PSS could only get the best V_{OC} of 0.79 V (Average

0.76±0.02) and PCE of 16.04 % (Average 15.69±0.40). The V_{OC} of 0.85 V is among the best values obtained so far for similar bandgap Pb-Sn PSCs and corresponds to a V_{OC} loss of only 0.4 V.

- A tiny layer of hydrophobic PTAA can protect the underlying layer of acidic PEDOT:PSS from oxygen and moisture. This fact was reflected in the enhancement of the PSCs operational and dark-shelf stabilities with PEDOT:PSS/PTAA.

5.2 Future work

Numerous future works can be done to improve the perovskite composition, structure to achieve higher performance which can be the extension of this dissertation. Some of the potential future works are listed below.

- The bandgap of the low bandgap 'rear' cell depends on the 'top' cell's bandgap in tandem structure, and it can be changed just by changing the Pb and Sn percentage. In our work for 1.25 eV, we have used 50% Sn and 50% Pb. If required, increasing the Sn percentage can lower the bandgap. Nevertheless, the proper anti-oxidation agent should be added to the perovskite solution to compensate for the Sn^{+2} oxidation.

- In our first project, we witnessed that a trace amount of PEAI addition to perovskite solution can inhibit the rapid crystallization of Pb-Sn-based perovskite films simultaneously passivating both positively and negatively charged defects. Therefore, finding a suitable additive is necessary to control the Sn oxidation. In this regard, the use of different antioxidant with different functional groups can be studied.

- Exploration of different characterization techniques would be helpful to examine further the perovskite crystal structure, composition, and effect using the PEAI into perovskite. Since XRD did not show any 2D peaks but using XPS and TEM, further information about 2D/3D heterostructure formation can be obtained.

- In our second project, we used PEDOT: PSS and PEDOT:PSS/PTAA as the hole transport layer. PEDOT:PSS is acidic and has low conductivity. PEDOT:PSS can be wholly replaced with other suitable HTLs. PTAA can be doped with a suitable dopant to increase conductivity and mobility further. In addition, different robust HTLs can be explored to get better stability and performance.

References

[1] J. Banerjee, K. Dutta, and D. Rana, "Carbon nanomaterials in renewable energy production and storage applications," in *Emerging nanostructured materials for energy and environmental science*: Springer, 2019, pp. 51-104.

[2] I. Dincer, "Environmental impacts of energy," *Energy policy,* vol. 27, no. 14, pp. 845-854, 1999.

[3] J. Peng, L. Lu, and H. Yang, "Review on life cycle assessment of energy payback and greenhouse gas emission of solar photovoltaic systems," *Renew. Sustain. Energy. Rev.,* vol. 19, pp. 255-274, 2013.

[4] P. A. Owusu and S. Asumadu-Sarkodie, "A review of renewable energy sources, sustainability issues and climate change mitigation," *Cogent Engineering,* vol. 3, no. 1, p. 1167990, 2016.

[5] W. Palz, *Power for the world: the emergence of electricity from the Sun*. Pan Stanford Publishing, 2010.

[6] H. Zou *et al.*, "Alternating Current Photovoltaic Effect," *Adv. Mater.,* vol. 32, no. 11, p. 1907249, 2020.

[7] M. A. Green, A. Ho-Baillie, and H. J. Snaith, "The emergence of perovskite solar cells," *Nature Photonics,* Review Article vol. 8, p. 506, 06/27/online 2014, doi: 10.1038/nphoton.2014.134.

[8] M. Liu, M. B. Johnston, and H. J. Snaith, "Efficient planar heterojunction perovskite solar cells by vapour deposition," *Nature,* vol. 501, no. 7467, pp. 395-398, 2013.

[9] M. Saliba *et al.*, "How to Make over 20% Efficient Perovskite Solar Cells in Regular (n–i–p) and Inverted (p–i–n) Architectures," *Chemistry of Materials,* vol. 30, no. 13, pp. 4193-4201, 2018.

[10] S. D. Stranks *et al.*, "Electron-hole diffusion lengths exceeding 1 micrometer in an organometal trihalide perovskite absorber," *Science,* vol. 342, no. 6156, pp. 341-344, 2013.

[11] H. Chen *et al.*, "A solvent-and vacuum-free route to large-area perovskite films for efficient solar modules," *Nature,* vol. 550, no. 7674, pp. 92-95, 2017.

[12] J. Ávila *et al.*, "High voltage vacuum-deposited CH 3 NH 3 PbI 3–CH 3 NH 3 PbI 3 tandem solar cells," *Energy & Environmental Science,* vol. 11, no. 11, pp. 3292-3297, 2018.

[13] J. Burschka *et al.*, "Sequential deposition as a route to high-performance perovskite-sensitized solar cells," *Nature,* vol. 499, no. 7458, pp. 316-319, 2013.

[14] A. Kojima, K. Teshima, Y. Shirai, and T. Miyasaka, "Organometal halide perovskites as visible-light sensitizers for photovoltaic cells," *Journal of the American Chemical Society,* vol. 131, no. 17, pp. 6050-6051, 2009.

[15] L. Protesescu *et al.*, "Nanocrystals of Cesium Lead Halide Perovskites (CsPbX3, X = Cl, Br, and I): Novel Optoelectronic Materials Showing Bright Emission with Wide Color Gamut," *Nano Lett.,* vol. 15, no. 6, pp. 3692-3696, 2015/06/10 2015, doi: 10.1021/nl5048779.

[16] K. X. Steirer *et al.*, "Defect Tolerance in Methylammonium Lead Triiodide Perovskite," *ACS Energy Letters,* vol. 1, no. 2, pp. 360-366, 2016/08/12 2016, doi: 10.1021/acsenergylett.6b00196.

[17] M. A. Green, E. D. Dunlop, J. Hohl□Ebinger, M. Yoshita, N. Kopidakis, and X. Hao, "Solar cell efficiency tables (version 56)," *Progress in Photovoltaics: Research and Applications,* vol. 28, no. 7, pp. 629-638, 2020.

[18] M. T. Hörantner *et al.*, "The potential of multijunction perovskite solar cells," *ACS Energy Letters,* vol. 2, no. 10, pp. 2506-2513, 2017.

[19] D. Yang, R. Yang, J. Zhang, Z. Yang, S. F. Liu, and C. Li, "High efficiency flexible

perovskite solar cells using superior low temperature TiO 2," *Energy & Environmental Science,* vol. 8, no. 11, pp. 3208-3214, 2015.

[20] Y. Zhao *et al.*, "A polymer scaffold for self-healing perovskite solar cells," *Nat. Commun.,* vol. 7, no. 1, p. 10228, 2016/01/06 2016, doi: 10.1038/ncomms10228.

[21] A. Rajagopal *et al.*, "Highly efficient perovskite–perovskite tandem solar cells reaching 80% of the theoretical limit in photovoltage," *Adv. Mater.,* vol. 29, no. 34, p. 1702140, 2017.

[22] M. A. Green, Y. Hishikawa, E. D. Dunlop, D. H. Levi, J. Hohl□Ebinger, and A. W. Ho□Baillie, "Solar cell efficiency tables (version 52)," *Progress in Photovoltaics: Research and Applications,* vol. 26, no. 7, pp. 427-436, 2018.

[23] J. Jeong *et al.*, "Pseudo-halide anion engineering for α-FAPbI3 perovskite solar cells," *Nature,* vol. 592, no. 7854, pp. 381-385, 2021/04/01 2021, doi: 10.1038/s41586-021-03406-5.

[24] G. Grancini, "One-year stable perovskite solar cells by 2D/3D interface engineering," *Nat. Commun.,* vol. 8, 2017// 2017.

[25] H. Queisser, "Slip Patterns on Boron□Doped Silicon Surfaces," *Journal of Applied Physics,* vol. 32, no. 9, pp. 1776-1780, 1961.

[26] H. L. Zhu and W. C. Choy, "Crystallization, Properties, and Challenges of Low□Bandgap Sn–Pb Binary Perovskites," *Solar RRL,* vol. 2, no. 10, p. 1800146, 2018.

[27] F. Hao, C. C. Stoumpos, R. P. H. Chang, and M. G. Kanatzidis, "Anomalous Band Gap Behavior in Mixed Sn and Pb Perovskites Enables Broadening of Absorption Spectrum in Solar Cells," *Journal of the American Chemical Society,* vol. 136, no. 22, pp. 8094-8099, 2014/06/04 2014, doi: 10.1021/ja5033259.

[28] R. Prasanna *et al.*, "Compositional engineering of tin-lead halide perovskites for efficient and stable low band gap solar cells," in *2018 IEEE 7th World Conference on Photovoltaic Energy Conversion (WCPEC)(A Joint Conference of 45th IEEE*

PVSC, 28th PVSEC & 34th EU PVSEC), 2018: IEEE, pp. 1718-1720.

[29] Z. Song, C. Chen, C. Li, R. A. Awni, D. Zhao, and Y. Yan, "Wide-bandgap, low-bandgap, and tandem perovskite solar cells," *Semiconductor Science and Technology,* vol. 34, no. 9, p. 093001, 2019.

[30] N. Ghimire *et al.*, "Mitigating Open-Circuit Voltage Loss in Pb–Sn Low-Bandgap Perovskite Solar Cells via Additive Engineering," *ACS Appl. Energy Mater.,* 2021/02/01 2021, doi: 10.1021/acsaem.0c02895.

[31] A. Rajagopal, P.-W. Liang, C.-C. Chueh, Z. Yang, and A. K. Y. Jen, "Defect Passivation via a Graded Fullerene Heterojunction in Low-Bandgap Pb–Sn Binary Perovskite Photovoltaics," *ACS Energy Letters,* vol. 2, no. 11, pp. 2531-2539, 2017/11/10 2017, doi: 10.1021/acsenergylett.7b00847.

[32] D. Forgács, "Efficient monolithic perovskite/perovskite tandem solar cells," *Adv. Energy Mater.,* vol. 8, 2016// 2016.

[33] S. Shao *et al.*, "Enhancing the crystallinity and perfecting the orientation of formamidinium tin iodide for highly efficient Sn-based perovskite solar cells," *Nano Energy,* vol. 60, pp. 810-816, 2019/06/01/ 2019, doi: https://doi.org/10.1016/j.nanoen.2019.04.040.

[34] W. Zhang, G. E. Eperon, and H. J. Snaith, "Metal halide perovskites for energy applications," *Nat. Energy,* Perspective vol. 1, p. 16048, 05/09/online 2016, doi: 10.1038/nenergy.2016.48.

[35] S. Gupta, D. Cahen, and G. Hodes, "How SnF2 impacts the material properties of lead-free tin perovskites," *J. Phys. Chem. C,* vol. 122, no. 25, pp. 13926-13936, 2018.

[36] X. Xu *et al.*, "Ascorbic acid as an effective antioxidant additive to enhance the efficiency and stability of Pb/Sn-based binary perovskite solar cells," *Nano Energy,* vol. 34, pp. 392-398, 2017.

[37] R. Lin *et al.*, "Monolithic all-perovskite tandem solar cells with 24.8% efficiency exploiting comproportionation to suppress Sn (II) oxidation in precursor ink," *Nature Energy,* pp. 1-10, 2019.

[38] S. Lv *et al.*, "Stability of Sn-Pb mixed organic–inorganic halide perovskite solar cells: Progress, challenges, and perspectives," *Journal of Energy Chemistry,* vol. 65, pp. 371-404, 2022/02/01/ 2022, doi: https://doi.org/10.1016/j.jechem.2021.06.011.

[39] C. Liu, "C60 additive-assisted crystallization in CH3NH3Pb0.75Sn0.25I3 perovskite solar cells with high stability and efficiency," *Nanoscale,* vol. 9, 2017// 2017.

[40] D. Chi, "Composition and interface engineering for efficient and thermally stable Pb–Sn mixed low-bandgap perovskite solar cells," *Adv. Funct. Mater.,* vol. 28, 2018// 2018.

[41] D. Zhao *et al.*, "Efficient two-terminal all-perovskite tandem solar cells enabled by high-quality low-bandgap absorber layers," *Nature Energy,* vol. 3, no. 12, pp. 1093-1100, 2018/12/01 2018, doi: 10.1038/s41560-018-0278-x.

[42] R. Prasanna *et al.*, "Design of low bandgap tin–lead halide perovskite solar cells to achieve thermal, atmospheric and operational stability," *Nature Energy,* vol. 4, no. 11, pp. 939-947, 2019/11/01 2019, doi: 10.1038/s41560-019-0471-6.

[43] A. F. Palmstrom *et al.*, "Enabling Flexible All-Perovskite Tandem Solar Cells," *Joule,* 2019.

[44] Z. Yang *et al.*, "Stable Low□Bandgap Pb–Sn Binary Perovskites for Tandem Solar Cells," *Advanced Materials,* vol. 28, no. 40, pp. 8990-8997, 2016.

[45] T. Jiang *et al.*, "Power Conversion Efficiency Enhancement of Low-Bandgap Mixed Pb–Sn Perovskite Solar Cells by Improved Interfacial Charge Transfer," *ACS Energy Letters,* vol. 4, no. 7, pp. 1784-1790, 2019.

[46] G. E. Eperon, S. D. Stranks, C. Menelaou, M. B. Johnston, L. M. Herz, and H. J. Snaith, "Formamidinium lead trihalide: a broadly tunable perovskite for efficient planar heterojunction solar cells," *Energy & Environmental Science,* 10.1039/C3EE43822H vol. 7, no. 3, pp. 982-988, 2014, doi: 10.1039/C3EE43822H.

[47] A. H. Slavney, R. W. Smaha, I. C. Smith, A. Jaffe, D. Umeyama, and H. I. Karunadasa, "Chemical Approaches to Addressing the Instability and Toxicity of Lead–Halide Perovskite Absorbers," *Inorganic Chemistry,* vol. 56, no. 1, pp. 46-55, 2017/01/03 2017, doi: 10.1021/acs.inorgchem.6b01336.

[48] D. Yao *et al.*, "2D–3D Mixed Organic–Inorganic Perovskite Layers for Solar Cells with Enhanced Efficiency and Stability Induced by n-Propylammonium Iodide Additives," *ACS Applied Materials & Interfaces,* vol. 11, no. 33, pp. 29753-29764, 2019/08/21 2019, doi: 10.1021/acsami.9b06305.

[49] W. Liao *et al.*, "Fabrication of Efficient Low-Bandgap Perovskite Solar Cells by Combining Formamidinium Tin Iodide with Methylammonium Lead Iodide," *Journal of the American Chemical Society,* vol. 138, no. 38, pp. 12360-12363, 2016/09/28 2016, doi: 10.1021/jacs.6b08337.

[50] F. Zhang *et al.*, "Growth of Amorphous Passivation Layer Using Phenethylammonium Iodide for High□Performance Inverted Perovskite Solar Cells," *Solar RRL,* 2019.

[51] X. Lian *et al.*, "Highly Efficient Sn/Pb Binary Perovskite Solar Cell via Precursor Engineering: A Two□Step Fabrication Process," *Advanced Functional Materials,* vol. 29, no. 5, p. 1807024, 2019.

[52] T. Leijtens *et al.*, "Tin–lead halide perovskites with improved thermal and air stability for efficient all-perovskite tandem solar cells," *Sustainable Energy & Fuels,* vol. 2, no. 11, pp. 2450-2459, 2018.

[53] G. E. Eperon *et al.*, "Perovskite-perovskite tandem photovoltaics with optimized

band gaps," *Science,* vol. 354, no. 6314, pp. 861-865, 2016.

[54] H. L. Zhu, J. Xiao, J. Mao, H. Zhang, Y. Zhao, and W. C. Choy, "Controllable Crystallization of CH3NH3Sn0. 25Pb0. 75I3 Perovskites for Hysteresis□Free Solar Cells with Efficiency Reaching 15.2%," *Advanced Functional Materials,* vol. 27, no. 11, p. 1605469, 2017.

[55] C. Li *et al.*, "In Situ Tin (II) Complex Antisolvent Process Featuring Simultaneous Quasi□Core–Shell Structure and Heterojunction for Improving Efficiency and Stability of Low□Bandgap Perovskite Solar Cells," *Advanced Energy Materials,* p. 1903013.

[56] J. Tong *et al.*, "Carrier lifetimes of >1 μs in Sn-Pb perovskites enable efficient all-perovskite tandem solar cells," *Science,* vol. 364, no. 6439, pp. 475-479, 2019, doi: 10.1126/science.aav7911.

[57] S. Shao *et al.*, "Enhancing the performance of the half tin and half lead perovskite solar cells by suppression of the bulk and interfacial charge recombination," *Advanced Materials,* vol. 30, no. 35, p. 1803703, 2018.

[58] R. Lin *et al.*, "Monolithic all-perovskite tandem solar cells with 24.8% efficiency exploiting comproportionation to suppress Sn(ii) oxidation in precursor ink," *Nature Energy,* vol. 4, no. 10, pp. 864-873, 2019/10/01 2019, doi: 10.1038/s41560-019-0466-3.

[59] G. Kapil *et al.*, "Strain relaxation and light management in tin–lead perovskite solar cells to achieve high efficiencies," *ACS Energy Letters,* vol. 4, no. 8, pp. 1991-1998, 2019.

[60] C. Li *et al.*, "Low-bandgap mixed tin–lead iodide perovskites with reduced methylammonium for simultaneous enhancement of solar cell efficiency and stability," *Nature Energy,* vol. 5, no. 10, pp. 768-776, 2020/10/01 2020, doi: 10.1038/s41560-020-00692-7.

[61] Z. Zhu, N. Li, D. Zhao, L. Wang, and A. K. Y. Jen, "Improved Efficiency and

Stability of Pb/Sn Binary Perovskite Solar Cells Fabricated by Galvanic Displacement Reaction," *Advanced Energy Materials,* vol. 9, no. 7, p. 1802774, 2019.

[62] D. Zhao *et al.*, "Low-bandgap mixed tin–lead iodide perovskite absorbers with long carrier lifetimes for all-perovskite tandem solar cells," *Nature Energy,* vol. 2, no. 4, p. 17018, 2017.

[63] D. Chi *et al.*, "Composition and Interface Engineering for Efficient and Thermally Stable Pb–Sn Mixed Low□Bandgap Perovskite Solar Cells," *Advanced Functional Materials,* vol. 28, no. 51, p. 1804603, 2018.

[64] M. Liu *et al.*, "High performance low-bandgap perovskite solar cells based on a high-quality mixed Sn–Pb perovskite film prepared by vacuum-assisted thermal annealing," *J. Mater. Chem. A,* vol. 6, no. 34, pp. 16347-16354, 2018.

[65] G. Xu *et al.*, "Integrating Ultrathin Bulk□Heterojunction Organic Semiconductor Intermediary for High□Performance Low□Bandgap Perovskite Solar Cells with Low Energy Loss," *Advanced Functional Materials,* vol. 28, no. 42, p. 1804427, 2018.

[66] G. Kapil *et al.*, "Highly Efficient 17.6% Tin–Lead Mixed Perovskite Solar Cells Realized through Spike Structure," *Nano letters,* vol. 18, no. 6, pp. 3600-3607, 2018.

[67] M. Liu, Z. Chen, Y. Yang, H.-L. Yip, and Y. Cao, "Reduced open-circuit voltage loss for highly efficient low-bandgap perovskite solar cells via suppression of silver diffusion," *Journal of Materials Chemistry A,* vol. 7, no. 29, pp. 17324-17333, 2019.

[68] M. Wei *et al.*, "Combining efficiency and stability in mixed tin–lead perovskite solar cells by capping grains with an ultrathin 2D layer," *Advanced Materials,* vol. 32, no. 12, p. 1907058, 2020.

[69] Z. Yang *et al.*, "Enhancing electron diffusion length in narrow-bandgap perovskites

for efficient monolithic perovskite tandem solar cells," *Nature Communications,* vol. 10, no. 1, p. 4498, 2019/10/03 2019, doi: 10.1038/s41467-019-12513-x.

[70] K. Xiao *et al.*, "All-perovskite tandem solar cells with 24.2% certified efficiency and area over 1 cm 2 using surface-anchoring zwitterionic antioxidant," *Nat. Energy,* vol. 5, no. 11, pp. 870-880, 2020.

[71] C. Li *et al.*, "Low-bandgap mixed tin–lead iodide perovskites with reduced methylammonium for simultaneous enhancement of solar cell efficiency and stability," *Nature Energy,* vol. 5, no. 10, pp. 768-776, 2020.

[72] N. Jalili and K. Laxminarayana, "A review of atomic force microscopy imaging systems: application to molecular metrology and biological sciences," *Mechatronics,* vol. 14, no. 8, pp. 907-945, 2004.

[73] F. J. Giessibl, "Advances in atomic force microscopy," *Reviews of Modern Physics,* vol. 75, no. 3, pp. 949-983, 07/29/ 2003, doi: 10.1103/RevModPhys.75.949.

[74] I. Mora-Sero, S. Gimenez, A. Braga, I. Concina, and A. Vomiero, "Panchromatic sensitized solar cells based on metal sulfide quantum dots grown directly on nanostructured TiO2 electrodes," 2011.

[75] T. Niu *et al.*, "Stable High□Performance Perovskite Solar Cells via Grain Boundary Passivation," *Advanced Materials,* vol. 30, no. 16, p. 1706576, 2018.

[76] N. Yang, "Two-Dimensional Graphene Bridges Enhanced Photoinduced Charge Transport in Dye-Sensitized Solar Cells," in *The Preparation of Nano Composites and Their Applications in Solar Energy Conversion*: Springer, 2017, pp. 41-56.

[77] G. Juška, K. Arlauskas, M. Viliūnas, and J. Kočka, "Extraction current transients: new method of study of charge transport in microcrystalline silicon," *Physical review letters,* vol. 84, no. 21, p. 4946, 2000.

[78] J.-H. Im, I.-H. Jang, N. Pellet, M. Grätzel, and N.-G. Park, "Growth of CH 3 NH 3 PbI 3 cuboids with controlled size for high-efficiency perovskite solar cells,"

Nature nanotechnology, vol. 9, no. 11, pp. 927-932, 2014.

[79] G. Sai-Anand *et al.*, "Additive assisted morphological optimization of photoactive layer in polymer solar cells," *Sol. Energy. Mater. Sol. Cells.,* vol. 182, pp. 246-254, 2018.

[80] N. Kumar, A. H. Chowdhury, B. Bahrami, M. R. Khan, Q. Qiao, and M. Kumar, "Origin of enhanced carrier mobility and electrical conductivity in seed-layer assisted sputtered grown Al doped ZnO thin films," *Thin Solid Films,* vol. 700, p. 137916, 2020.

[81] M. Stephen, K. Genevičius, G. Juška, K. Arlauskas, and R. C. Hiorns, "Charge transport and its characterization using photo□CELIV in bulk heterojunction solar cells," *Polymer International,* vol. 66, no. 1, pp. 13-25, 2017.

[82] M. Petrović, T. Ye, C. Vijila, and S. Ramakrishna, "Influence of charge transport and defects on the performance of planar and mesostructured perovskite solar cells," *Adv. Energy Mater.,* vol. 7, no. 13, p. 1602610, 2017.

[83] Q. Dong *et al.*, "Solar cells. Electron-hole diffusion lengths > 175 μm in solution-grown CH3NH3PbI3 single crystals," (in eng), *Science,* vol. 347, no. 6225, pp. 967-70, Feb 27 2015, doi: 10.1126/science.aaa5760.

[84] K. M. Reza *et al.*, "Grain Boundary Defect Passivation in Quadruple Cation Wide□ Bandgap Perovskite Solar Cells," *Solar RRL,* p. 2000740.

[85] Q. Wang *et al.*, "Effects of Selfâ Assembled Monolayer Modification of Nickel Oxide Nanoparticles Layer on the Performance and Application of Inverted Perovskite Solar Cells," 2017.

[86] W. Chen *et al.*, "Understanding the doping effect on NiO: toward high□ performance inverted perovskite solar cells," *Adv. Energy Mater.,* vol. 8, no. 19, p. 1703519, 2018.

[87] B. Chen, H. Hu, T. Salim, and Y. M. Lam, "A facile method to evaluate the

influence of trap densities on perovskite solar cell performance," *Journal of Materials Chemistry C,* vol. 7, no. 19, pp. 5646-5651, 2019.

[88] M. Haridim, M. Zelikson, and K. Weiser, "Trapping effects in a-Si:H investigated by small-signal transient photoconductivity and the steady-state photocarrier-grating technique," *Physical Review B,* vol. 49, no. 19, pp. 13394-13399, 05/15/ 1994, doi: 10.1103/PhysRevB.49.13394.

[89] D. Spoltore *et al.*, "Effect of polymer crystallinity in P3HT: PCBM solar cells on band gap trap states and apparent recombination order," *Advanced Energy Materials,* vol. 3, no. 4, pp. 466-471, 2013.

[90] L. Zeng *et al.*, "2D-3D heterostructure enables scalable coating of efficient low-bandgap Sn–Pb mixed perovskite solar cells," *Nano Energy,* vol. 66, p. 104099, 2019.

[91] D. Luo, R. Su, W. Zhang, Q. Gong, and R. Zhu, "Minimizing non-radiative recombination losses in perovskite solar cells," *Nature Reviews Materials,* pp. 1-17, 2019.

[92] J. Yuan, Y. Jiang, T. He, G. Shi, Z. Fan, and M. Yuan, "Two-dimensional perovskite capping layer for stable and efficient tin-lead perovskite solar cells," *Science China Chemistry,* vol. 62, no. 5, pp. 629-636, 2019.

[93] S. Gu, R. Lin, Q. Han, Y. Gao, H. Tan, and J. Zhu, "Tin and Mixed Lead–Tin Halide Perovskite Solar Cells: Progress and their Application in Tandem Solar Cells," *Adv. Mater.,* p. 1907392, 2020.

[94] M. A. R. Laskar *et al.*, "Phenylhydrazinium Iodide for Surface Passivation and Defects Suppression in Perovskite Solar Cells," *Adv. Funct. Mater.,* vol. 30, no. 22, p. 2000778, 2020.

[95] K. Nakamoto, "Infrared and R aman Spectra of Inorganic and Coordination Compounds," *Handbook of Vibrational Spectroscopy,* 2006.

[96] R. Warren and W. Liang, "Raman spectroscopy of new lead iodide intercalation compounds," *Journal of Physics: Condensed Matter,* vol. 5, no. 35, p. 6407, 1993.

[97] K. Gelderman, L. Lee, and S. W. Donne, "Flat-Band Potential of a Semiconductor: Using the Mott–Schottky Equation," *Journal of Chemical Education,* vol. 84, no. 4, p. 685, 2007/04/01 2007, doi: 10.1021/ed084p685.

[98] W. Tress, N. Marinova, T. Moehl, S. M. Zakeeruddin, M. K. Nazeeruddin, and M. Grätzel, "Understanding the rate-dependent J–V hysteresis, slow time component, and aging in CH 3 NH 3 PbI 3 perovskite solar cells: the role of a compensated electric field," *Energy & Environmental Science,* vol. 8, no. 3, pp. 995-1004, 2015.

[99] P. Wang *et al.*, "Gradient Energy Alignment Engineering for Planar Perovskite Solar Cells with Efficiency Over 23%," *Advanced Materials,* p. 1905766, 2020.

[100] S. I. Rahman *et al.*, "Grain Boundary Defect Passivation of Triple Cation Mixed Halide Perovskite with Hydrazine-Based Aromatic Iodide for Efficiency Improvement," *ACS Applied Materials & Interfaces,* 2020/08/24 2020, doi: 10.1021/acsami.0c10448.

[101] K. Wang *et al.*, "All-inorganic cesium lead iodide perovskite solar cells with stabilized efficiency beyond 15%," *Nat. Commun.,* vol. 9, no. 1, p. 4544, 2018/10/31 2018, doi: 10.1038/s41467-018-06915-6.

[102] Q. Jiang *et al.*, "Surface passivation of perovskite film for efficient solar cells," *Nat. Photonics,* vol. 13, no. 7, pp. 460-466, 2019/07/01 2019, doi: 10.1038/s41566-019-0398-2.

[103] H. Elbohy *et al.*, "Tuning hole transport layer using urea for high□performance perovskite solar cells," *Advanced Functional Materials,* vol. 29, no. 47, p. 1806740, 2019.

[104] X. Hou, S. Huang, W. Ou-Yang, L. Pan, Z. Sun, and X. Chen, "Constructing efficient and stable perovskite solar cells via interconnecting perovskite grains," *ACS applied materials & interfaces,* vol. 9, no. 40, pp. 35200-35208, 2017.

[105] M. Adil Afroz *et al.*, "Thermal stability and performance enhancement of Perovskite solar cells through oxalic acid induced perovskite formation," *ACS Applied Energy Materials,* 2020/02/25 2020, doi: 10.1021/acsaem.9b02111.

[106] K. Emshadi, "Tailoring the Grain Boundaries of Wide-bandgap Perovskite Solar Cells by Molecular Engineering," 2020.

[107] C. Li *et al.*, "Reducing saturation□current density to realize high□efficiency low□bandgap mixed tin–lead halide perovskite solar cells," *Advanced Energy Materials,* vol. 9, no. 3, p. 1803135, 2019.

[108] C. Bi, Q. Wang, Y. Shao, Y. Yuan, Z. Xiao, and J. Huang, "Non-wetting surface-driven high-aspect-ratio crystalline grain growth for efficient hybrid perovskite solar cells," *Nature Communications,* vol. 6, no. 1, p. 7747, 2015/07/20 2015, doi: 10.1038/ncomms8747.

[109] Y. Wang, W. Fu, J. Yan, J. Chen, W. Yang, and H. Chen, "Low-bandgap mixed tin–lead iodide perovskite with large grains for high performance solar cells," *J. Mater. Chem. A,* vol. 6, no. 27, pp. 13090-13095, 2018.